Rotor Position and Phase Inductance Estimation of Permanent Magnet Synchronous Machine Using PWM Excitation

by

Ramakrishnan Rajavenkitasubramony

A dissertation submitted in partial fulfillment
of the requirements for the degree of
Doctor of Philosophy
(Automotive Systems Engineering)
in the University of Michigan-Dearborn
2018

Doctoral Committee:

Assistant Professor Mengqi Wang, Chair
Professor Heath Hofmann, University of Michigan
Assistant Professor Tanjore Jayaraman
Associate Professor Taehyung Kim
Tomy Sebastian, Halla Mechatronics
Assistant Professor Wencong Su

Ramakrishnan. R

rrajaven@umich.edu

ORCID iD: 0000-0001-6609-2532

DEDICATION

To my parents, Dr. R.V.S Mony and Lakshmi Mony, to my wife, Sathya K.G and my daughter Diya. R. I also dedicate this work to all my teachers who have taught me throughout my life and all my family members and friends who have supported me . Above all, I dedicate this humble work to Almighty GOD.

ACKNOWLEDGEMENTS

First and foremost, I wish to express my gratitude towards my advisors Prof. Mengqi Wang and Dr. Tomy Sebastian. Their astute mentorship, thoughtful guidance and unwavering support is deeply appreciated. In particular, their ability to distill important facts, find technical weaknesses and recommending various solutions have helped me to develop a greater knowledge and have a better understanding of it. More than anything else, I really appreciate the faith and confidence they had in me.

I am thankful to my committee members Prof. Wencong Su, Prof. Heath Hofmann, Prof. Taehyung Kim and Prof. T. Jayaraman, for asking questions and providing helpful feedback. I would like to thank Prof. Chris Mi, for the guidance and support he has provided in my thesis work. All of the guidance and helpful feedback has been key in bringing solid foundation for the work in this thesis. I would like to thank Halla mechatronics, for providing financial support as well the laboratory facility. I would like to thank all my colleagues in Halla for their mentorship and friendship during my doctoral studies. I am grateful for Dr. Mohammad Islam's expert mentorship in the area of machine design and position sensor design. I am also grateful for Dr. Abraham Gebregergis, for engaging in a variety of technical discussions related to my studies and his general support and friendship. I would like to thank Christian Ross for teaching me innovative ways of reducing cost of a drive system, and for his friendship, I learned more from him than he could imagine. I would like to thank Mazin Khlaif, Mazharul Chowdhury, Anant Singh, and Vishnu Shanker for their great friendship and for the variety of help they provided in machine testing. All my colleagues are mentors to me and this work would not be possible without them.

TABLE OF CONTENTS

LIST OF TABLES

LIST OF FIGURES

LIST OF SYMBOLS

θ_e	Electrical rotor position
θ_m	Mechanical rotor position
θ_{er}	Position error
θ'	Rotor position with error
$\hat{\theta}_{er_n}$	Magnitude of nth order position error
ω_e	Angular electrical velocity
ω_c	Frequency of the injected carrier signal
A	State transition matrix for Kalman observer
C'_{dq}	*abc* to *dq* reference frame transformation matrix with position error
C	Estimate of the error covariance in Kalman filter
e_a, e_b, e_c	Back emf voltage
e_α, e_β	Back emf voltage in α and β axis
e_0	Equivalent back emf in U0 switching state

e_1	Equivalent back emf in U1 switching state
H	State to measurement matrix in Kalman Filter
Icp	Positive sequence of the carrier-signal current
Icn	Negative sequence of the carrier-signal current
I_{acoil}	Current flowing through one winding in phase A
I_p	Peak current
i_s	Stator current
iq	q axis current
id	d axis current
i_a, i_b, i_c	Phase currents in Phase A, B, C respectvely
iq_i, id_i	Ideal d and q axis current without position error
iq', id'	Perceived d and q axis current with position error
i_{ph}	General expression for Phase current
i_{qd_c}	q and d axis current with the excitation component due to voltage injection
i_1	Current in phase A during U1 switching state
i_0	Current in phase A during U0 switching state
$idcmd$	Commanded d axis reference current

iqcmd	Commanded q axis reference current
i_{U1}, i_{U2} , i_{U3}, i_{U4} , i_{U5} , i_{U6}	Phase currents in U1, U2, U3, U4, U5, U6 switching states respectively used for current slope measurement
K_e	Back Emf constant
K	Kalman Gain matrix
L_q	q axis inductance
L_d	d axis inductance
L_0	Average self-inductance of single coil
L_2	Magnitude of second order self-inductance term of single coil
L_4	Magnitude of fourth order self-inductance term
$L_{\alpha 0}$	DC component Phase-inductance in α and β axis
$L_{\alpha 2}$	Magnitude of second order phase inductance α and β axis
L_a, L_b, L_c	Phase inductances of Phase A,B,C respectively.
L_α, L_β	Phase inductance in α and β axis
L_s	General expression for Stator Inductance
L_{s0}	DC component of the phase inductance
L_{s2}	2nd order component of the phase inductance
L_{s4}	4th order component of the phase inductance

$L_{acoil,}\ L_{bcoil},\ L_{ccoil}$	Self-inductance of a single coil in phase A,B and C
$L_{1eq}, L_{2eq}, L_{3eq}, L_{4eq}, L_{5eq}, L_{6eq}$	Equivalent inductance in U1, U2, U3 U4, U5, U6 switching states respectively
M_{ab}, M_{bc}, M_{ca}	Mutual inductance between phases
M_{S0}, M_{S1}	DC component and 2nd order component of mutual inductance between phases respectively.
M_{01}, M_{02}	DC Component of mutual inductance between two coils that are one and two slot apart respectively
M_{21}, M_{22}	2nd order component of mutual inductance between two coils that are one and two slot apart respectively
M_{41}, M_{42}	4th order component of mutual inductance between two coils that are one and two slot apart respectively
$M1$	Mutual inductance between coil 1 slot part
$M2$	Mutual inductance between coil 2 slot part
n	Order of the position error
P	No. of Poles pairs

P_α	Orthogonal current derivative component obtained from three balanced current derivative measurement
P_β	Orthogonal current derivative component obtained from three balanced current derivative measurement
p	Differential operator with respect to time
Q	Covariance matrix of the state transition noise
R	Covariance matrix of the measurement noise for Kalman Filter
r_s	Stator Resistance
r_{eq}	Equivalent resistance in all switching states
S_{U1} , S_{U2} , S_{U3}, S_{U4} , S_{U5} , S_{U6}	Current slope in switching states U1,U2,U3,U4,U5,U6 after eliminating resistive drop and back emf.
S_{off}	DC value of the current slope obtained from each switching state
S_{amp2}	Magnitude of the 2nd order component, of the current slope obtained

T_d'	Torque developed with position error
T_n	Magnitude of nth order torque ripple from nth order position error
T_{2n}	Magnitude of 2nth order torque ripple from nth order position error
T_{DC}	DC component of the motor torque
T_{Rm}	Magnitude of the mth harmonic torque ripple component
t_{min}	Minimum amount of time needed per switching state to calculate robust current slope.
V	Applied DC link voltage in the inverter
V_{acoil}	Voltage applied across one winding in phase A and neutral
v_q	Stator q-axis voltage.
v_d	Stator d-axis voltage.
v_a,v_b,v_c	Applied phase A, B,C voltages with respect to ground
$v_{an}, v_{bn}v_{cn}$	Applied phase A, B, C voltages with respect to neutral
$v_{acarrier}, v_{bcarrier}, v_{ccarrier}$	High frequency carrier signal voltage applied to phase A, B, and C respectively.

v_{ph}	General expression for applied phase voltage with respect to ground
v_s	General expression for stator voltage with respect to ground
v_α, v_β	Stator voltage in α and β axis
v_{cm}	Magnitude of the injected carrier frequency voltage
$\hat{x}$	Estimated state variables in Kalman Filter
Y	Measured signal passed in to Kalman observer.
w	Gaussian noise representation on input signal

LIST OF APPENDICES

ABSTRACT

This thesis provides rotor position estimation and online inductance estimation using the PWM signals used for motor control. The position estimation technique provides an alternative rotor position information that enables to eliminate the backup position sensor hardware needed for safety critical applications. The sensorless position estimation using PWM based excitation provides the methodology to obtain the position information without influencing the motor performance such as audible noise and torque ripple. The techniques provided can be utilized for online estimation of inductance parameters. These inductance parameters are needed in the reference current calculation in a typical motor control scheme. An Extended Kalman Observer is proposed to enhance inductance and position estimation.

Fast sampling of motor phase current is needed to calculate the current slope in the PWM excitation scheme for position and inductance estimation. This thesis provides a methodology of fast current sampling using the microcontroller without sacrificing the processor throughput time. A method to improve the accuracy of the current slope calculation is also provided.

This thesis also analyzes the effect of position sensor errors on the performance of the permanent magnet motor drive. The error has significant influence on the motor torque ripple. A mathematical analysis and experimental verification at different operating conditions is provided in this thesis.

Keywords: Position estimation, PWM excitation, Stator inductance estimation, Sensorless techniques, Extended Kalman Observer

CHAPTER 1

Introduction

1.1 Background

This research is concerned with sensorless rotor position detection and online inductance estimation of Permanent Magnet Synchronous Machine (PMSM) without the use of additional hardware. These machines are now widely used in automotive industries, especially in traction, steering and braking applications. The total system cost for PMSM motor controller drive has increased as the need for safety architecture required to support autonomous vehicles has also increased. This is because redundant sensors need to be utilized so that the system can support a "**fail-operational**" safety architecture. In addition to this, packaging the motor drive system in the vehicle is a unique challenge and cost differentiator between industry competitors. In order to reduce cost and packaging, the motor size must be reduced. To meet the various load requirements at multiple operating conditions with reduced motor size, optimal machine control becomes an essential part of the design. Accurate rotor position and motor parameter information are key elements of optimal machine control.

The main motivation in this research is to reduce cost of the fail-operational system using PMSM drive system by:

1. Developing a sensorless position estimation strategy without adding redundant hardware, thereby eliminating the need of a backup position sensor for a system designed with fail-operational safety architecture.

2. Improving the PMSM performance by online identification of the motor inductance parameters and understanding/compensating the effect of position sensor error on machine performance.

1.1.1 Safety architecture for autonomous vehicle

Autonomous or driverless vehicles are the **future of the automotive industry.** One of the prime concerns for autonomous vehicles is operational safety of the vehicle. Figure 1.1 shows the levels of automation as defined by Society of Automotive Engineers (SAE) and National Highway Safety Administration (NHTSA).

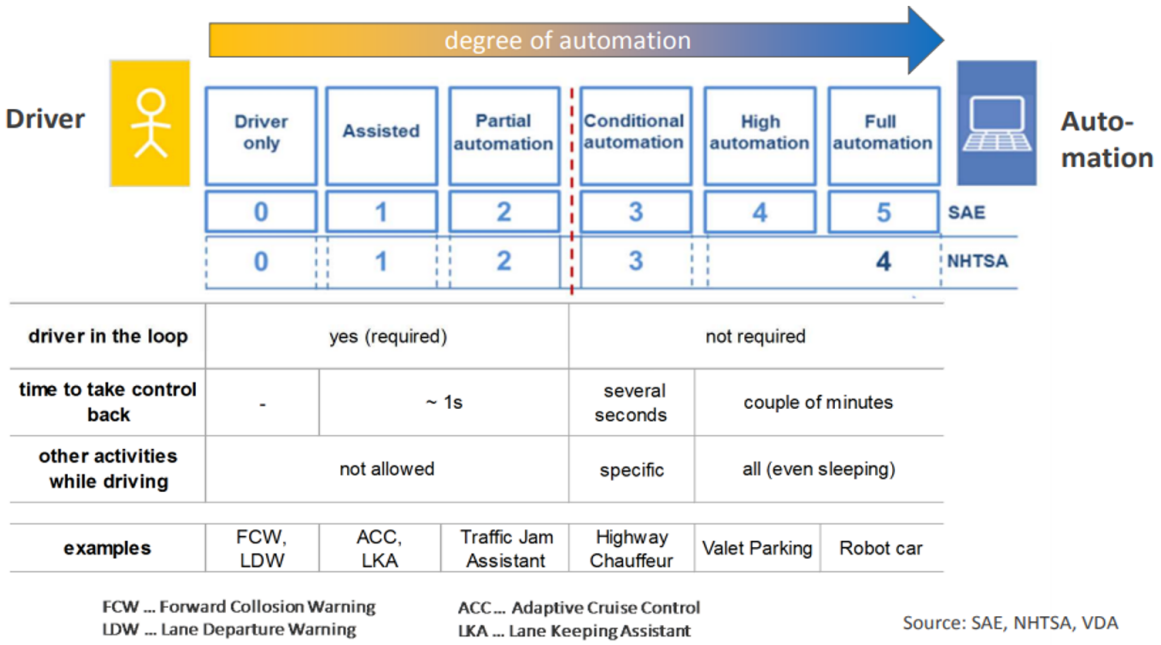

Figure 1.1: Level of automation as defined by SAE and NHTSA

It can be seen from Figure 1.1 that for level 3 automation and greater, where a driver is not required to be in the loop, it is essential that any one failure in the safety critical systems of the vehicle (such as traction, steering, braking etc.) does not lead to unsafe operation of the vehicle. This requirement has caused the system architecture design for these safety critical subsystem to move from fail–safe architecture to what is known as fail-operational architecture [1].

Figure 1.2 shows a typical fail-safe architecture with respect to the position sensor hardware. The main principle here is that the two redundant sensors are monitored by the drive system and in the event of a failure of either sensor, the output of the system is switched off. This is because we cannot identify which sensor has failed.

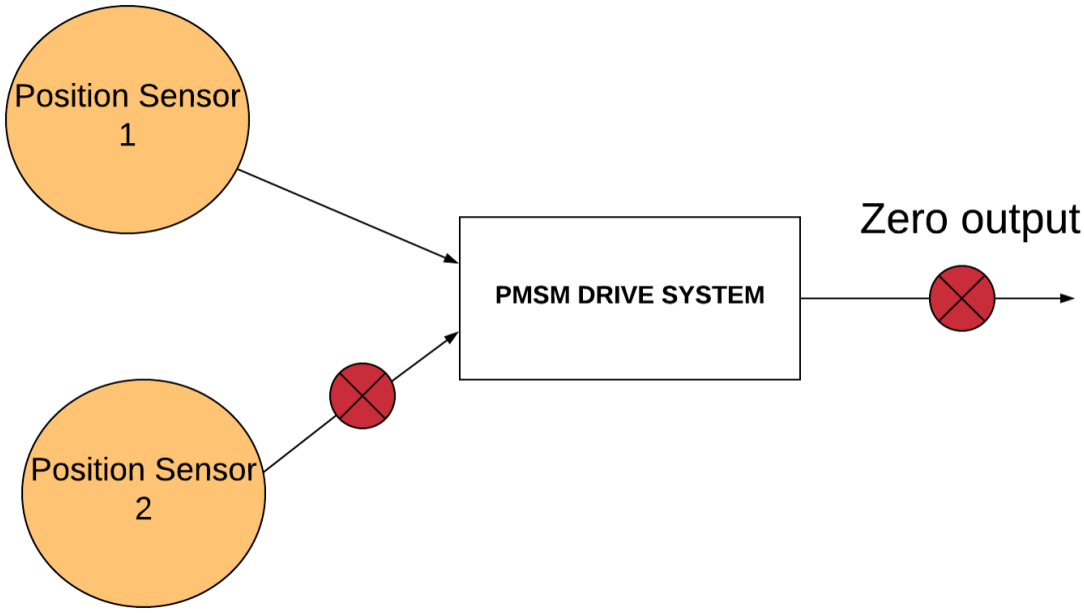

Figure 1.2: Fail safe architecture where one sensor fail will result to no output

As mentioned before, switching off the system in case of failure may not be always safe in the case of an autonomous vehicle. "**Fail-operational**" safety architecture can be realized with diverse redundant hardware. Diversity is achieved with two or more elements of hardware and software application. Figure 1.3 shows a typical 2-out of 3 safety architecture (2oo3) [2]. This safety

architecture consist of three different sensors being monitored by the processing unit. In the event of one sensor failure we can maintain full operation as we can now identify the failed senor and continue with the other two valid sensors.

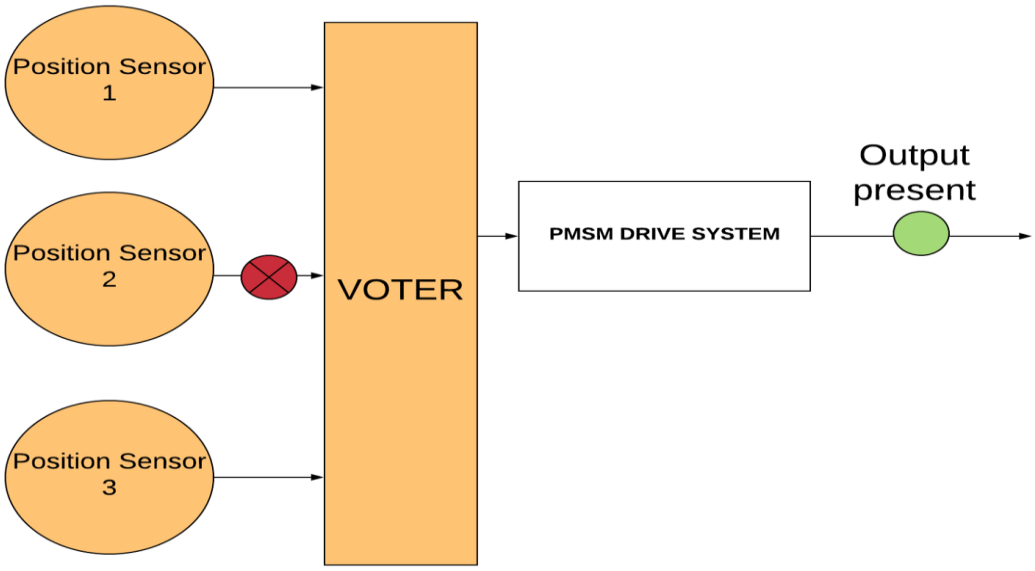

Figure 1.3: Fail-operational safety architecture with 3 sensor where one sensor fail will not result in zero output

The 2oo3 architecture leads to more cost because of additional wiring and increased complexity. One of the solution to address this problem is to use a “smart sensing” strategy where the third position information is estimated from other smart control techniques without using a third sensor, shown in Figure 1.4. This strategy uses sensorless techniques to estimate rotor position which the system will incorporate to determine which physical position sensor has failed in order to safely continue providing system output.

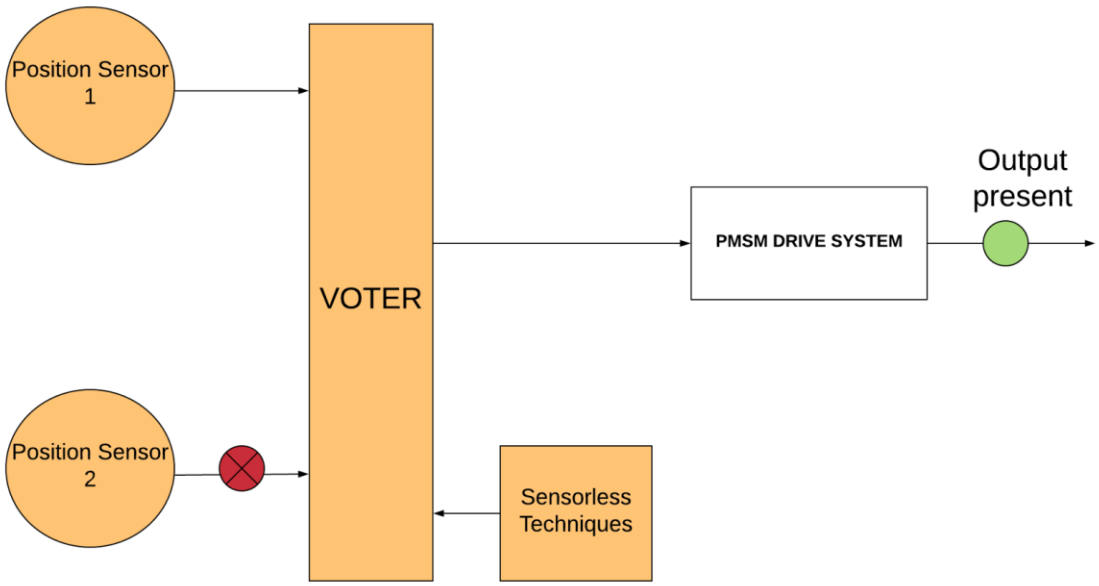

Figure 1.4: Smart sensing strategy to use sensorless technique for position diagnostic

This research topic is thus motivated to reduce the cost of position sensor deployed in the redundant architecture of a PMSM drive system. This is achieved by sensorless position estimation using PWM excitation. The various control schemes needed for detecting motor position for low and high speed are developed herein. The sensorless position techniques proposed in this research can be used in applications where there is a need for a redundant position sensor.

1.2 Literature review

Sensorless position estimation for permanent magnet synchronous machines has been a vast area of research for the past few decades. This research can be generally divided into two main categories:

1. Fundamental Excitation Techniques
2. Saliency/High-Frequency Injection techniques

1.2.1 Fundamental excitation techniques

The fundamental excitation method can further be classified into two broad categories:

a. Back EMF based estimation.
b. Model observer-based estimation.

1.2.1.1 Back EMF based estimation

The main idea behind this technique is to track speed dependent phenomenon such as back-emf to obtain the position information. Since the back emf is a speed dependent signal, it will ultimately fail as a method to provide position information because the magnitude of this signal will become zero when speed is zero. The voltage equation of a non-salient pole ($L_d = L_q = L_s$) in dq coordinates is given by:

$$\begin{bmatrix} v_q \\ v_d \end{bmatrix} = \begin{bmatrix} r_s + pL_s & \omega_e L_s \\ -\omega_e L_s & r_s + pL_s \end{bmatrix} \begin{bmatrix} iq \\ id \end{bmatrix} + \begin{bmatrix} \frac{\omega_e K_e}{P} \\ 0 \end{bmatrix} \quad (1.0)$$

Where:

p = differential operator.

r_s = stator resistance.

L_s = stator inductance.

K_e = motor constant.

ω_e = angular electrical velocity.

v_q = stator q-axis voltage.

v_d = stator d-axis voltage.

iq = stator q-axis current.

id = stator d-axis current.

P = Number of pole pairs.

Transforming (1.0) into $\alpha\beta$ coordinate we can see that the rotor position information is included in the Back EMF term as given in (1.1) where θ_e is the electrical rotor position. By estimating Back EMF, it is possible to obtain the position information.

$$\begin{bmatrix} v_\alpha \\ v_\beta \end{bmatrix} = \begin{bmatrix} r_s + pL_s & 0 \\ 0 & r_s + pL_s \end{bmatrix} \begin{bmatrix} i_\alpha \\ i_\beta \end{bmatrix} + \omega_e K_e \begin{bmatrix} -\sin\theta_e \\ \cos\theta_e \end{bmatrix} \quad (1.1)$$

This Back EMF based estimation scheme uses voltage and current for estimating both flux and motor velocity. This estimation technique is very sensitive to the variations in machine parameters. The estimation of the stator flux is defined as the time integral of induced voltage. The use of simple integration is not proposed in the literature because simple integration has an infinite gain at zero speed. There is also an unavoidable offset issue with this technique. A low pass filter is

used instead since it has a finite dc gain at zero speed, however unacceptable amplitude error as well as a phase error at low amplitudes is introduced.

Various improvement techniques have been proposed to reduce the minimum speed that position can be estimated in [3]–[6] This is achieved by compensating for amplitude errors and phase error at low amplitudes.

In the case of the Interior Permanent Magnet Synchronous Machine (IPMSM), the position information is embedded in both back emf term as well as in the saliency term. Reference studies [7]–[9] apply BEMF estimation for the IPMSM machine. These references incorporate the saliency-based factor into the Back EMF observer. The Back EMF term combining the saliency term is shown in (1.2). The back-emf term combining the saliency portion is termed as "*Extended Electromotive Force*." The observer used for estimation of extended EMF is more complicated than the simple observer used for tracking BEMF without the saliency term. The advantage, in this case, is that the EMF term also contains a term due to saliency that is dependent on the change in current. This factor can be used in the observer to track the position in addition to the regular BEMF term.

$$\begin{bmatrix} e_\alpha \\ e_\beta \end{bmatrix} = \{\left(L_d - L_q\right)\left(\omega_e id - \frac{diq}{dt}\right) + \omega_e K_e\}\begin{bmatrix} -\sin\theta_e \\ \cos\theta_e \end{bmatrix} \tag{1.2}$$

From (1.2) it can be seen that PMSM case is a particular instance when $L_d = L_q$. The main issue remaining to be addressed is the position estimation at zero speed as the magnitude of the EMF term becomes zero.

Apart from the problem of the low magnitude of the sensed voltage, the accuracy of the estimated position is affected due to motor parameter variations. A majority of the literature uses various

online parameter estimation methods to improve the accuracy. The sliding mode based observer technique used in [10]–[12] reduces the parameter sensitivity issue discussed above. The main challenges of sliding mode are:

1. Chattering noise especially at low speeds due to the small magnitude of the BEMF signal.
2. For good tracking at high-speed, the sliding mode observer's gain needs to be high, which in turn causes significant torque disturbances.

1.2.1.2 Model observer-based estimation

The main idea is to observe the error between either the measured current or torque with the model predicted values and then use that information to self-correct and estimate position. These techniques suffer from multiple challenges, primarily the estimation at low speed and zero speed and effectiveness with parameter variations in the model. Techniques to reduce the impact of parameter variations are described in [13], [14]. The other main drawback of this method is that model predicted values need to incorporate various nonlinearities in the system, otherwise the observer will introduce error in the position estimated.

Thus, it can be concluded that the fundamental excitation technique has following characteristics:

1. Can be implemented for mid and high speeds
2. Sensitive to parameter variation
3. Fails to work at zero and low speed.
4. The bandwidth improvement of this technique is limited.

1.2.2 Saliency/High-Frequency injection techniques

To overcome the limitation of estimating position at zero and low-speed, sensorless control methods based on tracking the saliency in the electric machine have been proposed. These techniques measure the machine response to a high-frequency excitation. The high-frequency excitation applied through the inverter is distinct from the fundamental excitation used for torque production. These methods have the capability to provide accurate measurement for zero and low speed.

The significant differences between the High-frequency excitation methods are:

1. The type of excitation given to the system
2. The measured signals and various signal processing needed to estimate position.

The Figure 1.5 shows the general classification of High-frequency injection techniques.

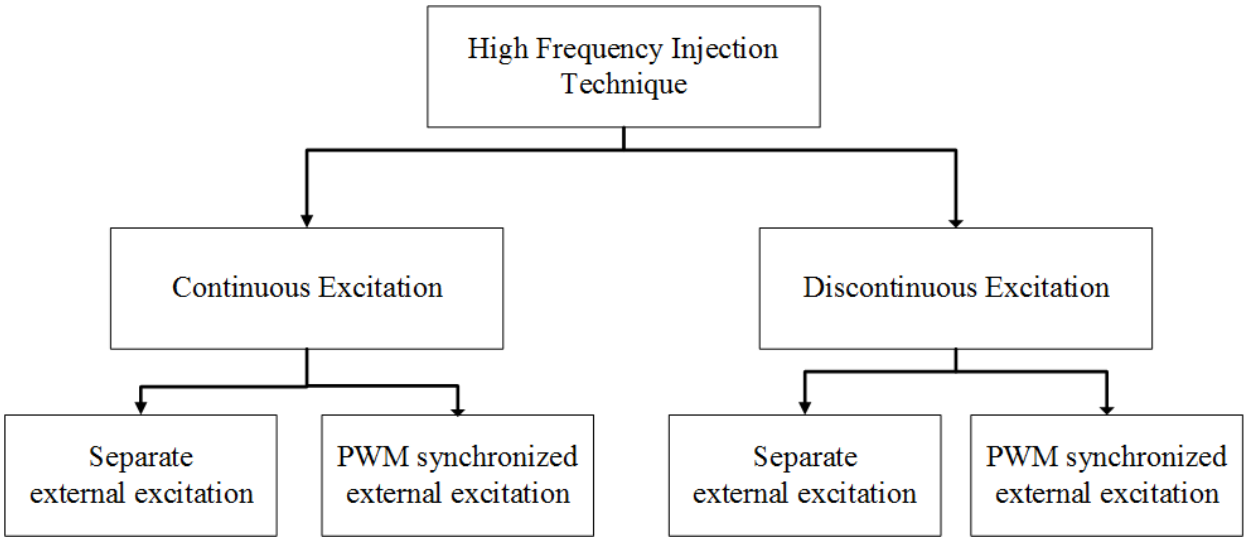

Figure 1.5: High-Frequency Injection Technique

From *Figure 1.5* it can be seen that High-Frequency Excitation can be broadly classified into the following types:

1. Continuous excitation
2. Discontinuous excitation

n general, if the high-frequency excitation used to estimate the rotor position is always present along with the fundamental excitation, it is referred to as continuous excitation. In the case of discontinuous excitation, the excitation is done periodically.. In general, the high-frequency excitation is provided either in the applied voltage or in current with the former being preferred. The reason for this preference is that current injection has numerous difficulties such as [15]:

1. Relatively large amplitude signal need to be injected.

2. The higher amplitude signal produces torque ripple.
3. Minimal spectral separation makes isolating carrier frequency from the fundamental frequency difficult.

1.2.2.1 High-Frequency machine model

In general, the physical principal on all these methods is to first measure the current response when a high frequency excitation, distinct from the fundamental excitation is applied, followed by appropriate demodulation and processing with a closed loop observer as discussed in [16] . A high bandwidth current loop is required for this injection.

The following assumptions are made to create the high-frequency model of the machine:

1. For high frequency excitation, the resistive terms are not significant and can be eliminated from the equation.
2. High-frequency excitation is separated from the fundamental excitation.
3. The machine considers only second order saliency, higher orders are negligible and therefore ignored.

Figure 1.6 shows the change in inductance as a function of rotor position in a PM machine. Using the assumptions listed above, we can derive the high-frequency model of the machine at zero and low speed in matrix form as given in (1.3). The mutual inductance are omitted here:

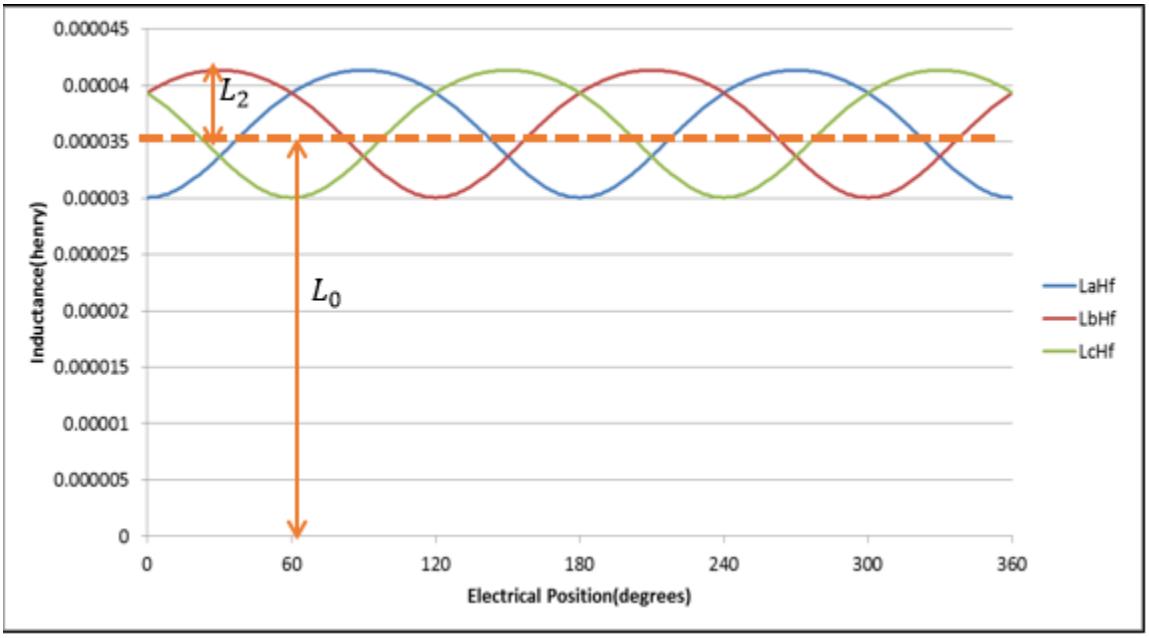

Figure 1.6: Inductance variation with position

$$\begin{bmatrix} v_a \\ v_b \\ v_c \end{bmatrix} = \begin{bmatrix} L_a & 0 & 0 \\ 0 & L_b & 0 \\ 0 & 0 & L_c \end{bmatrix} \begin{bmatrix} \frac{dia}{dt} \\ \frac{dib}{dt} \\ \frac{dic}{dt} \end{bmatrix} \tag{1.3}$$

where:

$L_a = L_{S0} + L_{S2} \cos 2(\theta_e)$

$L_b = L_{S0} + L_{S2} \cos 2(\theta_e - 120)$

$L_c = L_{S0} + L_{S2} \cos 2(\theta_e - 240)$

v_a, v_b, v_c: voltages applied by the inverter to the machine.

By transforming the (1.3) into the equivalent *dq* frame model, (1.4) is obtained

$$\begin{bmatrix} v_q \\ v_d \end{bmatrix} = \begin{bmatrix} L_{S0} + L_{S2}cos(2\theta_e) & L_{S2}sin(2\theta_e) \\ L_{S2}sin(2\theta_e) & L_{S0} - L_{S2}cos(2\theta_e) \end{bmatrix} \begin{bmatrix} \frac{diq}{dt} \\ \frac{did}{dt} \end{bmatrix} \quad (1.4)$$

The equation (1.4) is the general high-frequency model.

1.2.2.2 Continuous injection

From Figure 1.5 it can be seen that the major difference in between continuous and discontinuous techniques come from whether the high-frequency excitation carrier signal has any relationship with the PWM switching states. If the carrier signal has no connection with the PWM switching states, those techniques are referred to as separate excitation method. In the case where the excitation is given periodically in between the PWM switching states, the method is referred to as PWM synchronized excitation. In the case of periodic excitation, the carrier signal used for excitation is described in (1.5) with magnitude v_c and frequency ω_c . The high frequency excitation signal interacts with the machine saliency to produce current that contains information relating to position.

$$v_{acarrier} = v_{cm}\cos(\omega_c t) \quad (1.5)$$

$$v_{bcarrier} = v_{cm}\cos(\omega_c t - 120)$$

$$v_{ccarrier} = v_{cm}\cos(\omega_c t - 240)$$

The resultant current measured has a positive and negative sequence component [17], [18]. This is shown in (1.6), where the I_{cp} is the magnitude of the positive component and I_{cn} is the magnitude of the negative component.

$$i_{qd\_c} = -jI_{cp}e^{j\omega_c t} - jI_{cn}e^{j(2\theta_e - \omega_c t)} \tag{1.6}$$

From (1.6) it can be seen that the position θ_e information is found in the negative sequence component. There are different techniques to estimate position using different type of observers as seen in [19], [20]. Implementation of these techniques requires at least two current sensors. In (1.6) the only the current resulting from carrier signal voltage excitation is shown. In normal operation however, the measured stator current will also include the fundamental current used for current control. Preventing interference between the negative-sequence carrier signal current and the fundamental current is of great importance and is usually achieved by the signal-processing scheme shown in Figure 1.7.

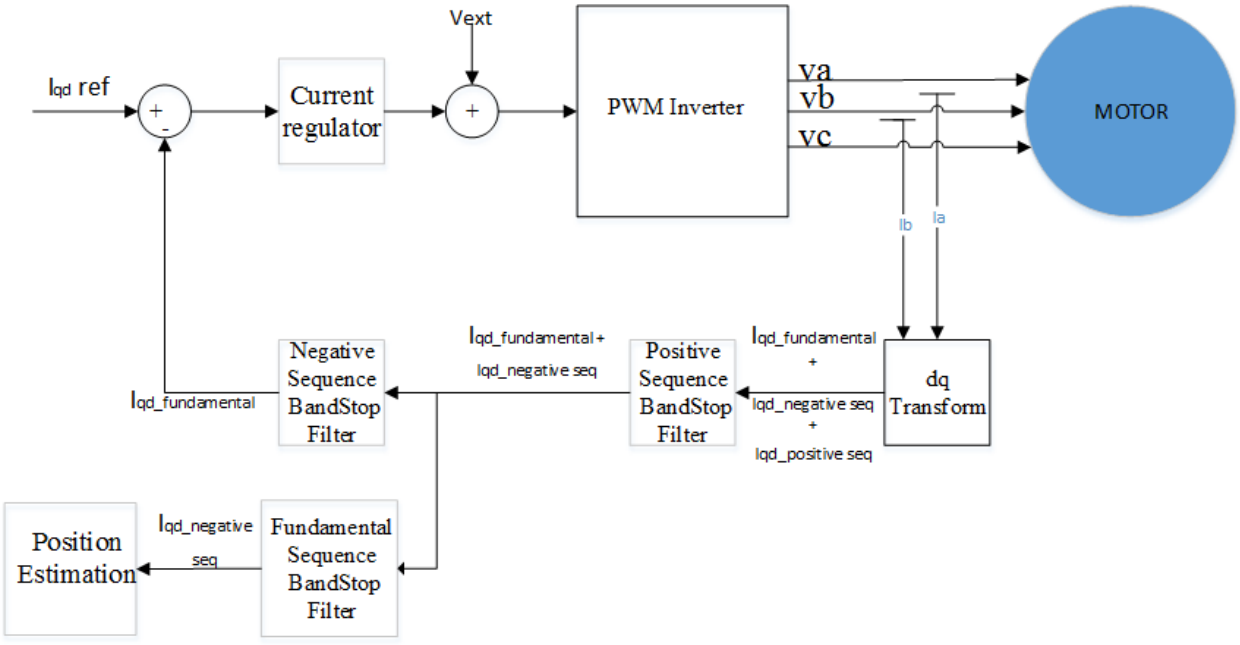

Figure 1.7: Block diagram showing the signal processing of the High frequency excitation method

While these techniques can detect position at zero and low speeds, there are a few drawbacks. One major drawback is that the inverter nonlinearities, such as the dead time, causes distortion in the measured current signal and this affects the accuracy of the estimated position. Another major concern with continuous excitation is in the impact on audible noise performance. In an application such as steering, noise vibration and harshness (NVH) requirements are critical system charachteristics where acoustic noise is of primary concern. The effect of BEMF at high speed is another area of concern in these applications but is not addressed in much of the literature because the focus is about low and zero speed operation. References [15] and [21] discuss similar methods of high-frequency excitation but injecting it in current rather than voltage.

1.2.2.3 Discontinuous injection

In this technique instead of giving a continuous injection, a periodic burst injection is utilized [22], but the principle of position detection remains the same as explained in 1.2.2.2. While this technique reduces some of the drawbacks found in continuous injection, such as acoustic noise issue, it introduces other drawbacks, specifically position accuracy decreases as rotor speed increases since continuous position estimation is not available. Therefore this technique is mainly used for zero and low speed applications.

Another technique in the discontinuous injection method, which has been successful for estimating position, is integrating the excitation with the PWM signal. The method is referred as the "*Indirect Flux detection by On-line Reactance Measurement (INFORM)*" [23]. The basic idea of this method is to measure the current response to the voltage injection that is integrated with the pulse width

modulation (PWM) pattern. The current response is measured using the current sensor that is typically utilized for the motor drive control. This strategy has the following characteristics:

1. No extra hardware required
2. Applicable to low-cost DSPs
3. Applicable mainly to zero and low speed
4. Higher current ripple, resulting in degraded acoustic noise performance

From (1.3) it can be observed that the derivatives of phase current are a function of the instantaneous voltage and equivalent high-frequency inductance. Therefore, measuring the derivative of phase current due to the excitation and knowing the voltage applied, the position information can be determined.. The INFORM inductance can be defined as given in (1.7). The inductance contains the desired information of rotor position.

$$L_s = \frac{v_s}{\frac{dis}{dt}} \tag{1.7}$$

Where:

L_s = stator inductance

v_s = stator voltage

i_s = stator current

These techniques need a minimum time for the current measurement to be made. The INFORM technique uses the various appropriate switching states of the inverter to apply the excitation so that the effect of the current distortion can be minimized. A benefit of INFORM is that the average voltage of the excitation is zero, therefore the torque disturbance is minimum.

Drawbacks of this method are [24]:

1. It is suited for zero and low speed.
2. High current ripple due to which additional losses and acoustic noise.

1.3 Thesis objectives and outline

The last section showed a comprehensive summary of the various advancements made in the area of sensorless control of PM machines. The following points can be concluded from the review

1. Fundamental excitation techniques work well for medium to high speed and have low threshold point usually around 300-400rpm.

2. Fundamental excitation techniques are parameter sensitive, though various control strategies such as sliding mode observer are used to minimize these effects.

3. High-frequency injection techniques work well for the zero and low speed operation.

4. Continuous injection techniques are susceptible to various non-ideal behaviors in the inverter such as inverter dead time, which produces distortion in the measured signal.

5. PWM integration based excitations are not significantly affected due to inverter nonlinearities such as the dead time [29-30]. Since measurement of the high-frequency response is done in the time domain, the non-linear effect of dead time can be avoided by sampling the current after switching transitions have settled.

6. Continuous Injection and PWM integration technique suffer from poor acoustic and torque ripple issues.

7. Extra di/dt sensors are usually required for PWM injection-based methods [25], [26]which are not incorporated in industry as it leads to additional cost.

Thus, one of the conclusions that can be drawn from this study in regards to low torque ripple application fields, such as steering, is that both fundamental and high-frequency injection methods are not optimal. The most significant obstacle of the fundamental excitation method is that it is not capable of estimating position for zero and low speed. This method can be used for conditions where speed is above 500rpm. In cases of high-frequency injection techniques, torque ripple is produced and significant acoustic noise is introduced which is undesirable in many applications.

Major factors which affect the performance of a PMSM drive are the accurate knowledge of both rotor position and motor parameters. The literature [27], [28] does not provide the effect of position error at all operating ranges. This research begins with creating a mathematical model to show the effect of position sensor error on the torque produced by the machine at all operating conditions. Also shown in this research is the effect of position sensor compensation. Another aspect of this research is to develop an online technique to estimate the inductance of the machine using the

PWM based excitation. Accurate knowledge of the inductance at all operating condition improves the torque speed performance of the machine. An in-depth treatment of this topic is given in this research.

Thus the main objectives of this thesis are:

1. To understand/ improve the effect of position sensor error on the performance of PMSM machine.
2. To investigate the online stator inductance estimation at all speed including zero speed using the PWM excitation.

3. To investigate the possibility of position estimation at low and mid speed in a PM machine using the PWM excitation that is used to control the motor, therefore avoiding any external high-frequency injection.

4. To investigate the possibility of a low-cost motor position estimation solution without using any additional sensors, other than the current sensor, that is commonly utilized for the control of PM machines.

5. To determine a strategy for minimizing the current ripple developed in PWM excitation based position sensorless technique.

6. To develop architecture for high speed current sensing without affecting any software throughput, thereby making it easier to be deployed in practical production environment.

1.4 Dissertation organization

The remainder of this dissertation is organized as follows. Chapter 2 will address the effect of position sensor error on the performance of the PMSM machine. This chapter goes to develop a mathematical model for the benefit of understanding the effect of position sensor on a current control PMSM drive, showing the effect of the position error on the current and on the resulting torque developed. Chapter 3 analyzes the variation of inductance with position for the motor under study which is the basis for both inductance and position estimation. The mathematical expression developed for the inductance variation are verified experimentally and using Finite Element (FE) analysis. Various conclusion are made which form the basis for later chapters. Chapter 4 introduces the PWM excitation methodology and develops a model to estimate inductance using the PWM excitation. In this chapter, key implementations are discussed such as, maintaining current excitation at zero speed and zero voltage. Experimental results are shown and compared with the FE and model results. In chapter 5 fast current sampling strategy is discussed. The fast current sampling forms the key aspect which allows the implementation of PWM excitation based position estimation in the processor without additional hardware. In order for such method to be practically viable the software throughput should not be affected. This chapter develops a new architecture of oversampling current without affecting software throughput. Various current slope measurement strategies are discussed and practical results are shown. After having discussed the PWM excitation method and the current sampling architecture, the Chapter 6 deals with position estimation using the PWM excitation. This chapter introduces a strategy to estimate position with minimum current ripple, showing the key improvements from other literatures dealing with position estimation using PWM signals. This chapter goes to detail the Extended Kalman Observer

(EKO) implementation used for position and inductance estimation. The position estimation strategy at zero speed and high speed are also discussed in this chapter. Various results are shown for zero, low and mid speed position estimation. Finally Chapter 7 provides conclusions and future work.

CHAPTER 2

Effect of Position Sensor Error on the Performance of Permanent Magnet Machine Drives

2.1 Introduction

In Permanent Magnet Synchronous motor (PMSM) drives, shaft position information is required for the proper control of the machine. In the PMSM drive the torque ripple generated by the machine has various harmonic content. The major torque ripple generated in a three phase machine is due to the interaction of 5th, 7^{th}, 11^{th} and 13^{th} harmonics in the back emf with the phase current. These induced voltage harmonics are responsible for the 6^{th} and 12^{th} order (electrical) ripple in the torque. In practical applications we tend to see various other harmonic orders in the torque. Figure 2.1 shows the various torque harmonics measured from an 8-Pole current controlled Interior Permanent Magnet Synchronous Machine (IPMSM). It can be seen that in addition to the 6^{th} and 12^{th} order electrical (24th and 48^{th} order mechanical) we see several other harmonic orders.

This chapter analyzes the effect of the position error on the applied phase current and thereby on the resultant torque produced in a current controlled IPMSM drive. The various types of position error involved in a Hall Effect based sensor in a practical application are discussed in [29]. This research showed various causes for different types of error in a hall effect based sensor and also the effect of those position errors on generated torque for a PMSM drive. This research did not discuss the reasons for the various harmonics generated in the torque ripple due to position error. The research is primarily focused on the modeling of IPMSM drive including the electromagnetically originating torque ripple. This research did not consider the torque ripple originating from the position sensor error. The study presented in [27], [28], [30] discusses various torque ripple causes on PMSM drive such as cogging torque and provides various techniques to

minimize these effects by optimizing the motor design. However, these studies do not consider the effect of position error on the torque ripple generated. While the study presented in [31], [32] shows the effects of the position resolution and accuracy on the torque developed, it does not provide a good mathematical understanding of these effects due to position error. The study provides much in terms of practical results, which show the effect of position offset error with speed. However, this literature does not provide a good mathematical understanding of how the position harmonics affect the applied phase current and generated torque. The study presented in [33], [34] show various techniques for estimating rotor position and the associated error, but does not consider the effect on torque production. The study presented in [35]–[39] show various ways to compensate for the position error which in turn reduces the effect of position sensor error on the torque ripple generated. These studies do not consider the effect of position error on the generated torque, rather mainly concentrates on how to reduce the position error. In [40] a relationship between angle error and torque ripple is shown, but it does not provide any practical data and fails to describe the effect of this relationship within a current controlled closed loop system of a PMSM drive. Various online corrections for reducing the position sensor error are presented in [41]–[44] These papers also do not provide a general analysis of how position error influences the phase current generated and the resultant torque.

This chapter is organized as follows: Section 2.2 presents the type of sensor used for the analysis and the general blocks involved in the closed loop current control of IPMSM drive. Section 2.3 is divided in to two sub sections. The first subsection presents the effect of motor position error on the current harmonics in the machine with a mathematical model. While the second presents the mathematical model showing the effect of the position sensor on the torque generated. Section 2.4 presents both the model as well as experimental results to illustrate the effect of position sensor error on the applied current and on the torque produced. Section 2.5 will consider the effect of a

practical position sensor's error on torque production. An approach of compensating the position error and its effect on the torque ripple are also demonstrated.

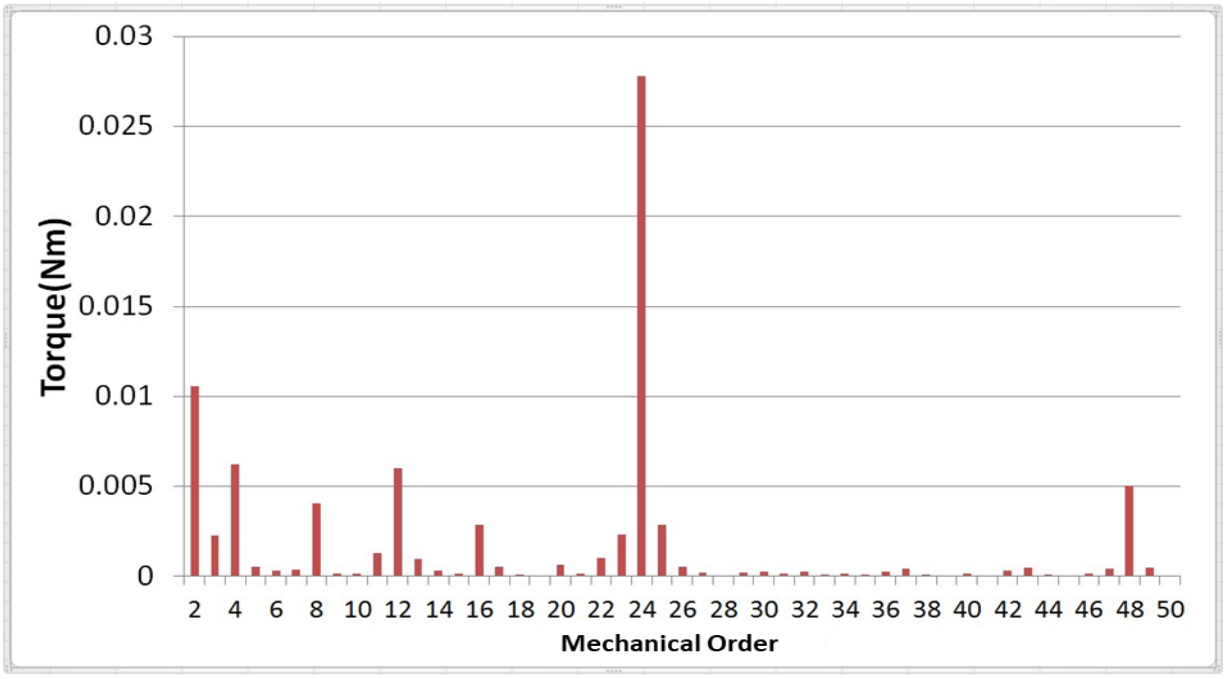

Figure 2.1: Torque harmonics in the measured torque from an 8pole IPMSM

2.2 Position sensor block diagram and types of error

The hall-effect, magnetoresistive or resolver type sensors are very often used for shaft position sensing in PMSM drives. The position obtained from the sensor is used in the computation of the voltage vector to be applied to the motor and in the Park transformation of phase currents to *dq* axis currents. *Figure 2.2*. shows the ideal placement of the Hall Effect sensor with respect to the rotating magnet. In practical implementation, misalignment between the magnet and the sensor will always be present. In addition, there is part-to-part variation between the sensor devices (Hall IC), resulting in various type of errors as discussed in [29]. Other types of position sensors also will have errors due to misalignment and other manufacturing tolerances.

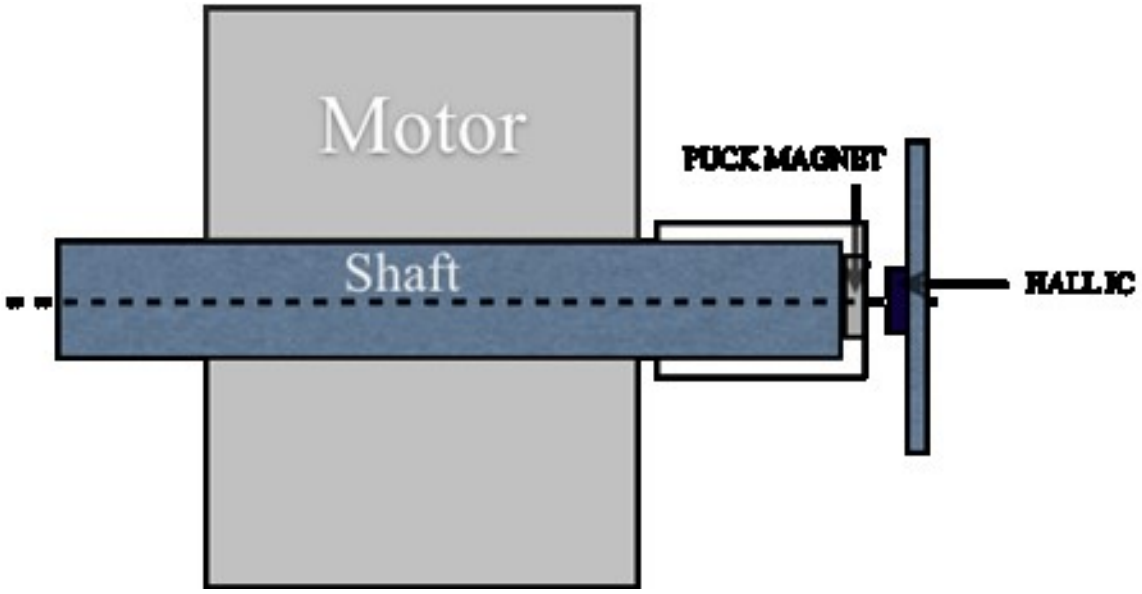

Figure 2.2: Ideal hall sensor setup for rotor position sensing in synchronous machine

Figure 2.3 shows the general block diagram of a current controlled IPMSM drive in which a PI control mechanism is used for controlling the current. The output of the PI is then fed into a Space Vector PWM (SVPWM) block that converts the *dq* voltages to phase voltages that are applied to the motor. The main two blocks which uses the position in the current controlled IPMSM drive are a) current transformation from abc to *dq* block and b) applied voltage calculation block. The erroneous position is used in the application of phase voltage which creates a resultant phase

current. The phase current obtained contains ripple which produces ripple in the resultant torque. The phase current generated is fed back to the controller where the erroneous position is used to convert it to the *dq* coordinate system. The effect of this operation is such that the perceived *dq* current by the controller is oblivious of the actual current ripple in the machine. Therefore current control cannot correct for the actual phase current ripple. The closed loop effect of position error can be analyzed in two parts: 1) The effect of position error on the actual current developed in the machine and 2) The effect of this current on the torque generated by the machine. In the next section these two parts are analyzed in detail.

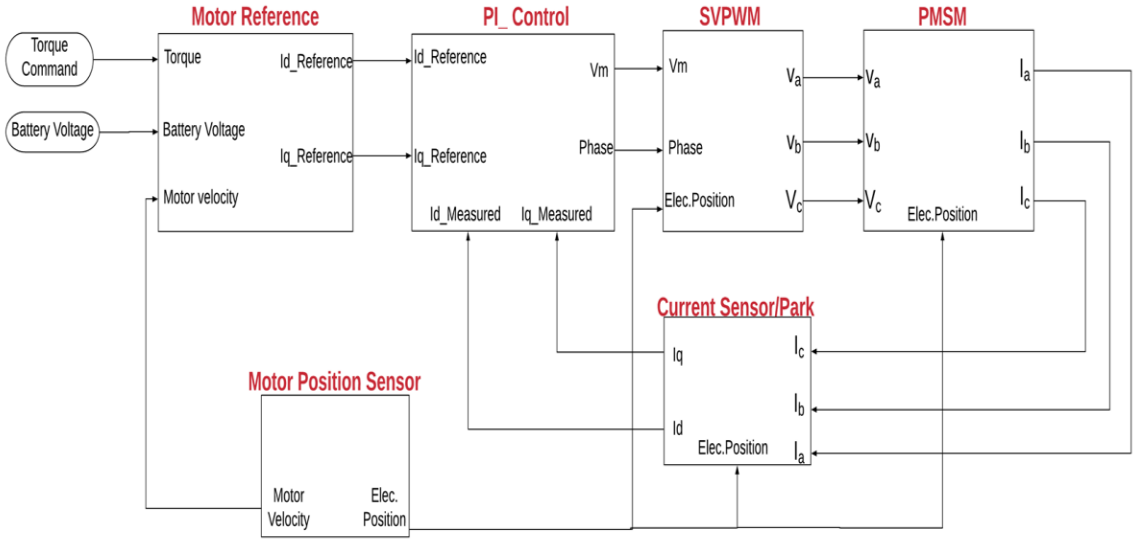

Figure 2.3: Block diagram of current controlled IPMSM

2.3 Torque ripple analysis due to position error

In this section the analysis is divided in to 1) The effect of position error on the phase current and 2) the effect of the resultant current on the developed torque. *Figure 2.4*. shows the reference axis defined which shall be used for the analysis. The picture shows both the stationary abc axes, stationary α β axes and the rotating *dq* axes. It is to be noted that the α axis is aligned with phase a axis. The transformation from three phase frame to the *dq* frame can be given as shown in (2.1).

$$\begin{bmatrix} iq_i \\ id_i \end{bmatrix} = \frac{2}{3}\left[C_{dq}\right]\begin{bmatrix} i_a \\ i_b \\ i_c \end{bmatrix} \tag{2.1}$$

Where:

$$C_{dq} = \begin{bmatrix} \cos(P\theta_m) & \cos(P\theta_m - 120) & \cos(P\theta_m + 120) \\ -\sin(P\theta_m) & -\sin(P\theta_m - 120) & -\sin(P\theta_m + 120) \end{bmatrix}$$

iq_i = Ideal q axis current with no error in position

id_i = Ideal d axis current with no error in position

P = No. of Pole pairs.

It is to be noted that the (2.1) is written in terms of mechanical rotor position θ_m. The positive *d*-axis is chosen as the demagnetizing current as opposed to the magnetizing current. This way in the control range *id* is always positive.

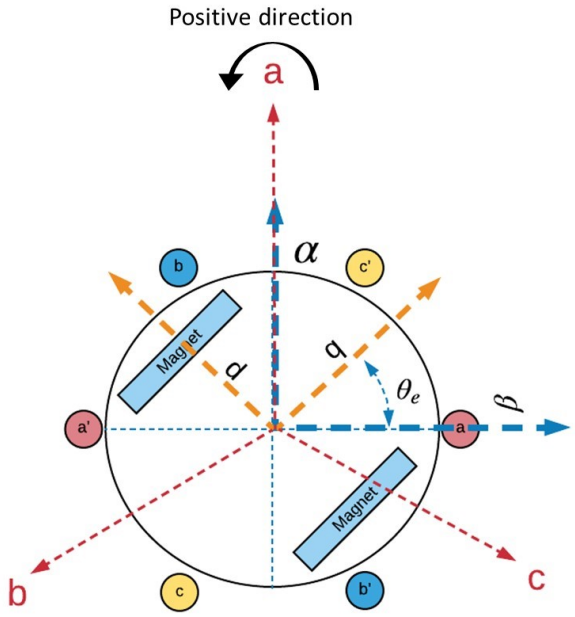

Figure 2.4: Motor reference axis definition

2.3.1 Effect of position error on current

Let us define θ_m as actual rotor mechanical position. The erroneous mechanical position read by the sensor can be defined as θ'

$$\theta' = \theta_m + \theta_{er} \tag{2.2}$$

where:

$$\theta_{er} = \sum_{n=0}^{n=\infty} \hat{\theta}_{er_n} * \cos(n\theta_m) \tag{2.3}$$

The n in the (2.3) is defined as the major harmonic orders present in the measured position and $\hat{\theta}_{er_n}$ is defined as the magnitude of the position error for the nth harmonic. The applied phase voltage uses this erroneous position. The resultant dq current in the machine can be written as shown in and (2.4) and (2.5).

$$iq' = \frac{2}{3}[i_a \cos(P\theta') + i_b \cos(P\theta' - 120) + i_c \cos(P\theta' + 120)] \quad (2.4)$$

$$id' = -\frac{2}{3}[i_a \sin(P\theta') + i_b \sin(P\theta' - 120) + i_c \sin(P\theta' + 120)] \quad (2.5)$$

Using the (2.2) we can expand (2.4) and (2.5) as given in (2.6)

$$\begin{bmatrix} iq' \\ id' \end{bmatrix} = \frac{2}{3}\left[C'_{dq}\right] \begin{bmatrix} i_a \\ i_b \\ i_c \end{bmatrix} \quad (2.6)$$

where:

$$C'_{dq} = \begin{bmatrix} \cos(P\theta') & \cos(P\theta' - 120) & \cos(P\theta' + 120) \\ -\sin(P\theta') & -\sin(P\theta' - 120) & -\sin(P\theta' + 120) \end{bmatrix}$$

Simplifying the equation and using the expression for iq_i and id_i , the resultant iq' and id' current can be expressed as given in (2.7).

$$iq' = \cos(P\theta_{er})\, iq_i - \sin(P\theta_{er})\, id_i \quad (2.7)$$

$$id' = \cos(P\theta_{er})\, id_i + \sin(P\theta_{er})\, iq_i$$

Expanding the sine and cosine terms using Taylor series expansion, neglecting higher orders and substituting for θ_{er} from (2.3), the dq current in the machine can be expressed in terms of actual position θ_m as

$$iq' = \left[1 - \frac{\left(P\hat{\theta}_{er}\right)^2 (1 + \cos(2n\theta_m))}{4}\right] iq_i - P\hat{\theta}_{er}\cos(n\theta_m) id_i \quad (2.8)$$

$$id' = \left[1 - \frac{\left(P\hat{\theta}_{er}\right)^2 (1 + \cos(2n\theta_m))}{4}\right] id_i + P\hat{\theta}_{er}\cos(n\theta_m) iq_i$$

Eq. (2.8) shows that the resultant current generated in the machine has both n^{th} and $2n^{th}$ harmonic components. This is because we only considered lower order terms in the Taylor series expansion. It is important to understand that the harmonic component seen in the applied phase current changes with the magnitude of *d* and *q* axis current.

From, (2.8) it can be seen that when current is mainly *iq* (or *id* =0), the actual *iq* has mainly $2n^{th}$ order ripple. Whereas when *iq* is nearly zero, *iq* will have predominantly n^{th} order ripple. Similarly, when *id* is nearly zero, *id* has $2n^{th}$ order ripple and when *id* is nearly zero *id* will have mainly n^{th} order ripple.

2.3.2 Effect of position error on torque

In this section, we analyze the effect of the position error in the generated torque. The torque developed in an IPMSM motor can be written as:

$$T_d = \frac{3}{2}\left(K_e iq + iqid\left(L_q - L_d\right)P\right) \tag{2.9}$$

The torque developed by the motor T_d thus is a function of *q* axis and *d* axis current. The objective is to understand how the ripple content in the *q* axis and *d* axis current generated due to the position error affect the developed torque. In order to understand this effect, the expression for *iq* and *id* obtained in (2.8) is substituted in (2.9). The torque developed can thus be simplified and the resultant torque developed T_d' is shown in the Appendix A. In general the resultant torque generated has an average torque component and ripple component and can be expressed as:

$$T_d' = T_{DC} + \sum_{m=1}^{4} T_{Rm}\cos(m\, n\theta_m) \tag{2.10}$$

The expression shows that for a given n^{th} order position error the torque generated has harmonic terms from n^{th} to $4n^{th}$ order. This analysis also shows that the torque ripple changes as a function of both *id* and *iq* for a given position error.

To maximize the torque for a given peak current I_p the *iq* and *id* can be calculated as

$$id = -\frac{3K_e}{8\,krc} + \frac{1}{2}\sqrt{\left(\frac{3K_e}{4krc}\right)^2 + 2I_p^2} \tag{2.11}$$

$$iq = \sqrt{I_p^2 - i_d^2}$$

where:

$$krc = \frac{3P}{2}(L_q - L_d)$$

Analyzing the ripple component further, it can be seen that the major contributors of the ripple will be the n^{th} and $2n^{th}$ order terms. The rest of the harmonic content will be considerably smaller. From Appendix A it can be seen that the *id* has a more dominant effect on the n^{th} order torque ripple and *iq* has a more dominant effect on the $2n^{th}$ order torque ripple. Appendix A also shows that the magnitude of the $3n^{th}$ and the $4n^{th}$ order ripple is much less compared to the n^{th} and $2n^{th}$ order. We can also state that the magnitude of $2n^{th}$ order ripple is less than the n^{th} order ripple for a given current. It should be noted that the effect of a given position error on the torque ripple generated will be less in a PMSM machine when compared to an IPMSM machine.

It should be noted that, in reality, the L_d and L_q values also change with current due to saturation. This effect can be modelled using Finite element analysis and the values may be used in actual calculation of current.

2.4 Results

2.4.1 Model results

An 8-pole current controlled IPMSM drive model was setup in Simulink to analyze the various effects of the position sensor error. The erroneous motor position is used in calculating the phase voltage to be applied and also in the conversion of phase current to *dq* current used for

current control. The position is injected with different harmonics to study its effect on motor current and torque. In the initial analysis, the motor was run at constant speed with a current command of *iqcmd* = 60A and *idcmd* =0A. In order to avoid confusing the effect of position error with the electromagnetically created torque ripple, a fifth order motor mechanical position error of amplitude of 0.5 degree was injected in the position. This will help to understand the current and torque ripple harmonics created by a given harmonic order in the position error. Figure 2.5 and Figure 2.6. plots the effect of the 0.5 degree position error on the measured *dq* currents. It can be seen that the main harmonic order developed in the *q* axis current is tenth order and in the case of *d* axis current it is fifth order. The result obtained is in accordance with (2.8) developed in the previous section, as we can see that if *id* is very small the major component in the resultant *q* axis current is n^{th} order while the major component in the resultant *d* axis is $2n^{th}$ order.

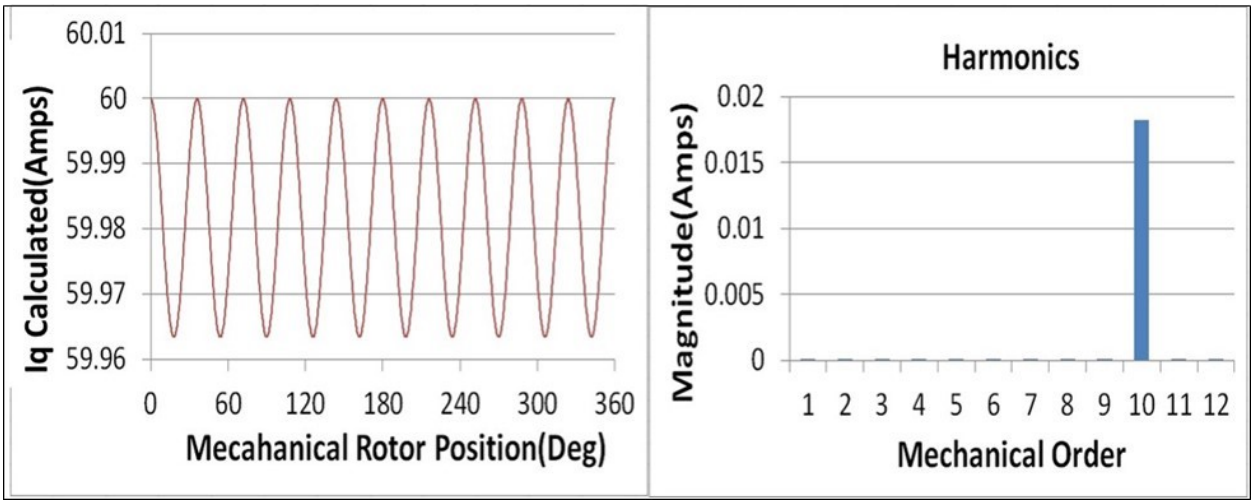

Figure 2.5: Effect of 0.5 deg 5th order position error on *q* axis current for *iqcmd*=60 and *idcmd*=0

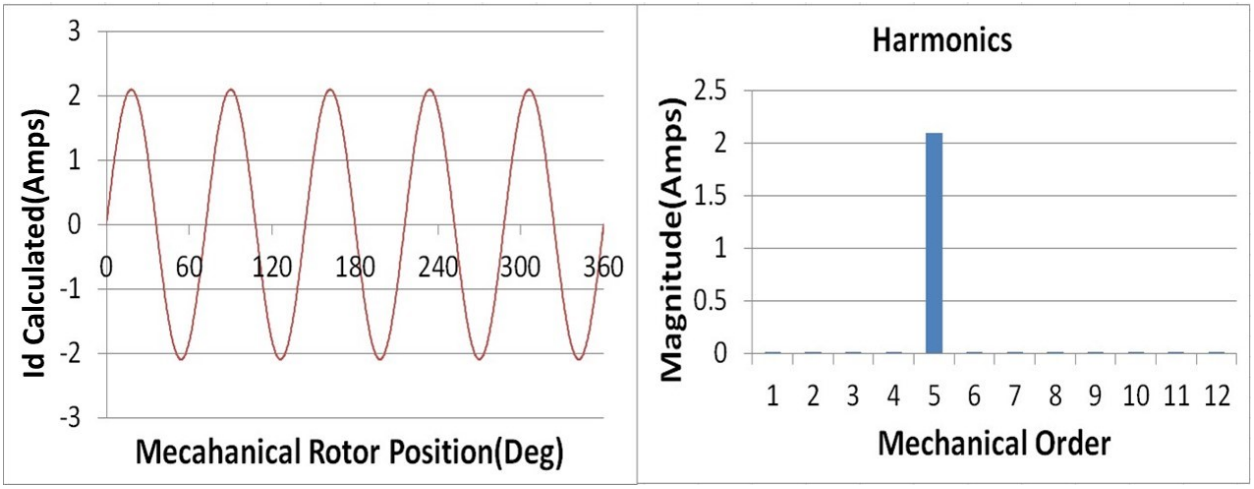

Figure 2.6: Effect of 0.5 deg 5th order position error on *d* axis current for *iqcmd*=60 and *idcmd*=0

Figure 2.7 and *Figure 2.8* shows the effect of fifth order position sensor error on the current developed when the commanded current is given as *iqcmd* = 0 and *idcmd* = 60. The figure shows that the major harmonic in the resultant *q* axis current in the machine is n^{th} order and the major component in the resultant *d* axis current is $2n^{th}$ order. This result shows that the ripple produced in the current changes with the different levels of *idcmd* an *iqcmd* current.

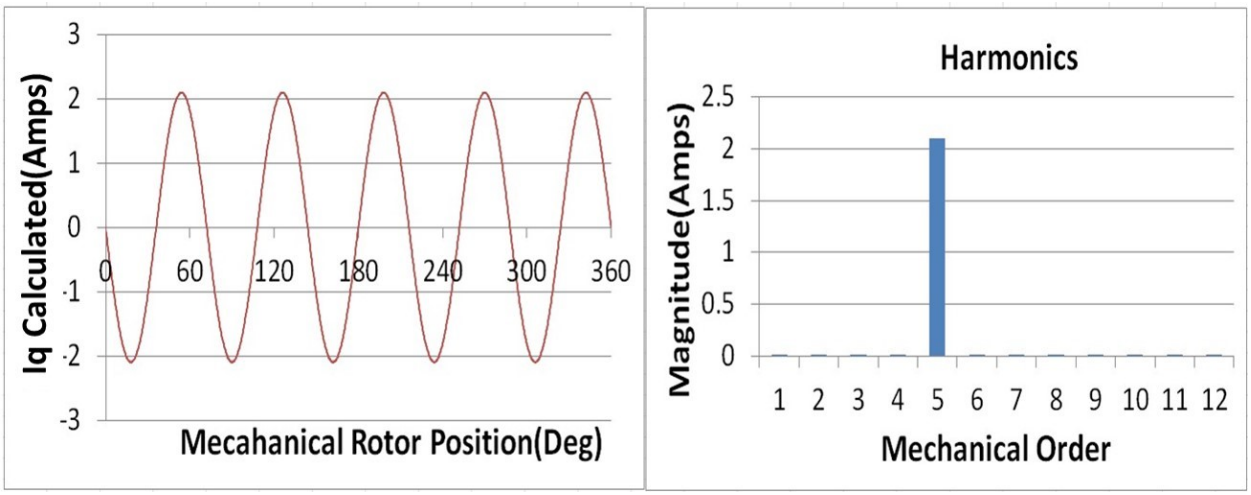

Figure 2.7: Effect of 0.5 deg 5th order position error on *q* axis current for *iqcmd*=0A and *idcmd*=60A

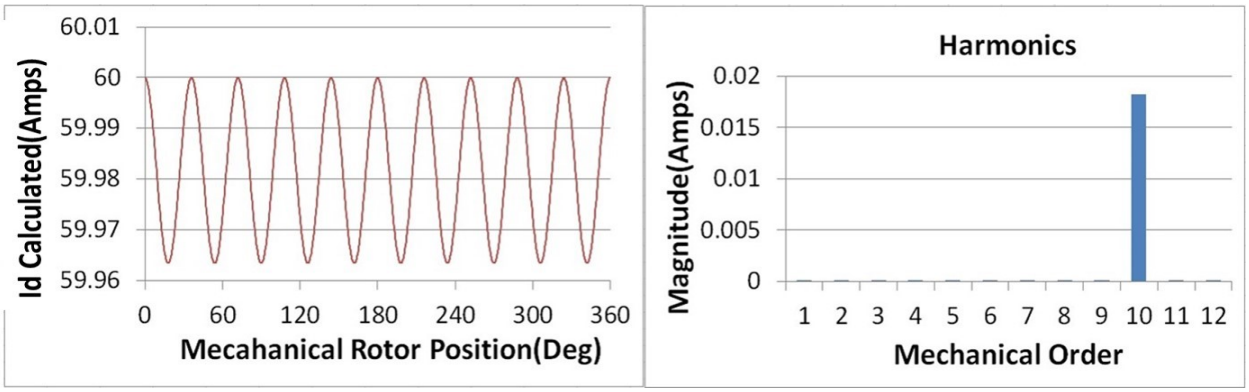

Figure 2.8: Effect of 0.5 deg 5th order position error on *d* axis current for *iqcmd*=0A and *idcmd*=60A

The *Figure 2.9*. shows the effect of 0.5 deg fifth order position error on the torque developed and its harmonic content in the case when the commanded *idcmd* =0A and *iqcmd* =60A. It can be observed that the major harmonic content in the torque ripple is n^{th} and $2n^{th}$ order. Therefore the resultant torque ripple has 5th and 10th order harmonic. From Appendix A, it can be noted that when *idcmd* = 0A the largest contributor to the n^{th} order harmonics is from the iq_i^2 term:

$$T_n = \left(0.75Pk1\left(L_q - L_d\right) - 0.281Pk1^3\left(L_d - L_q\right)\right) iq_i^2 \tag{2.12}$$

For the $2n^{th}$ order harmonics the main contributing term is:

$$T_{2n} = 0.375 * iq_i * K_e * k1^2 \tag{2.13}$$

Where: $k1 = P * \hat{\theta}_{er}$

For the machine under study, the magnitude of the n^{th} order component is greater than the magnitude of the $2n^{th}$ order component. The result obtained therefore is in accordance with the (2.10) developed in the previous section. *Figure 2.10* shows the effect of the fifth order position error on the torque developed and its harmonic content in the case when *id*=60A and *iq*=0A. In this case the harmonic content in the torque ripple is n^{th} order and thus the torque ripple is predominantly 5th order. The magnitude of the 5th order is much higher when compared to the previous scenario (*id*=0A, *iq*=60A). It can be seen here that the $2n^{th}$ order torque ripple is not

present which is in accordance with the equation given in Appendix A as we can see that the T_{R2} component of the ripple is function of iq_i and product of $iq_i id_i$

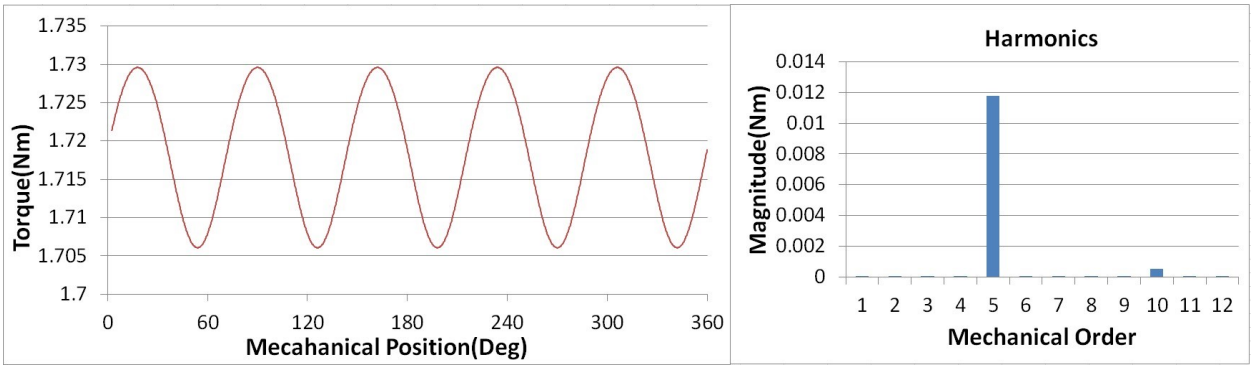

Figure 2.9: Effect of 0.5 deg 5th order position error on the measured torque for *iqcmd*=60A and *idcmd*=0A

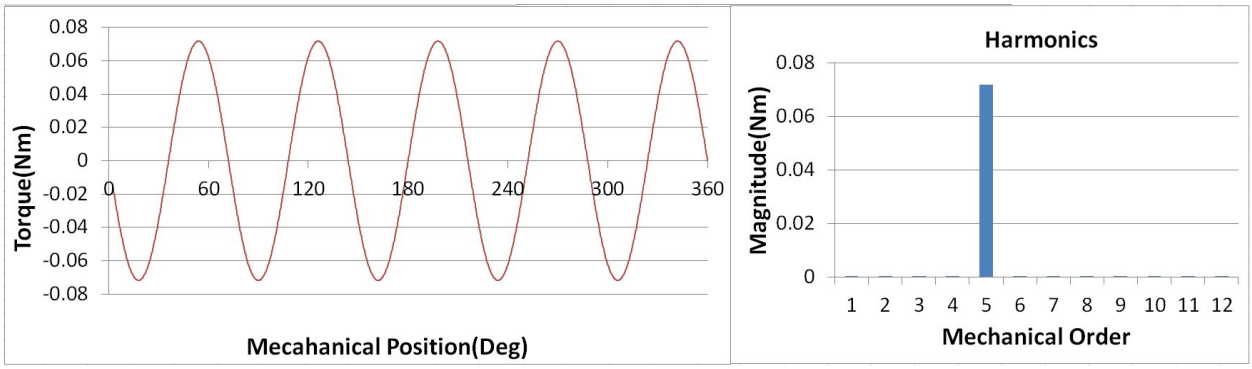

Figure 2.10: Effect of 0.5 deg 5th order position error on the measured torque for *iqcmd*=0A and *idcmd*=60A

2.4.2 Experimental results - effect on phase current

Tests were performed on a 3-phase 12-slot 8-pole IPMSM motor that uses a hall-effect position sensor. The various motor parameters are given in Appendix A. An Infineon TC23X microprocessor is used for the signal analysis of the motor position signal and for generating current control commands. A high resolution master encoder was attached to the shaft of the motor to provide the reference position. A fifth order mechanical position error of 0.5 degrees was added to the actual position in the controller in order to create the position sensor error. A high resolution torque sensor was attached to the motor in order to measure the torque generated. The torque sensor

has an accuracy of +/-2mNm and bandwidth of 1000Hz (-3dB). The mechanical system has much lower frequency response and that will be the limiting factor in the ability to measure developed torque of the machine at high speed. The effect of position error on the applied phase current is studied first. The phase current is measured at various current commands at a motor speed of 20 RPM. In order to verify with the mathematical model, the practical result obtained are matched with the model output. The results obtained in *Figure 2.11* clearly shows that a fifth order position error causes a tenth order harmonic in the measured *q* axis current and fifth order harmonic in the measured *d* axis current when commanded current is iq=60A and *id*=0A. This matches closely with the simulation results and the mathematical model obtained in this paper. Though the % error between the analytical results and the experimental results in the *q* axis is approximately 33%, the actual values are small and within the measurement resolution error. The current measurement resolution is 120mA with over sampling. The *d* axis current results is within 4% percent of the modelled results. *Figure 2.12* shows the effect on q and *d* axis current when commanded with iq=0A and *id*=60.A. It can be seen that the position error with fifth order causes a fifth order harmonic in the applied *q* axis current and tenth order harmonic in the applied

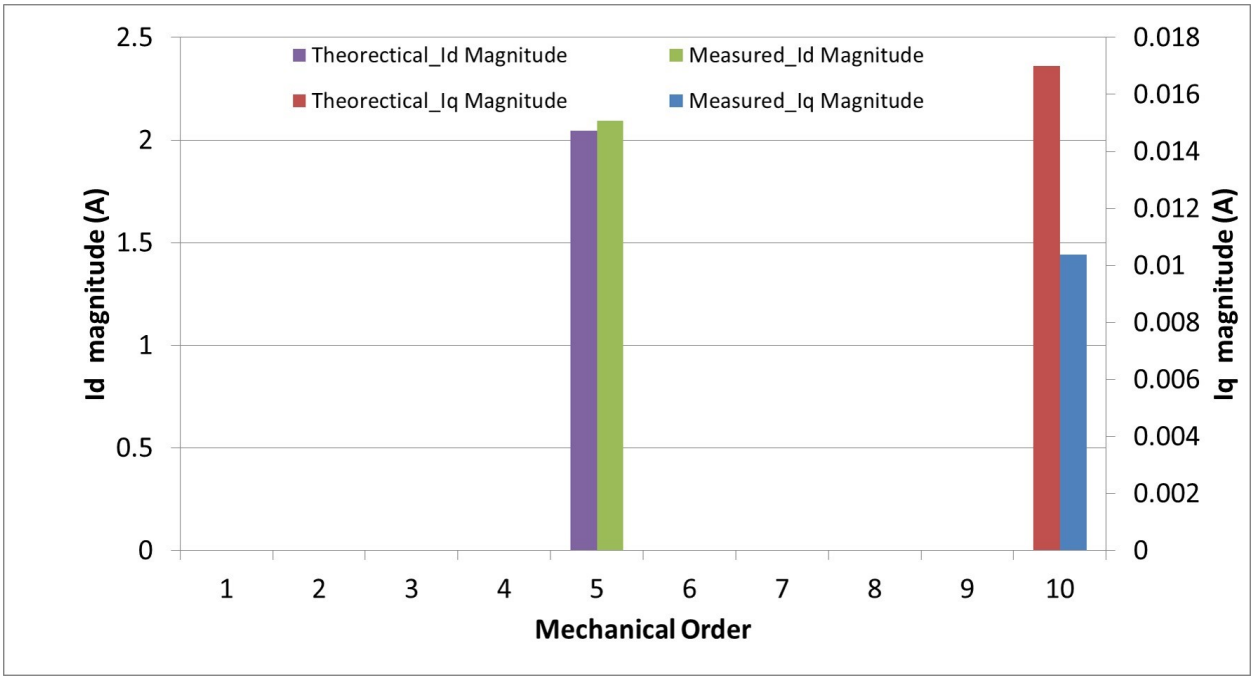

Figure 2.11: Effect of 0.5 deg 5th order position error on *q* axis and *d* axis current for *iqcmd*=60A and *idcmd*=0A

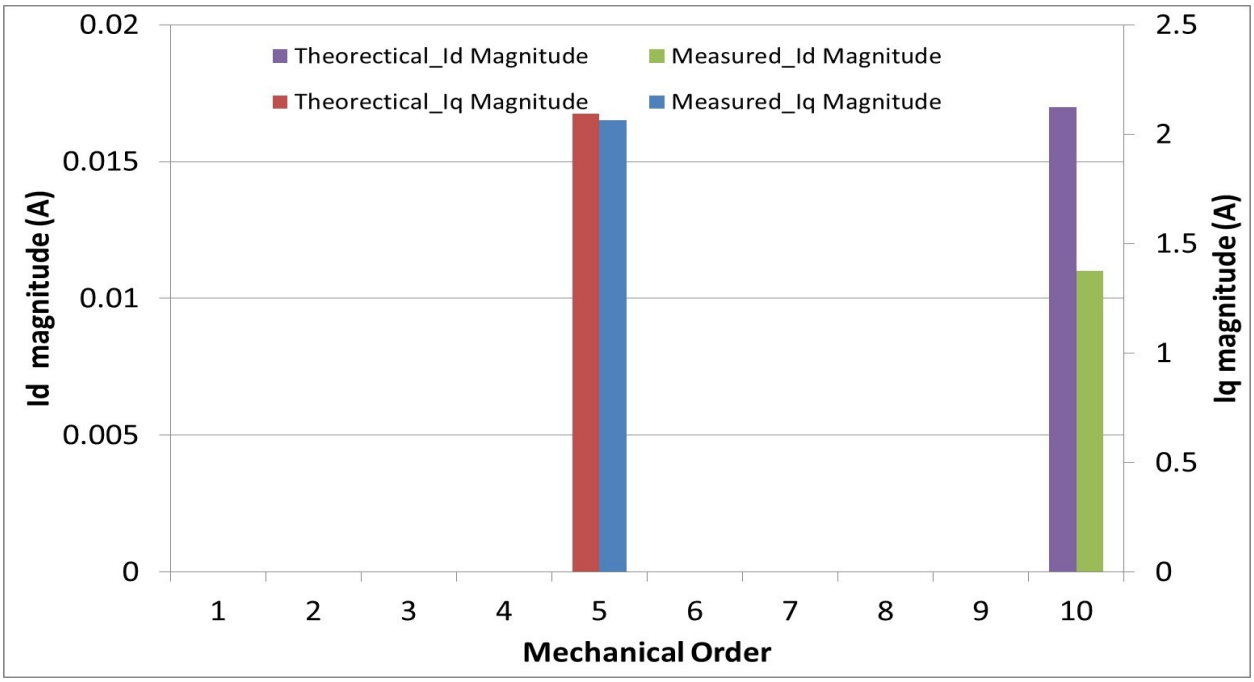

Figure 2.12: Effect of 0.5 deg 5th order position error on *q* axis and *d* axis current for *iqcmd*=0A and *idcmd*=60A

2.4.3 Experimental results-effect on torque generated

Next, we analyze the effect of position error on the generated torque. In order to validate the mathematical model, the analysis is done initially by varying the *q* axis current while maintaining a zero *d* axis current and vice versa. Once the mathematical model is verified the result at different motor operating points is also discussed. *Figure 2.13* shows the resultant harmonic content of the torque generated compared with the initial set of harmonic content without any position error injected when *iqcmd* =60 and *idcmd* =0. This shows that, when injected with a fifth order position error, it introduces both fifth order and a tenth order torque ripple. *Figure 2.14* shows the effect of the fifth and tenth order as a function of *iqcmd*. It compares the practical result with the actual model result showing that the mathematical model matches closely with the practical results obtained.

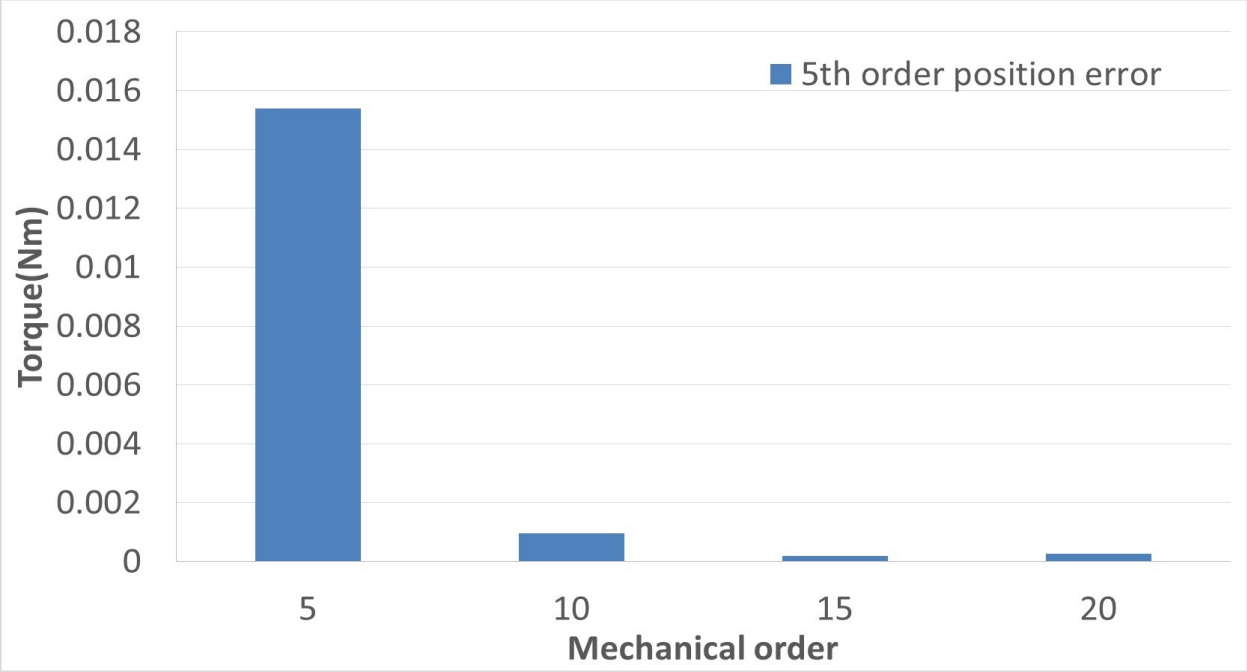

Figure 2.13: Effect of 0.5 deg 5th order injected position error on the measured torque for *iqcmd*=60A and *idcmd*=0A

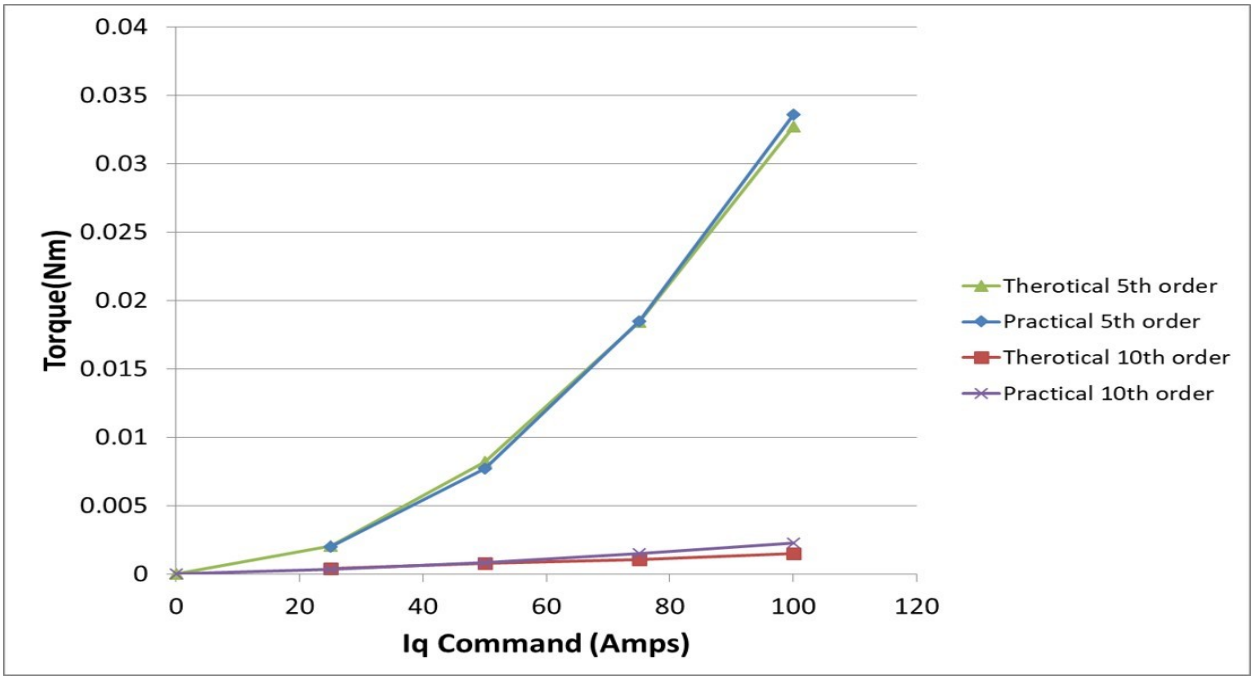

Figure 2.14: Effect of 0.5 deg 5th order position error on the measured torque for various *iqcmd* with *idcmd*=0A

In this second scenario, data is collected at various *d* axis current commands while maintaining a zero *q* axis current. The motor is commanded with *iqcmd* = 0 and *idcmd* = 60. The *Figure 2.15* shows the harmonics in the resultant measured torque compared with the harmonic content when no error was injected. As predicted by the model result, only 5^{th} order component is observed, which is much higher in magnitude than the previous scenario (*iqcmd* = 60 and *idcmd* = 0. *Figure 2.16* shows the effect of 5^{th} and 10^{th} order torque ripple as function of *idcmd*.. Figure 2.17 shows the effect of the 5^{th} and 10^{th} order torque ripple as function of torque command at 20RPM of motor. The analytical and practical results are well matched. The *id* and *iq* current is calculated using (2.11) for a given torque command.

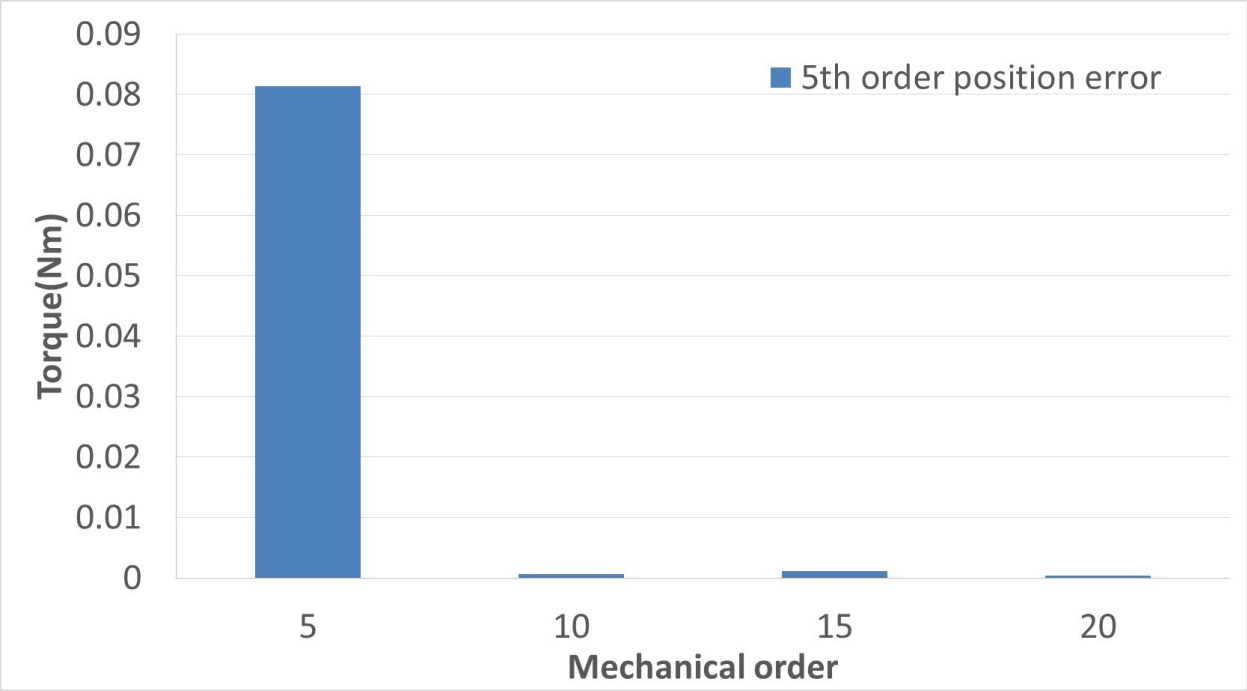

Figure 2.15: Effect of 0.5 deg 5th order position error on the measured torque for *iqcmd*=0A and *idcmd*=60A

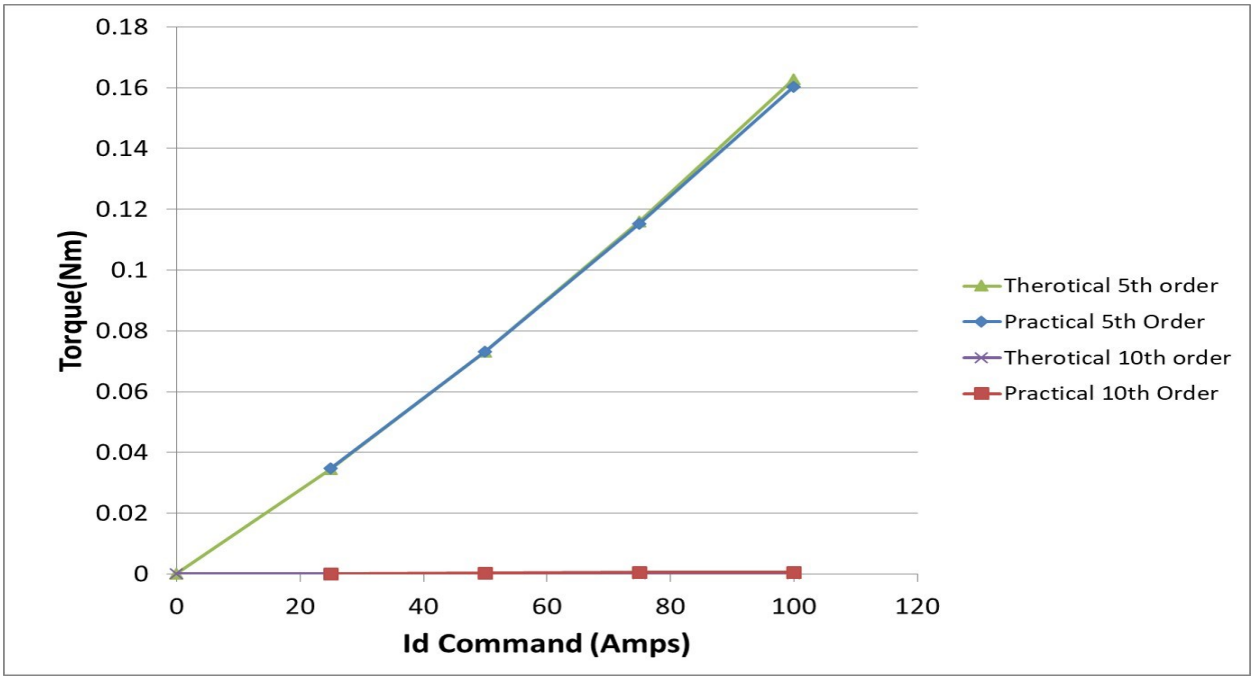

Figure 2.16: Effect of 0.5 deg 5th order position error on the measured torque for various *idcmd* with *iqcmd*=0A

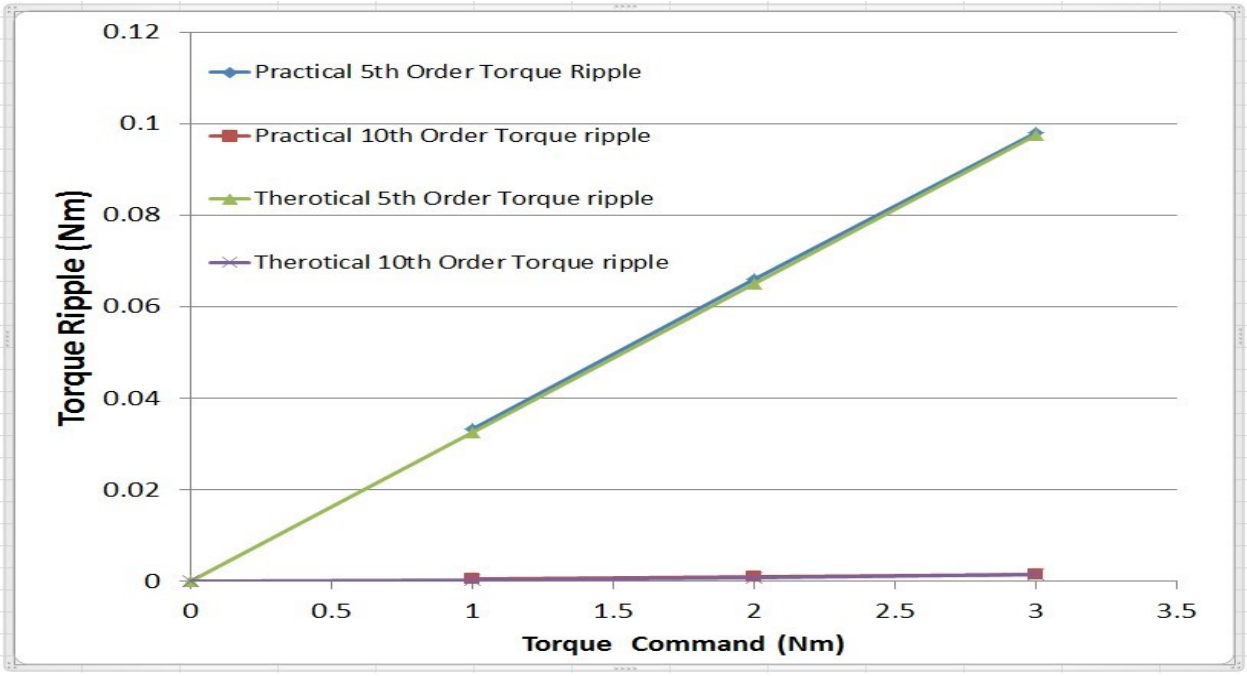

Figure 2.17: Effect of 0.5 deg 5th order position error on the measured torque for different torque level

We can conclude based on the results obtained above, that the effect of the position sensor error on the torque generated varies as a function of *idcmd* and *iqcmd* magnitude. The results also show that the main harmonic content in the torque ripple when injected with a position error of $n\theta_{err}$ are n^{th} and $2n^{th}$ order. Comparing the *Figure 2.14* and *Figure 2.16* it can be seen that the magnitude of the n^{th} order torque ripple is much higher with *idcmd* compared to the case of the *iqcmd* for a given current.

2.5 Practical sensor and error compensation

As seen in *Figure 2.1* the realistic error in the position will contain 2nd, 3rd, 4th and 16th orders with respect to mechanical revolutions of the rotor. Depending on the sensor technology, we may have other harmonics as well. In *Figure 2.1* the 24th and 48th order ripple are generated due to the induced voltage harmonics interacting with the current. For an 8-pole motor, the torque ripple generated due to voltage harmonic are 24th and 48th (6th and 12th electrical). It is expected that these

will be the major harmonics in the torque ripple generated. It can be seen that in addition to the 24^{th} and 48^{th} order ripple, several other harmonics are also present. However these may not all be attributed to the position error as other contributors such as current sensor error will also be present and produce undesirable torque ripple. In order to perform compensation, the sensor error is measured by comparing it to an optical based high precision external encoder as a reference. The compensation is applied to understand the sensor contributions. *Figure 2.18* shows various orders in the position sensor error used in the test motor. The position sensor error is first characterized with the high precision encoder. The major errors in this particular sensor were found as 2^{nd}, 3^{rd} and 16^{th} orders. From the analysis given in this paper, these errors will contribute to 2^{nd}, 3^{rd}, 4^{th}, 6^{th}, 16^{th} and 32^{nd} orders in the torque. The expected magnitudes of the torque ripple due to the sensor error present is compared with the actual torque ripple obtained before compensation in *Figure 2.19*. It was observed that the 4^{th} and 8^{th} order were much higher than expected. This is due to other contributing factors such as phase imbalance which effect the same orders but have a greater magnitude than the position error contribution. The sensor position errors are compensated for online by using the previously characterized sensor error. *Figure 2.20* shows the torque ripple after sensor errors are compensated. It was observed that the torque ripple magnitude of the compensated orders were minimized after compensation was applied. Note that magnitude of some of these components did go up, due to the fact that the vector subtraction of the ripple due to position error and due to other causes, such as cogging, resulted in larger magnitudes.

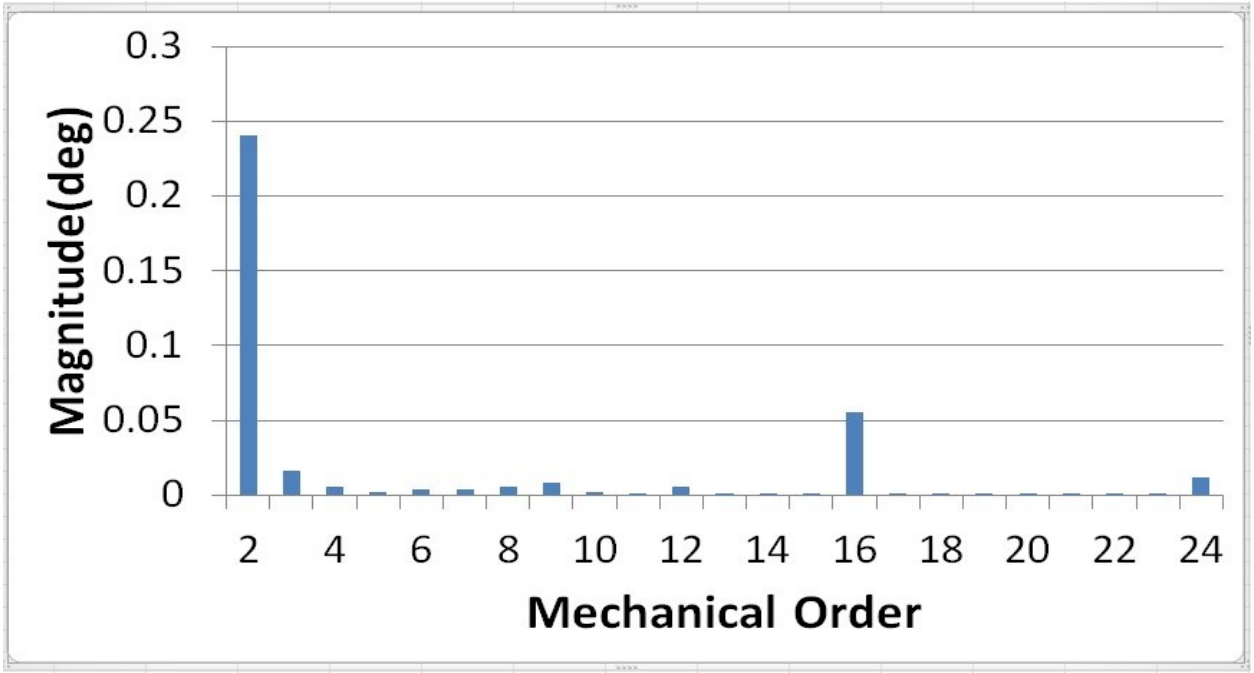

Figure 2.18: Measured position sensor error harmonics from the test motor

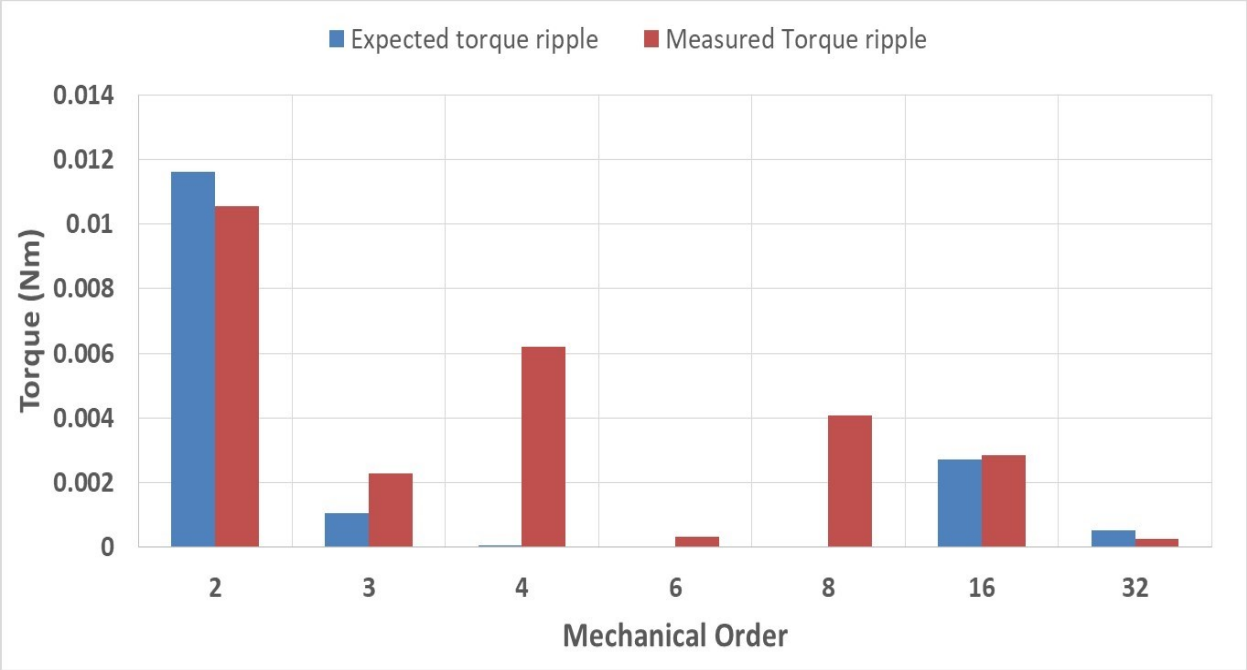

Figure 2.19: Theoretical torque ripple expected due to the measured position error in Fig.2.18 vs experimental torque ripple

Figure 2.20: Torque ripple with and without position error compensation

2.6 Conclusions

This chapter discussed the effect of position sensor error on the performance of a current controlled Permanent Magnet Synchronous Machine drive. The chapter gives a mathematical model for the effect of the position error on the generated current, and also quantifies the various harmonics generated in the current. It also studied the effect of the position error on the generated torque and gives the mathematical model for the same. This study thus gives insight into how the position error affect the torque ripple generated in an IPMSM drive, thereby helping to root-cause the various source of the harmonics seen in the generated torque other than the known electromagnetically created harmonics. In general it can be concluded that an n^{th} -order harmonic in the measured mechanical position creates n^{th} and $2n^{th}$ mechanical order ripple in the torque. The higher order ripple content is very small. Finally, the section shows typical position error harmonics present in practical sensors and the effect of position error compensation on the torque ripple generated. The study presented applies equally to PMSM/IPMSM current controlled motor drives. The position sensor error has a greater impact on torque ripple with *d* axis current. Thus

for IPM drives the impact of sensor errors is larger than SPM drives since IPM drives generally operate with higher *id*.

CHAPTER 3

Analysis of Inductance Variation in PM Machine

3.1 Introduction

From the last chapter it is clear that position error has detrimental effect in performance of PMSM/IPMSM machine. In redundant architectures as explained in Chapter 1, multiple sensors are used which add to the total system architecture, thus sensorless position estimation becomes a valuable cost reduction technique. The idea in this research is to track saliency of the machine to detect the position. Therefore it is of utmost importance to understand how inductance varies with respect to position. The aim of this chapter is to provide in-depth analysis of inductance variation including the effect of mutual inductance between the windings. A mathematical expression of the total phase inductance is developed. Section 3.2 introduces the configuration of the motor under study and begins with a simple single winding configuration. The objective of this part is to calculate the self and mutual inductances, and examine the effect of the parallel winding connections on the effective inductance. Section 3.3 will focus on connecting the parallel path and finding the equivalent phase inductance. The FE model analysis is compared with the experimental result to support the mathematical model obtained. Conclusions of this chapter are presented in section 3.4.

3.2 Single winding study

The motor used in this study is a 12-slot 8-pole motor. The motor winding is configured such that there are four parallel paths per each phase. Figure 3.1 shows the motor configuration of the 12-slot 8-pole motor with the parallel paths per phase, the letters refer to the phase, and the number corresponds to the parallel path. For example, A1 indicates the coil in phase A in parallel path 1. It is evident from Figure 3.1 that there are four parallel paths per phase. The objective of this section is to study the self-inductance of a single coil and understand the mutual effect between the windings on the other slots. For this study, the parallel paths in each phase are separated and thus the effect based on current on a single coil could be explored. The single coil study thus gives the basic understanding of the variation of the inductance of a single coil with the position. The test is done by passing current through the single winding as illustrated in *Figure 3.2*.

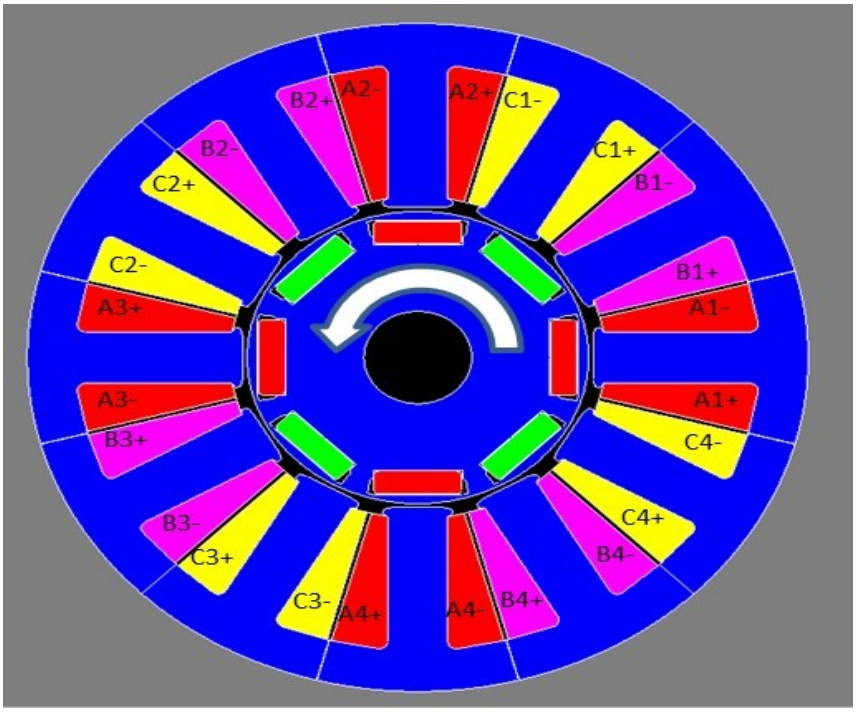

Figure 3.1: Motor slot and winding configuration of an 8-pole 12 slot IPM machine

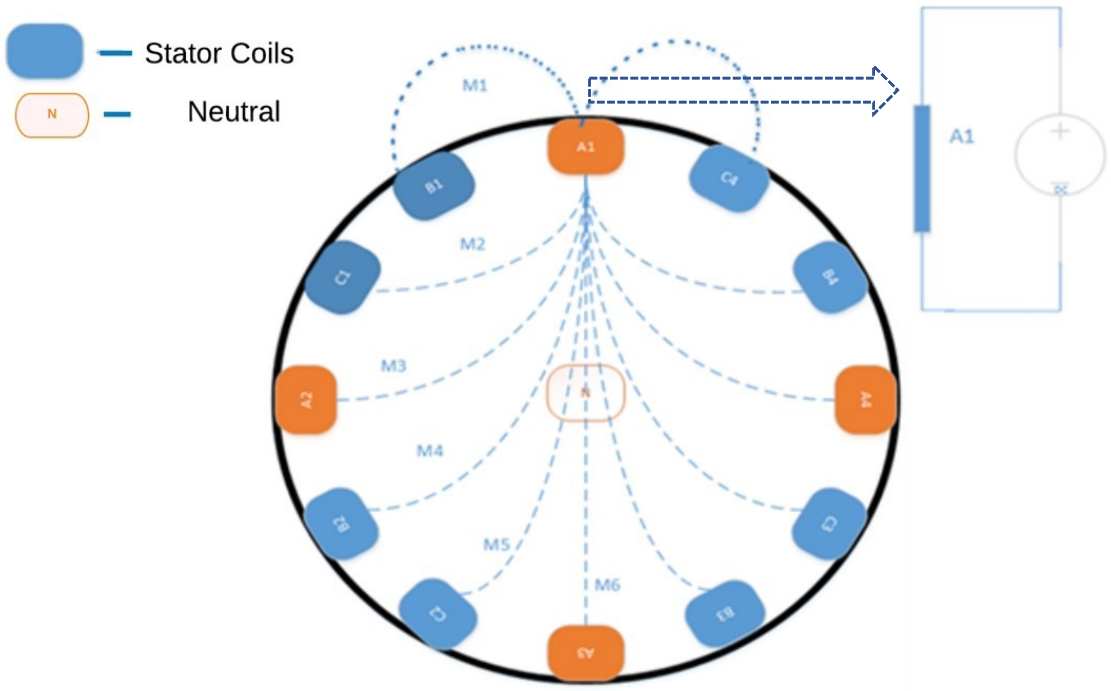

Figure 3.2: Stator coil representation showing the A1 coil through which the current is passed for single winding study

3.2.1 Self- inductance analysis

At first we will define the reference axis used for the analysis in this research. Figure 3.3 shows the motor reference axis which will be used for the analysis in this chapter. Sinusoidally distributed windings, Phases A, B & C are represented by a-a', b-b', c-c' respectively. Phase b and phase c coils are displaced 120 and 240 degrees respectively from the winding a-a' (Phase A).

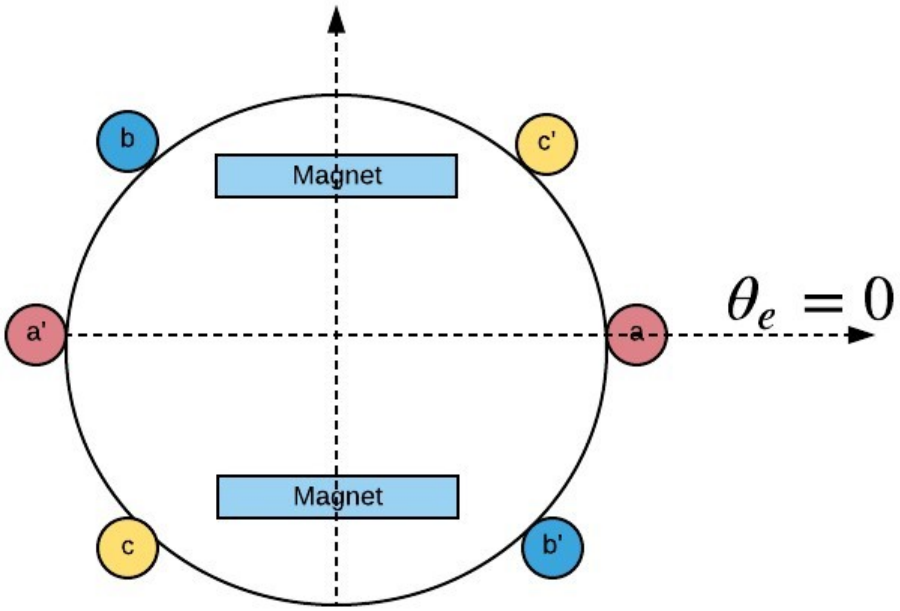

Figure 3.3: Motor reference axis definition used for the analysis

The expected self-inductance term [45] of a single coil has an average dc component L_0, 2nd order component of self-inductance term, L_2 and 4th order component of self-inductance, L_4 shown as:

$$L_{acoil} = L_0 + L_2 * cos(2\theta_e) + L_4 * cos(4\theta_e) \quad (3.1)$$

$$L_{bcoil} = L_0 + L_2 * cos\big(2(\theta_e - 120)\big) + L_4 * cos(4(\theta_e - 120))$$

$$L_{ccoil} = L_0 + L_2 * cos\big(2(\theta_e - 240)\big) + L_4 * cos(4(\theta_e - 240))$$

where $L_{acoil,}$ L_{bcoil}, L_{ccoil} is the self-inductance of a single coil in phase A,B and C respectively and θ_e is the angle in electrical degrees.

To measure the inductance, the voltage V_{acoil}, is applied across one winding in phase A and the neutral as shown in *Figure 3.4*. Current flowing through the phase A is measured as I_{acoil}. Self-inductance $L_{acoil,}$ can be calculated at any rotor position from zero to 360 degrees using the expression:

$$L_{acoil} = \frac{V_{acoil}}{\frac{dI_{acoil}}{dt}} \tag{3.2}$$

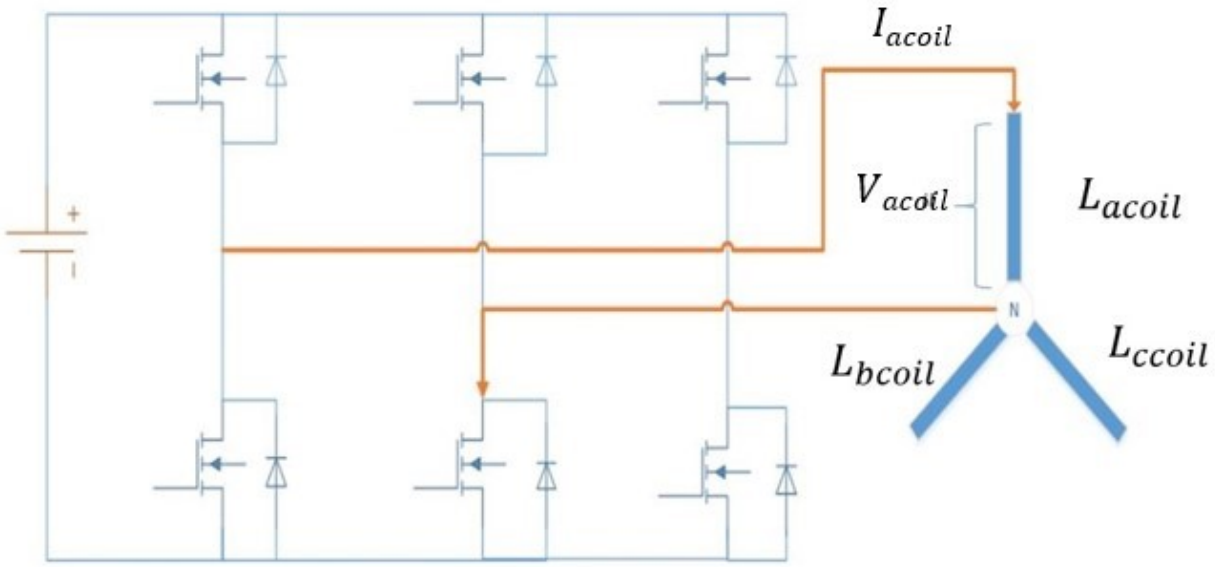

Figure 3.4: Test setup to determine self-inductance of single coil

The self-inductance $L_{acoil,}$ of the phase A coil, is plotted at various positions in *Figure 3.5*. The curve fit data plotted shows how the self-inductance varies with position. Similarly, the self-inductance for Phases B and C can be calculated. The measured result indicates that the self-

inductance of a single coil is of the form expressed in equation 3.1, thus the components L_0, L_2 and L_4 of the single coil can be determined.

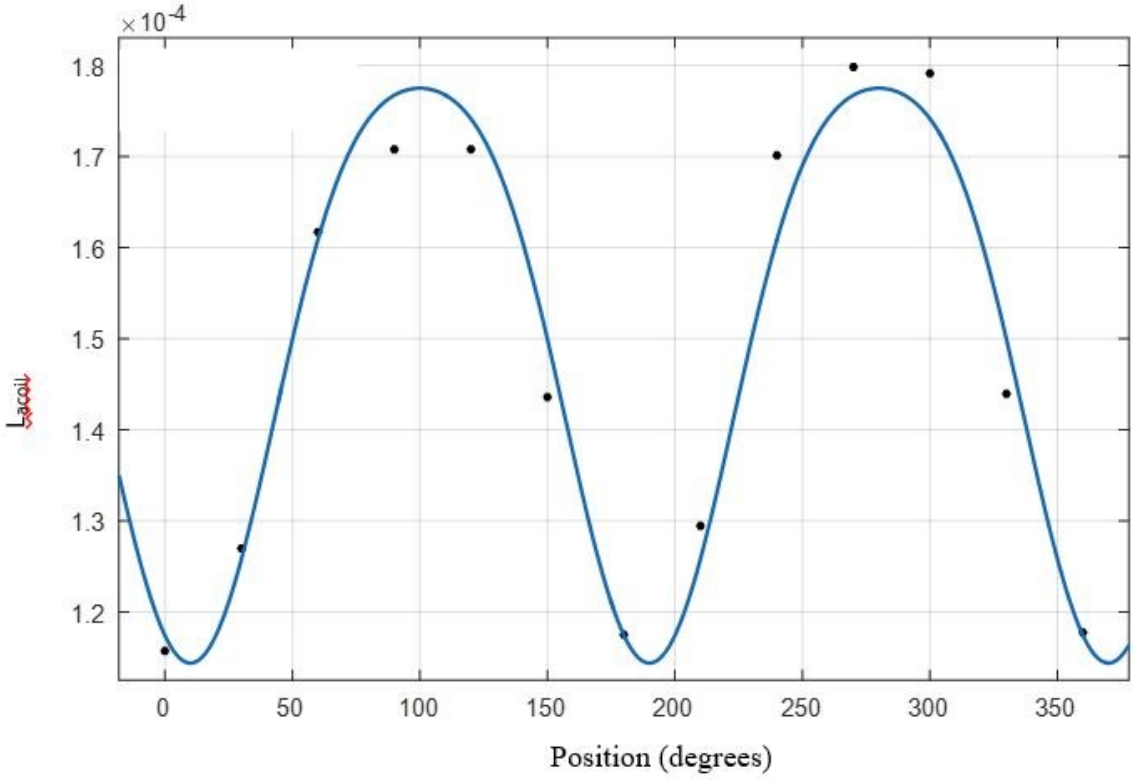

Figure 3.5: Practical measurement of self-inductance (L_{acoil}) at various positions with the best fit curve

Finite Element (FE) analysis is used to validate the values obtained for L_0, L_2 and L_4. In the FE analysis the total flux linkage is obtained by passing the current of 1A through the coil A1 and rotating position from zero to 360 degrees. The inductance at various positions is calculated by flux linkage per ampere. The inductance obtained for a single coil in phase A is shown in *Figure 3.6*. The Fourier analysis on the obtained inductance is used to estimate the self-inductance parameters L_0, L_2 and L_4. The parameters of the self-inductance term obtained through FE analysis is compared with the experimental results in Figure 3.7.

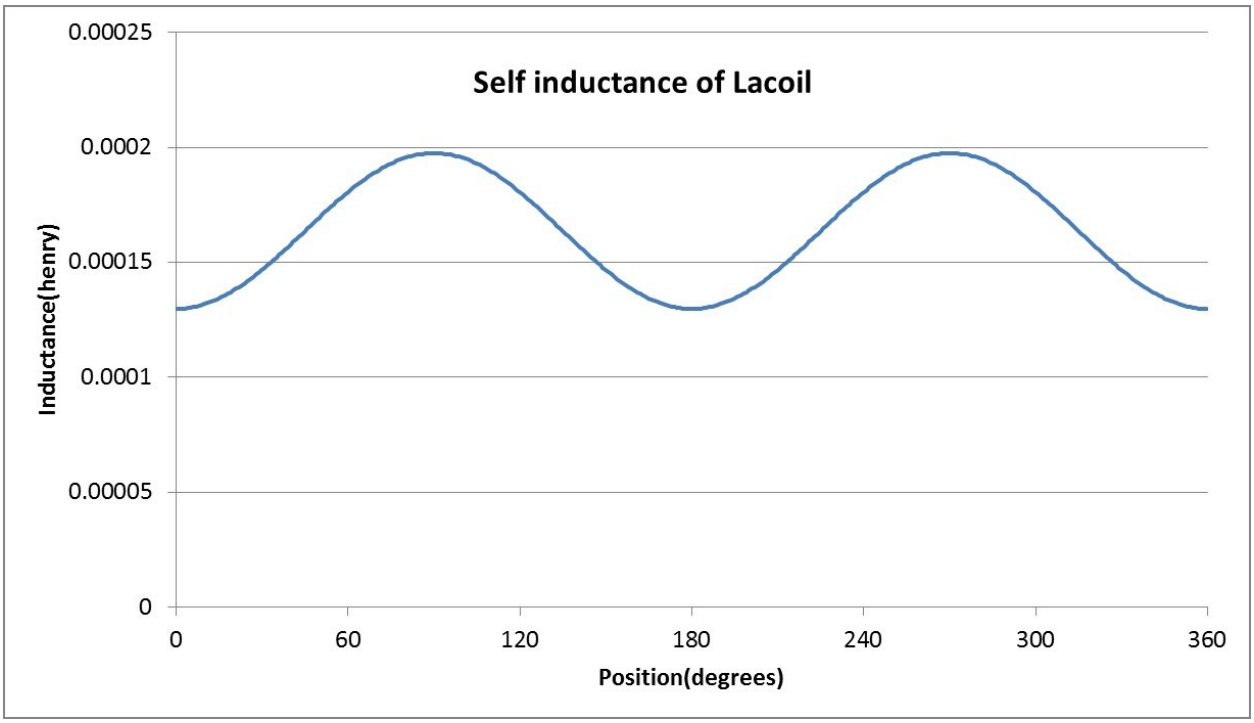

Figure 3.6: FE analysis result of self-inductance (L_{acoil}) at various positions

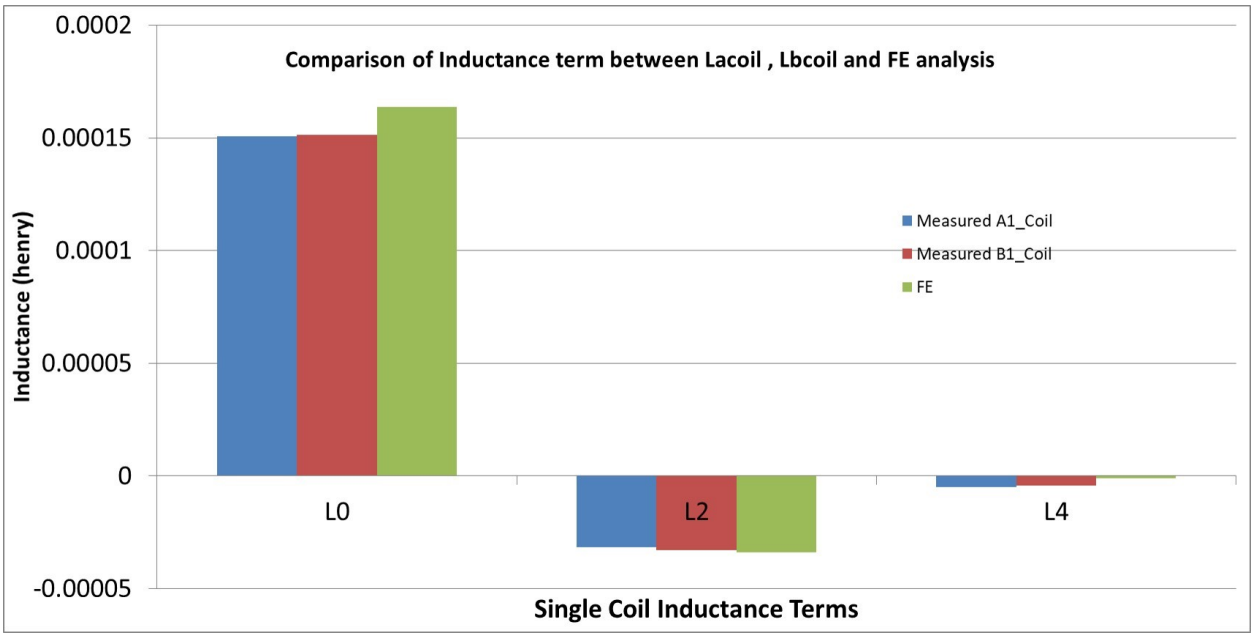

Figure 3.7: Comparison of self- inductance parameters measured vs. FE analysis

From the results obtained above the following conclusions can be made:

1. The self-inductance parameter L_0 obtained from the experimental results is within 7% match of the results from the FE analysis, while the components L_2 and L_4 are within a 2% match of the FE value. The differences may be due to manufacturing tolerance variations in the air gap and other mechanical parameters.

2. The self-inductance takes the form as stated in (3.1).

3. The self-inductance term primarily consists of the DC and the second order term. From the result obtained, we can see that the magnitude of L_4 is only 2% of the magnitude compared to L_0, while L_2 is 20% of the magnitude of the L_0. Therefore, fourth order and higher order terms are considered negligible.

3.2.2 Mutual inductance analysis

In this section analysis is performed in order to study the effect of mutual inductance of coils that are one and two slots apart. The effect of mutual inductance for coils that are three slots apart or

more is negligible and therefore not considered in this analysis. Terms M1 and M2 are defined as the mutual inductance of coils one and two slots apart respectively.

The expected form of the mutual inductance M1 and M2 can be given as [45]:

$$M1 = M_{01} + M_{21} * \cos(2(\theta_e - 240)) + M_{41} * \cos(4(\theta_e - 240))$$
$$M2 = M_{02} + \mathrm{M}_{22} * \cos\big(2(\theta_e - 120)\big) + \mathrm{M}_{42} * \cos\big(4(\theta_e - 120)\big) \quad (3.3)$$

where M_{01} and M_{02} denote the dc component of mutual between the two coils one slot and two slots apart respectively. M_{21}, and M_{22} denotes the second-order component of mutual between the two coils one slot and two slots apart respectively.

Revisiting the single winding study, see Figure 3.2, current is passed through the A1 coil, with coils B1 and C1 one and two slots apart respectively. Mutual inductance M1 and M2 are calculated by measuring the rate of change of current through the coil A1 and measuring the induced voltage V_{1w} across the coil B1 and neutral and voltage V_{2w} across the coil C1 and neutral, respectively. The voltages are measured at various rotor positions. Figure 3.8 shows the experimental setup to measure the mutual inductance M1 and M2. The expressions for the calculation of M1 and M2 can be given as:

$$M1 = \frac{V_{1w}}{\frac{dI_{coil}}{dt}} \quad M2 = \frac{V_{2w}}{\frac{dI_{coil}}{dt}} \quad (3.4)$$

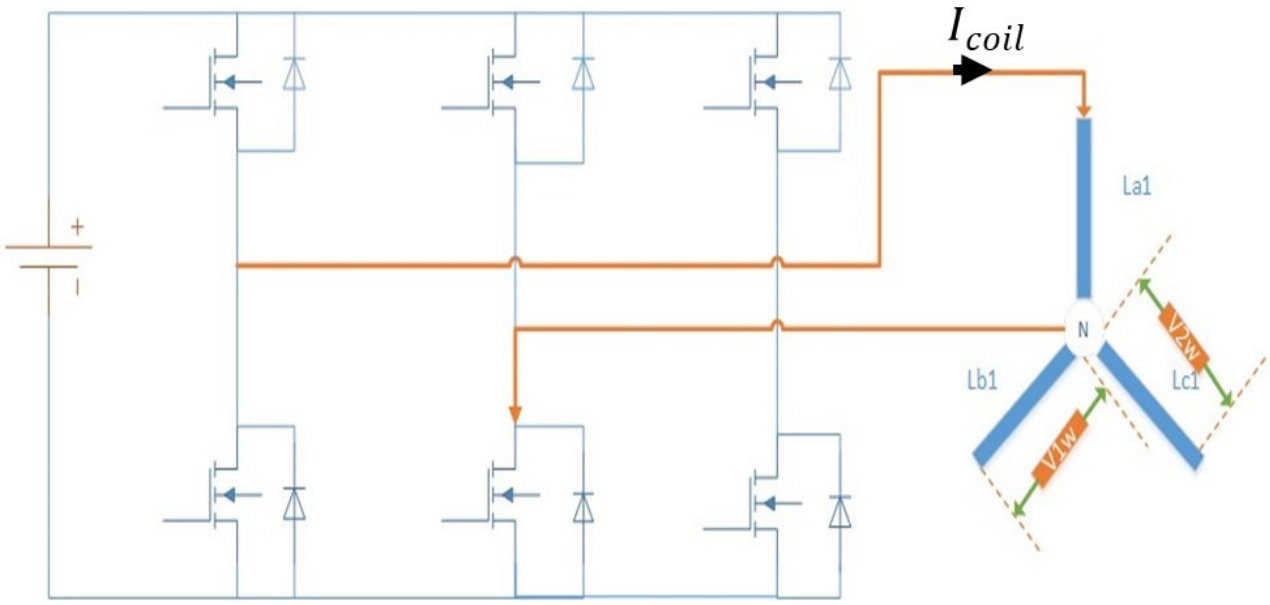

Figure 3.8: Test setup to determine the mutual inductance between coils

The measured mutual inductance of two coils that are one slot and two slots apart are given in Figure 3.9 and Figure 3.10 respectively. The solid line in the figures shows the best fit curve for the experimental results. The Fourier analysis of the inductance obtained gives us the mutual inductance components $M_{01}, M_{21}, M_{41}, M_{02}, M_{22}, M_{42}$ as expressed in (3.3). It can be seen that the magnitude of the mutual inductance two coil apart is 10 time smaller than the magnitude of inductance 1 coil apart. Therefore it can be concluded that the effect of mutual inductance from the coil 2 slots apart, is negligible.

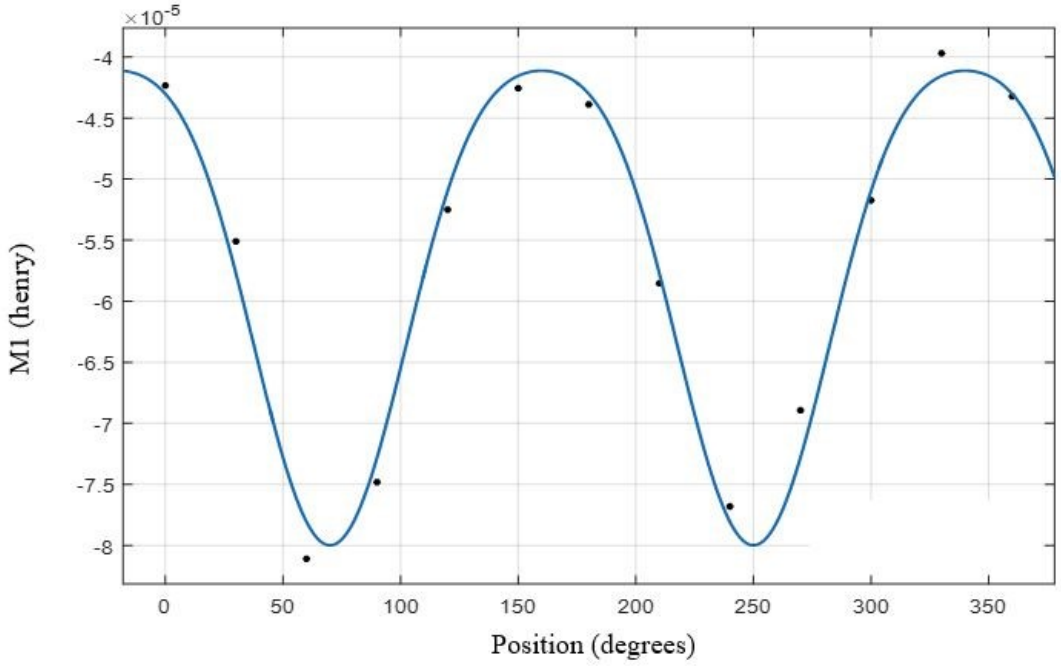

Figure 3.9 Measured mutual inductance between two coils one slot apart and the best curve fit cosine curve with dc, 2nd and 4th order harmonic

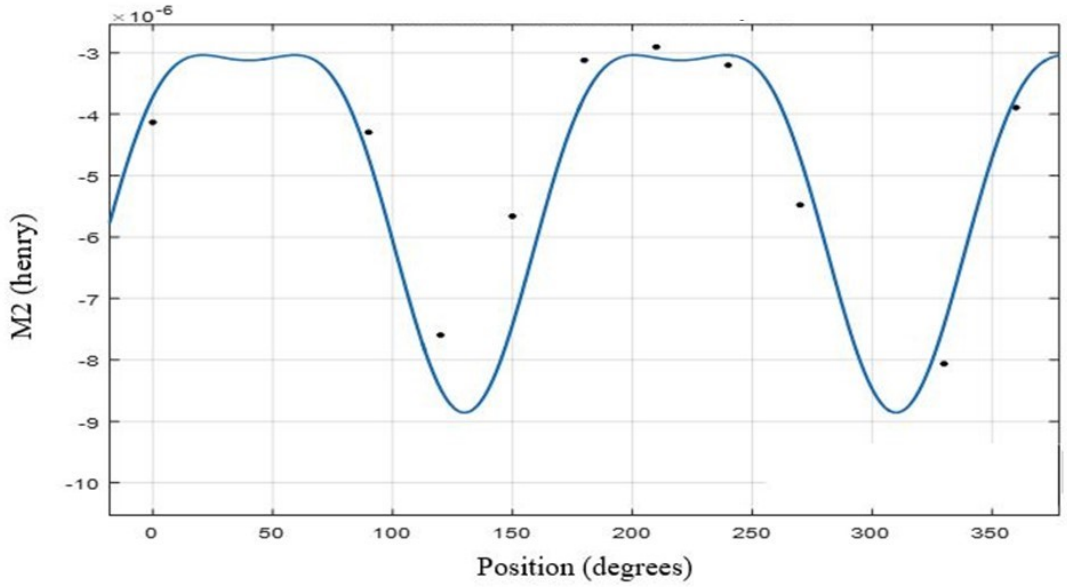

Figure 3.10: Measured mutual inductance between coils that are two slot apart the best curve fit cosine curve with dc, 2nd and 4th order harmonic

Similar to the self-inductance study, FE analysis is used in finding the total flux linkage at various rotor positions in B1 and C1 coil when 1Amp of current is passed through the A1 coil. Flux linkage per ampere determines the mutual inductance. The FE result of the mutual inductance for coil one slot and two slots apart are shown in Figure 3.11 and Figure 3.12 respectively. Table 3.1 shows the comparison of the mutual inductance parameters between FE and experimental data.

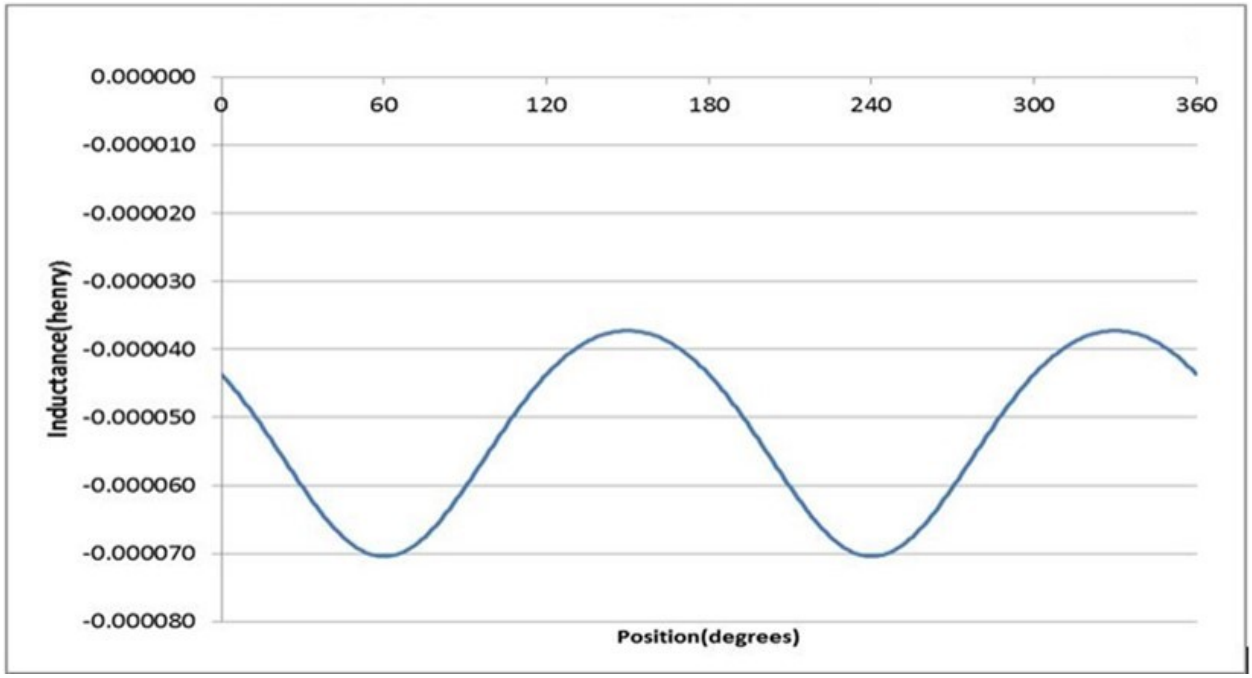

Figure 3.11: Mutual inductance of coil between two coils one slot apart using FE analysis

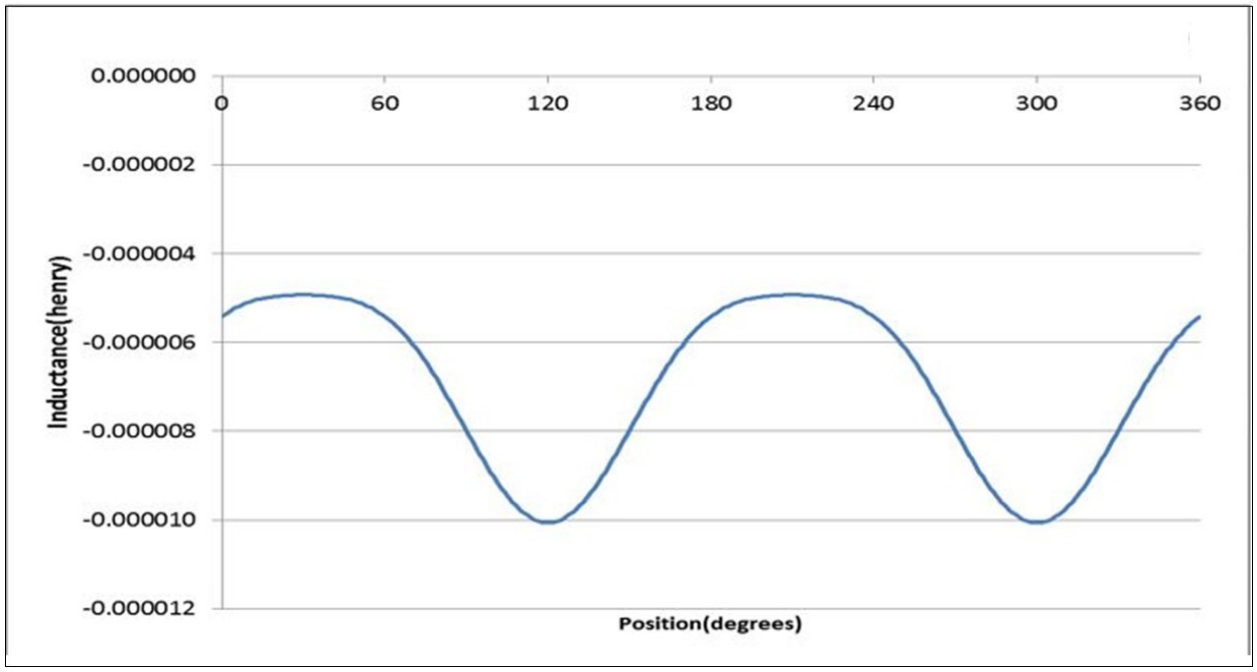

Figure 3.12: Mutual inductance of coil between two coils two slot apart using FE analysis

Term	**FE(μH)**	**Measured(μH)**
M_{01}	-52.5	-54.01
M_{02}	-6.9	-5.076
M_{04}	-1.25	-2.5

Table 3.1: Comparison of FE vs measured mutual inductance of coil 1 slot apart

Following observations are noted from the result above:

1. The mutual inductance between the coils one slot and two slots apart take the form found in (3.3).
2. The magnitude of the mutual inductance of the coil two slots apart is 10 times less than the magnitude of the mutual inductance one slot apart. Therefore it can be concluded that the effect of mutual from coil 2 slot apart is negligible and therfore will be ignored in further analysis.
3. The FE and the experimental results of the Mutual inductance parameter M_{01} match within 2%.

3.3 Phase inductance study

In this section, the primary objective is to model the total phase self and mutual inductances and obtain the values of all related parameters. All the parallel paths of each of the phases are connected

in this study. The idea in this section is to use the parameters derived from the single coil study to obtain the parameters for the total self and mutual phase inductance. The model developed is verified using FE analysis as well as experimental data.

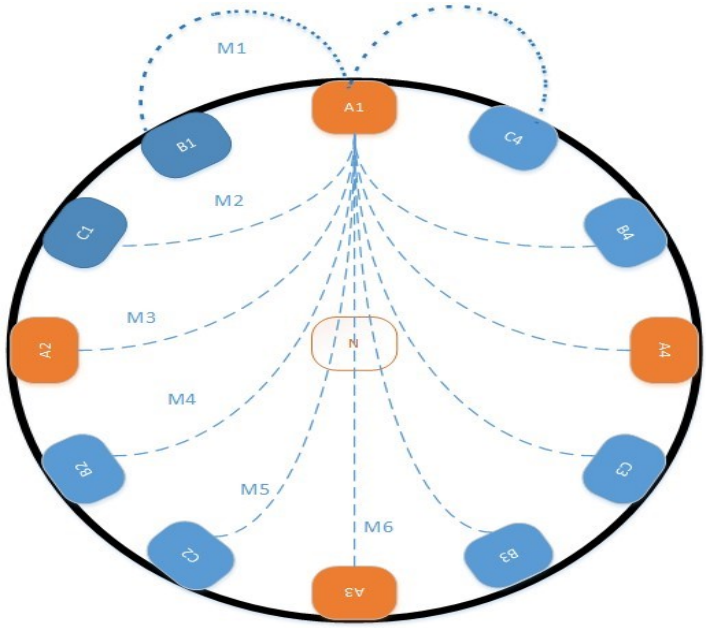

Figure 3.13: Representation of stator coils in the 8pole 12 slot motor

3.3.1 Self-inductance analysis

The objective of this section is to model the total self-inductance of a phase. In general, the total phase inductance will be of the form [45]:

$$L_a = L_{s0} + L_{s2}\, cos\, 2\theta_e \; + \; L_{s4}\, cos\, 4\theta_e \tag{3.5}$$

$$L_b = L_{s0} + L_{s2}\, cos\, 2(\theta_e - 120) + L_{s4}\, cos\, 4(\theta_e - 120)$$

$$L_c = L_{s0} + L_{s2}\, cos\, 2(\theta_e - 240) + \; L_{s4}\, cos\, 4(\theta_e - 240)$$

Where L_{s0} represent the dc component, L_{s2} and L_{s4} represent the second and fourth order components of the self-inductance. To understand the relationship between the parameters of the total phase self-inductance and the self-inductance parameters developed for single coil, consider the case for Phase A. Assuming balance system, if we inject a current in phase A it equally divides

in the four parallel paths. From Figure 3.13 it can be seen that the A1, A2, A3, and A4 coils are in the slot 0, 3, 6, and 9 respectively. It is also noted that for the A1 coil, the mutual inductance with the coil A2 is the same as the mutual with coil A4, as both are three slots apart. Recalling that the magnitude of mutual inductance of coils two or more slots apart are insignificant, they are therefore are not considered in this model. Thus the total voltage across the phase can be expressed as:

$$v_{ph} = \frac{1}{4}\frac{d(Ls)i_{ph})}{dt}$$

Where: (3.6)

$$Ls = (L_0 + L_2 cos2\theta_e + L_4 cos4\theta_e)/4$$

The v_{ph} is the voltage across the phase and neutral, and i_{ph} is the current passed through the phase as shown in *Figure 3.14*. From 3.5, the dc and the harmonic components of the total phase self-inductance can be expressed in terms of the single coil parameters (neglecting mutual inducatance from coils two or more slots apart) as:

$$L_{s0} = L_0/4 \quad (3.7)$$

$$L_{s2} = L_2/4$$

$$L_{s4} = L_4/4$$

The phase self-inductance is measured by applying the voltage across the phase A and neutral with phase B and C being open, such that phase A coils are the only one linking with the flux. Figure 3.14 shows the test setup where L_a, L_b, L_c denotes the total self-inductance of phase A, B and C respectively. The current through the phases are measured, and the self-inductance is calculated at various rotor positions using the expression:

$$L_{ph} = \frac{v_{ph}}{\frac{di_{ph}}{dt}} \tag{3.8}$$

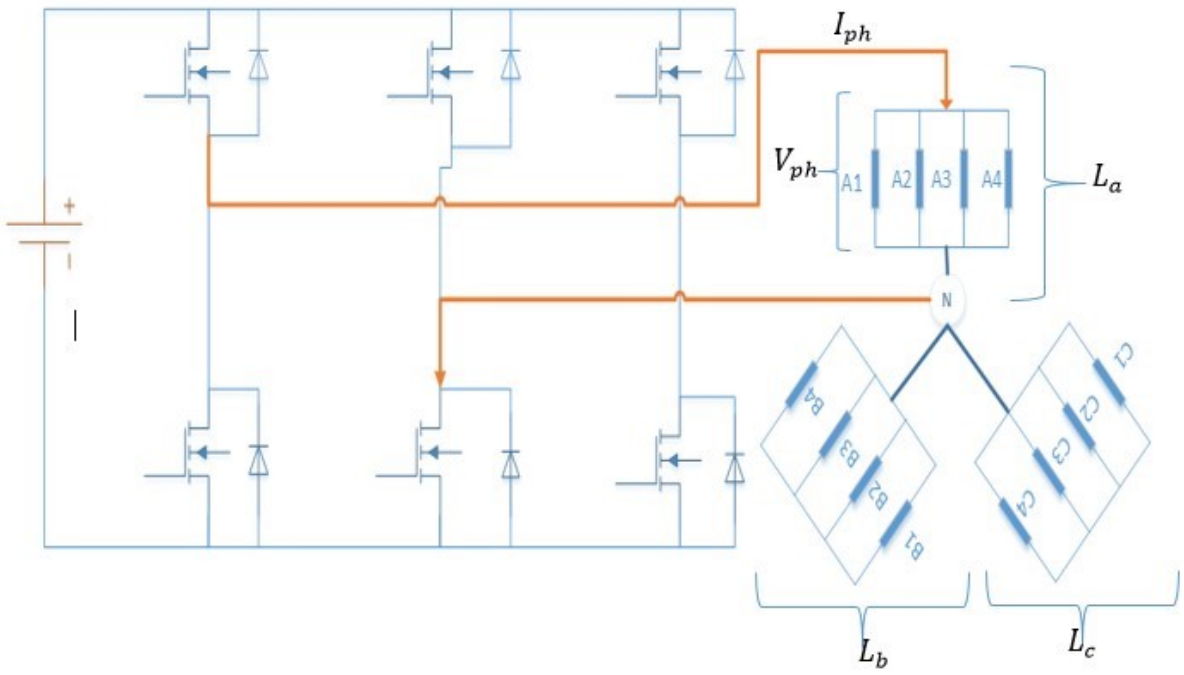

Figure 3.14: Phase self-inductance measurement setup

The measured phase self-inductance of phase A at various positions is shown in *Figure 3.15*. The FFT is performed to compute the componentsL_{s0}, L_{s2} and L_{s4}. The FE analysis is also performed to calculate the total phase self-inductance by calculating the total flux linkage per ampere at various rotor positions. *Table 3.2* shows the comparison of the self-inductance parameters computed from experimental data and FE analysis.

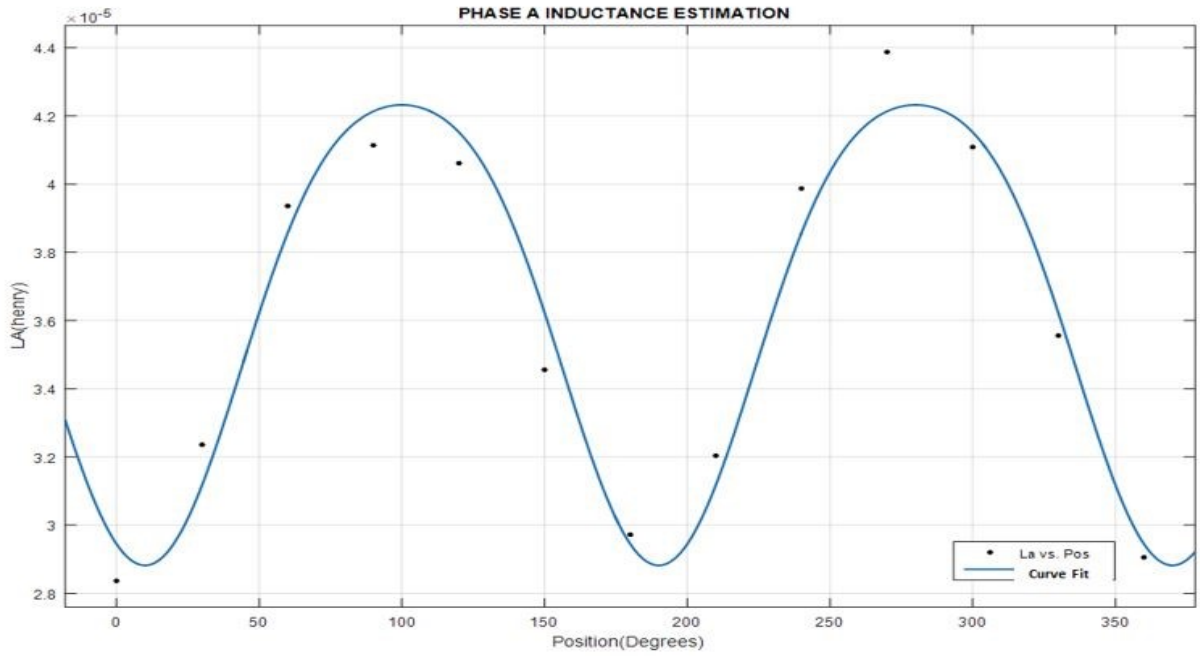

Figure 3.15: Total phase A self-inductance measured and the best curve fit cosine curve with dc, 2nd and 4th order harmonic

Term	FE(µH)	Measured(µH)
L_{s0}	36.23	36.6
L_{s2}	-5.64	-6.79
L_{s4}	0.5	0.78

Table 3.2: Comparison of FE Vs measured self-inductance parameters

3.3.2 Mutual inductance analysis

In this section, the mutual effect between the phases is modeled. *Figure 3.16* shows the mutual between A1 coil in phase A with the four coils in phase B. It can be seen that the coils of phase B are located in slot1, slot 4, slot7 and slot 10.

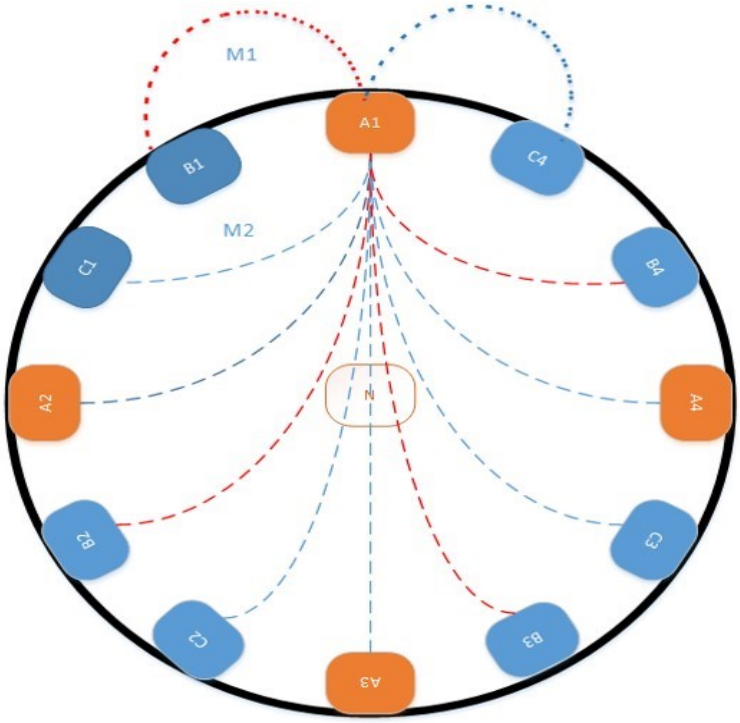

Figure 3.16: Mutual coupling between phase A coils and phase B coils is indicated by the red line

The total mutual inductance between phases can be shown as [13]:

$$M_{ab} = M_{S0} + M_{S2}\cos 2(\theta_e - 240) + M_{S4}\cos 4(\theta_e - 240) \quad (3.9)$$

$$M_{ac} = M_{S0} + M_{S2}\cos 2(\theta_e - 120) + M_{S4}\cos 4(\theta_e - 120)$$

$$M_{bc} = M_{S0} + M_{S2}\cos 2(\theta_e) + M_{S4}\cos 4(\theta_e)$$

where M_{S0} is the dc portion, M_{S2} and M_{S4} is the second and fourth order term. Assuming the magnitude of the mutual with coils 2 and higher slot apart are insignificant as concluded in section 3.2, these parameters can be defined in terms of the single coil mutual parameters (defined in Eq. (3.3)) as:

$$M_{S0} = (M_{01})/4 \quad (3.10)$$

$$M_{S2} = (M_{21})/4$$

$$M_{S4} = (M_{41})/4$$

To measure the mutual inductance between phases, current is passed through one of the phases and the voltage induced in the other phases is measured. Only one phase is linking with the flux while others are open. *Figure 3.17* shows the setup for measuring $M_{ab.}$ The mutual inductance between phase A and B can be calculated as:

$$M_{ab} = \frac{V_{bn}}{\frac{dI_a}{dt}} \tag{3.11}$$

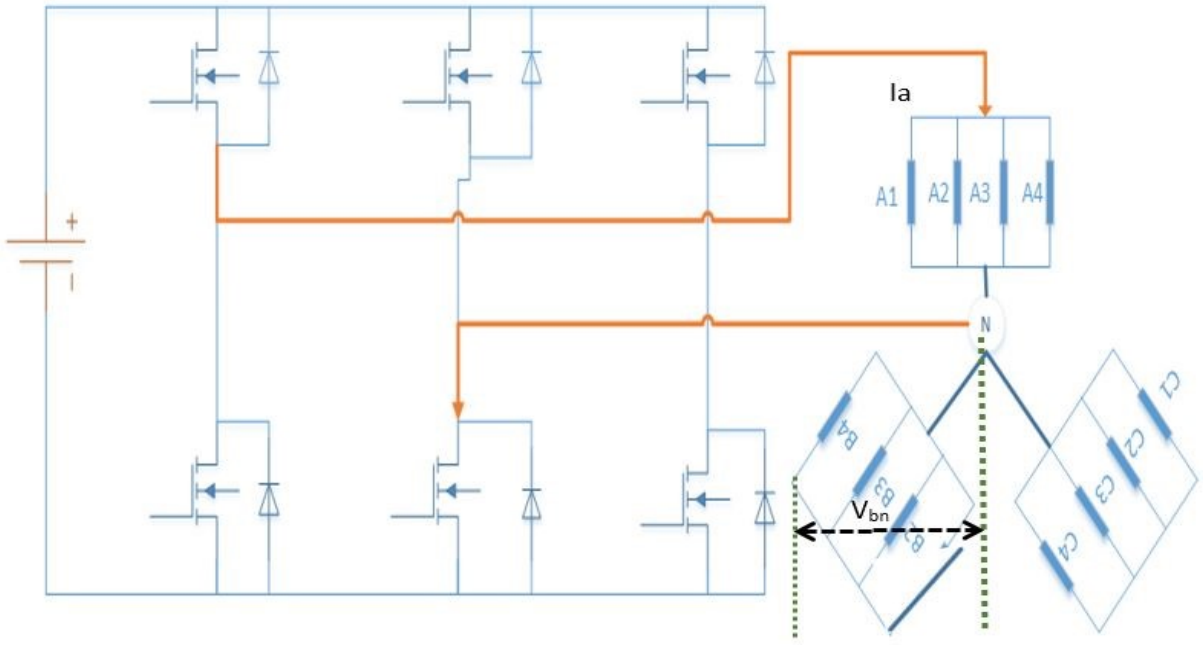

Figure 3.17: Measurement setup for measuring mutual inductance between Phase A and B

The mutual inductance measured is shown in *Figure 3.18*. The Fourier analysis of the result is done to obtain the mutual inductance parameters. The FE analysis is completed, and the comparison between the experimental and FE data for the mutual parameters is shown in *Table 3.3*.

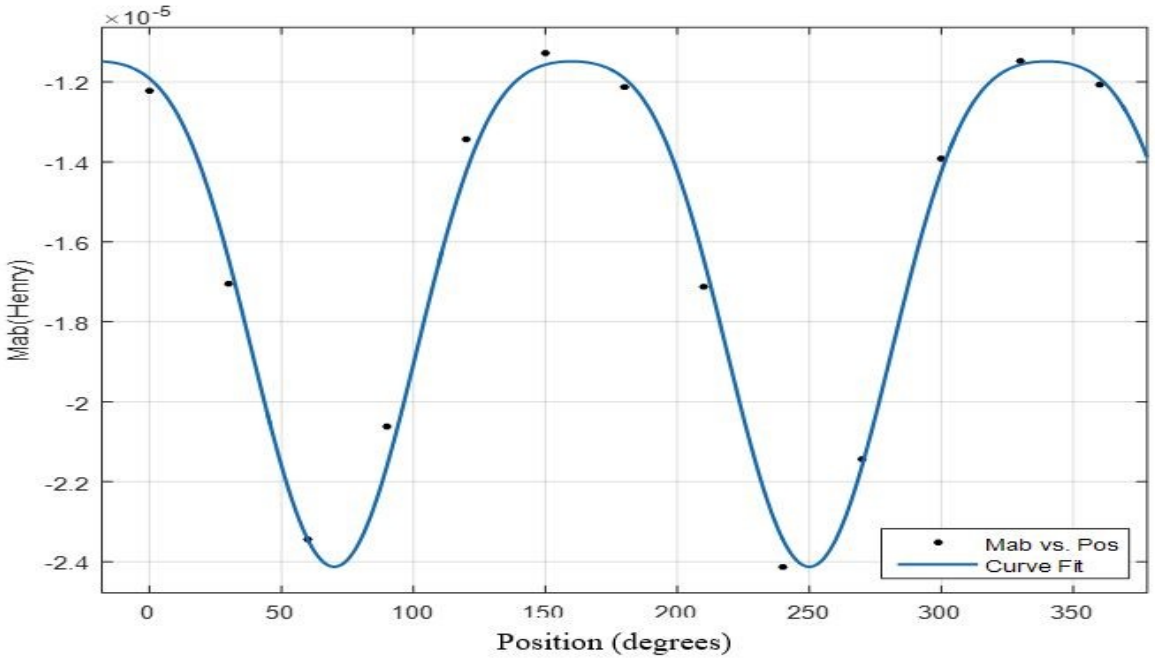

Figure 3.18: Practical measurement of Mab and the best curve fit cosine curve with dc, 2nd and 4th order harmonic

Term	**FE(µH)**	**Measured(µH)**
M_{S0}	-17.60	-16.54
M_{S2}	-5.64	-6.32
M_{S4}	-0.31	-0.51

Table 3.3: Comparison of FE Vs measured mutual inductance parameters

3.4 Conclusions

A detailed analysis of inductance variation for the IPMSM motor under study was completed. The expression for modelling the self and mutual inductance was verified with experimental and FE analysis. From these measurements the following conclusions are given:

1. The model of phase self-inductance can be expressed as :

$$L_a = L_{s0} + L_{s2}\, cos\, 2\theta_e \tag{3.12}$$

$$L_b = L_{s0} + L_{s2}\, cos\, 2(\theta_e - 120)$$

$$L_c = L_{s0} + L_{s2}\, cos\, 2(\theta_e - 240)$$

Where L_{s0} is the dc component and L_{s2} is the 2nd order component. The magnitude of the 4th order component L_{s4} is only 1-2% of the dc magnitude, therefore it is considered negligible and will be ignored in this research.

2. The magnitude of the mutual inductance of coils two slots apart is 10 times less than the magnitude of mutual inductance from coils one slot apart, therefore it is considered negligible and will be ignored in this research.

3. The model for the phase mutual inductance can be expressed as:

$$M_{ab} = M_{S0} + M_{S2}\, cos\, 2(\theta_e - 240) \tag{3.13}$$

$$M_{ac} = M_{S0} + M_{S2}\, cos\, 2(\theta_e - 120)$$

$$M_{bc} = M_{S0} + M_{S2}\, cos\, 2(\theta_e)$$

Where M_{S0} is the dc component and M_{s2} is the 2nd order component. The magnitude of the 4th order component M_{s4} is only 1-2% of the dc magnitude therefore it is considered negligible and will be ignored in this research.

4. The relationship between the phase self-inductance parameters L_{s0}, L_{s2} with the single coil parameters L_0 and L_2 was established. This was verified with experimental and FE analysis results.

5. The relationship between the phase mutual inductance parameters M_{s0}, M_{s2} with the parameters of mutual inductance of coils one slot apart M_{01} and M_{02} was established. This was verified with experimental and FE analysis results.

CHAPTER 4

Stator Inductance Estimation of Permanent Magnet Motors using PWM Excitation Method

4.1 Introduction

As shown in chapter 3 the rotor position information can be extracted by measuring the variation of inductance with respect to the rotor position. The inductance of the machine can be found in general by measuring voltage and the rate of change of current. In practical applications inductance is estimated by performing various tests offline, and finite element (FE) modelling. This approach won't account for production build variations and saturation changes. Accurate knowledge of the inductance is essential for optimum control of the machine. In this chapter, the main focus is estimating the machine inductance during operation of the machine.

In general, to control the motor for a position, speed or torque controlled system, a reference current calculation is performed and PI controllers are used to control the currents as shown in *Figure 2.3* in chapter 2. It is common in Permanent Magnet Synchronous Machine (PMSM) control to use the inductance in *d-q* coordinates. The torque developed in this case can be given as:

$$T_d = 1.5\big(K_e iq + iqid\big(L_q - L_d\big)P\big) \tag{4.1}$$

Where K_e is the back emf constant, $L_d$and L_q are the *d* and *q* axis inductances, *id* and *iq* are the *d* and *q*-axis currents and *P* is the number of pole pairs. To maximize the torque for a given peak current I_p the reference values for *iq* and *id* currents can be calculated as:

$$id = -\frac{3K_e}{8\,krc} + \frac{1}{2}\sqrt{\left(\frac{3K_e}{4krc}\right)^2 + 2I_p^2} \tag{4.2}$$

$$iq = \sqrt{I_p^2 - i_d^2} \tag{4.3}$$

where:

$$krc = \frac{3P}{2}(L_q - L_d)$$

Eq. (4.2) and (4.3) is easy to use as long as the available supply voltage can maintain the currents id and iq. But, as the speed increases *id* has to be increased and *iq* needs to be reduced to keep the applied voltage that can be maintained with the given supply voltage. The reference currents thus calculated has significant influence on the motor inductance parameters.

To understand the effect of erroneous inductance used in calculating the reference, the two inductance parameter namely L_d and L_q are adjusted such that L_q is reduced by 5% and L_d is increased by 5%. This will reduce the $L_q - L_d$ term as the $L_q > L_d$. From (2) it is clear that, for a given torque command, the *id* reference will be calculated lower and the *iq* reference will be higher. In order to understand the effect, the maximum torque corresponding to max current is commanded. Figure 4.1 shows the analytical result comparing the q axis current commanded versus the actual current in two scenarios:

1. Using nominal parameters.
2. When L_d inductance is increased by 5% and L_q inductance is lowered by 5% in the controller.

The expectation is that when the nominal parameter are used the commanded and measured current will follow each other and the torque thus developed is the maximum achievable torque at all speed

for the machine. Using the wrong parameter as explained above will create the reference current command to be higher in the case of *iq* and lower in the case of *id*. This is because the reduction in the $L_q - L_d$ term as explained before. The current will be able to follow the new reference command until the applied voltage hits the rail. After that, the measured current would deviate from the commanded current as the motor is not capable of generating the requested current estimated from the erroneous inductance value. This is shown in Figure 4.1

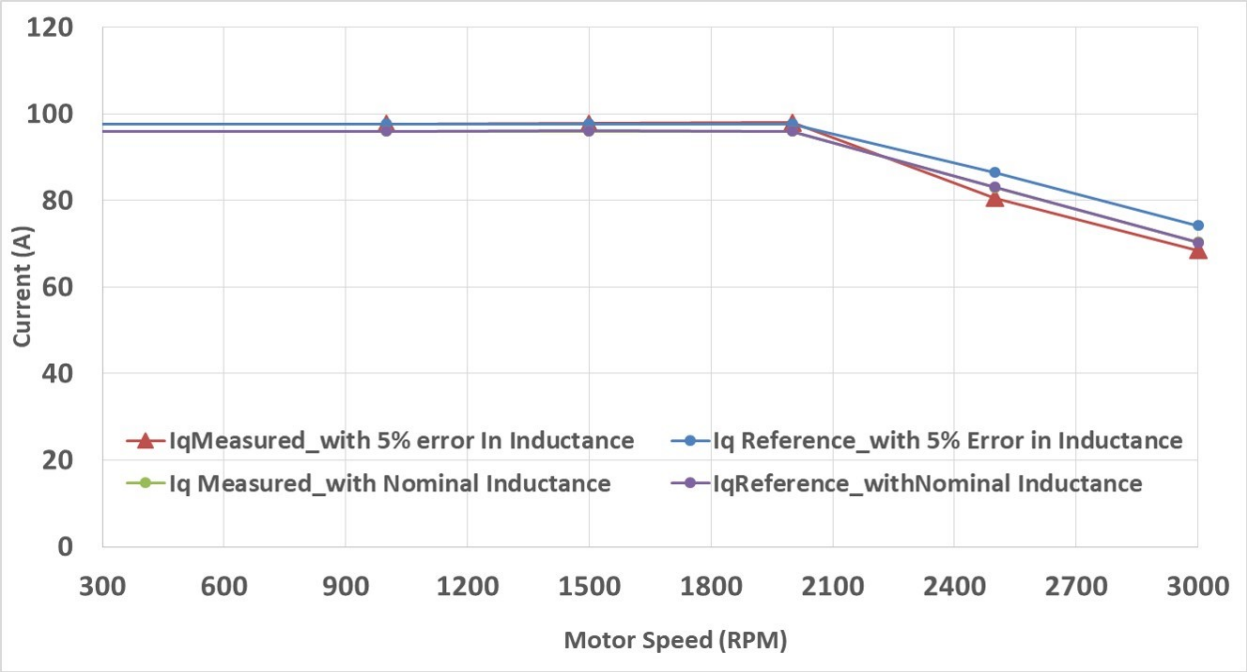

Figure 4.1: Effect of erroneous inductance value in the calculated reference current and the generated current

The effect of the increased *iq* and lower *id* due to the 5% error in inductance causes the torque generated at low speed to be smaller. The % error between the torque developed in the two scenarios is only 0.5% at low speed. At higher speed, once the voltage applied reaches the maximum voltage the % error in torque increases to more than 25% at certain speeds. This is shown in the Figure 4.2. From Figure 4.2 it is clear that the having an accurate knowledge of the inductance real-time is crucial for efficient control of the machine. This chapter thus addresses the online inductance estimation technique without any additional hardware or voltage injection.

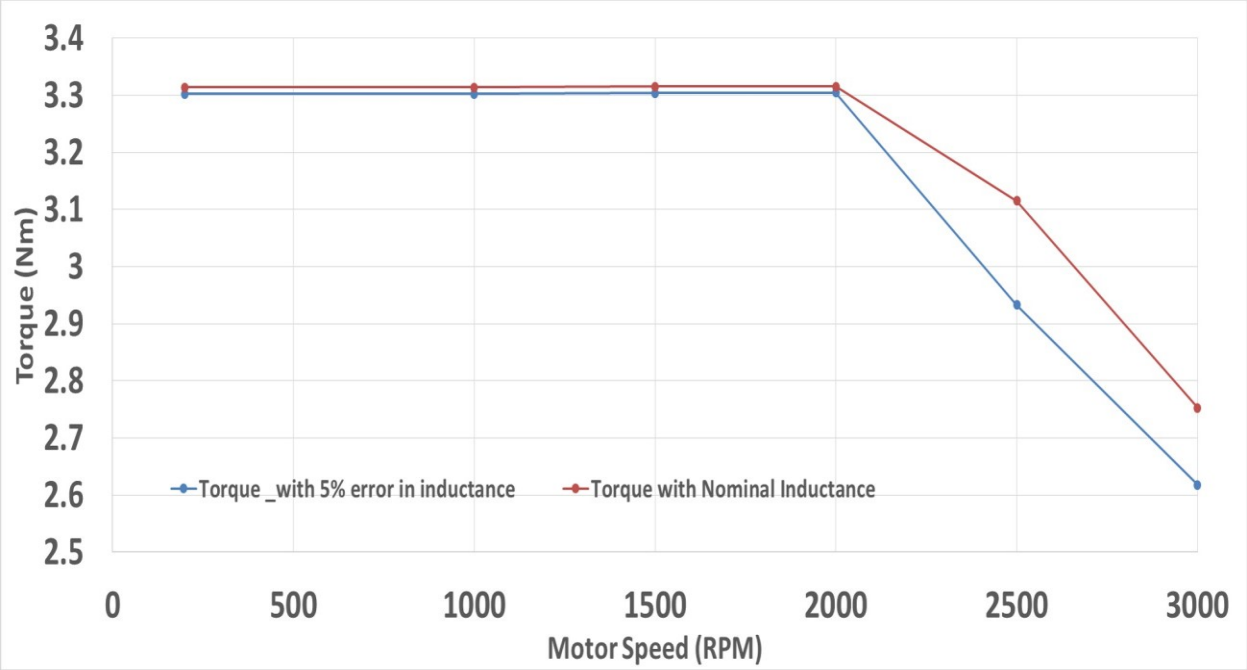

Figure 4.2: Effect of erroneous inductance in the reference current calculation on the torque generated

Various approaches have been presented to estimate the inductance which can be categorized as analytical method, finite element method and experimental method. The accuracy of the analytical method greatly depends on the accurate knowledge of the saturation factor and form factors. Neglecting saturation in PM modeling can lead to some errors in the inductance parameter. The finite element method can model the saturation effect fairly well but the estimated values are often needed to be practically validated and also variation in the build cannot be accounted. The experimental method usually needs highly complicated procedure and test setup. The accuracy issues of most widely used experimental methods are discussed in [46]. In order to overcome such issues online estimation are considered in [47]–[49]. However the estimation accuracy of these methods at very low speed is not discussed. Periodic external injections are used for estimating position and inductance in [50]–[52].The periodic injection causes vibration and acoustic noise issues which might not be suitable for some applications. The self-identification of machine parameters is discussed in [53]–[55]. The accuracy of the estimated parameters by such method is

good but such procedure might not be suitable for large volume production as it adds to manufacturing time.

The goal of this chapter is to propose a method to estimate the inductance of PM motor with rotor position at various load conditions including zero speed and torque conditions. It introduces measuring inductance using the excitation produced by the PWM signal utilized for the conventional motor drive control thereby introducing no external excitation, no additional hardware and no special procedure to obtain the inductance. This chapter is organized as follows Section 4.2 discusses the modelling of PWM excitation method defining the relationship between the observable parameters and the *dq* inductance used for the control. This section also covers various changes needed from the conventional PWM technique in order to maintain current excitation even at zero speed and zero average current. Section 4.3 derives a mathematical model of the equivalent inductance for each switching states. This section thus forms the relationship between equivalent phase inductance of each switching state with phase inductance parameters discussed in chapter 3. Section 4.4 talks about optimal current measurement regions based on the duty cycle applied in order to obtain optimum rate of change of current which is used for calculating the inductance. In section 4.5 online estimation of inductance is discussed. The section also discusses how to cancel the effect of resistive drop and back emf thereby allowing the estimation to work even at higher speed. Various experimental results of the proposed scheme are also shown.

4.2 Modelling PWM excitation method

The basic principle of modeling the PWM excitation method is to measure the rate of change of current. The rate of change of current is related to the inductance. The two major challenges in PWM excitation method are 1) Maintaining excitation at all load conditions so that the rate of change of current can be measured. 2) Measuring rate of change of current and detecting the inductance which is used for motor control. The dynamic equation of the machine can be modeled as:

$$\begin{vmatrix} v_a \\ v_b \\ v_c \end{vmatrix} = \begin{bmatrix} r_s & 0 & 0 \\ 0 & r_s & 0 \\ 0 & 0 & r_s \end{bmatrix} \begin{vmatrix} i_a \\ i_b \\ i_c \end{vmatrix} + p \begin{bmatrix} L_a & M_{ab} & M_{ac} \\ M_{ab} & L_b & M_{bc} \\ M_{ac} & M_{bc} & L_c \end{bmatrix} \begin{vmatrix} i_a \\ i_b \\ i_c \end{vmatrix} + \begin{bmatrix} e_a \\ e_b \\ e_c \end{bmatrix} \quad (4.4)$$

The inductance matrix shown in (4.4) has both self-inductance and mutual inductance parameters. The self and mutual inductance as explained in chapter3 section 3.31 can be expressesd as:

$$L_a = L_{s0} + L_{s2}\, cos\, 2\theta_e \quad (4.5)$$

$$L_b = L_{s0} + L_{s2}\, cos\, 2(\theta_e - 120)$$

$$L_c = L_{s0} + L_{s2}\, cos\, 2(\theta_e - 240)$$

$$M_{ab} = M_{S0} + M_{S2}\, cos\, 2(\theta_e - 240)$$

$$M_{ac} = M_{S0} + M_{S2}\, cos\, 2(\theta_e - 120)$$

$$M_{bc} = M_{S0} + M_{S2}\, cos\, 2(\theta_e)$$

It can be seen for both self and mutual inductance, it is assumed to have dc and 2nd order components. The terms L_{s0} and M_{S0} are the dc components of the self and mutual inductances,

while L_{s2} and M_{S2} are the magnitude of the 2nd order component of the self and mutual inductances respectively. Figure *4.3* redraws the reference axis definition which was defined in chapter 3 to help in the analysis for this chapter.

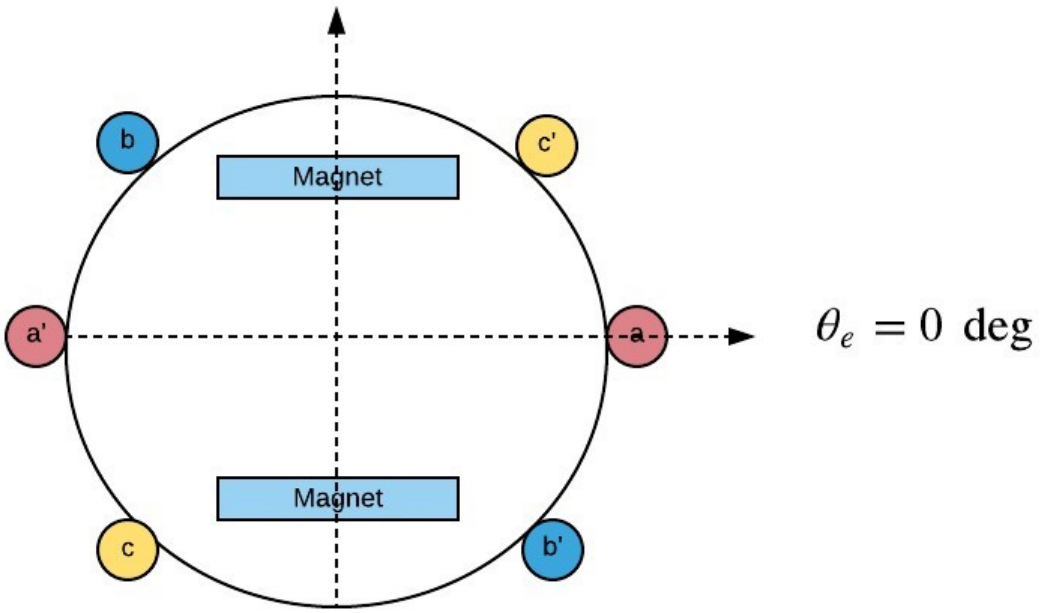

Figure 4.3: Motor reference axis definition used for the analysis

In practice, for motor control, the inductances in *dq* coordinates or *αβ* coordinates are usually used rather than the self and mutual inductance terms. The *αβ* transformed inductance can be defined in terms of self and mutual inductance parameter as:

$$L_\alpha = L_{\alpha 0} + L_{\alpha 2}\, cos\, 2\theta_e \tag{4.6}$$

$$L_\beta = L_{\alpha 0} - L_{\alpha 2}\, cos\, 2\theta_e$$

Where:

$$L_{\alpha 0} = L_{s0} - M_{S0}$$

$$L_{\alpha 2} = \frac{L_{s2}}{2} + M_{S2}$$

The $L_{\alpha 0}$ and $L_{\alpha 2}$ are defined as the DC and the magnitude of the 2nd order component of the inductances in $\alpha\beta$ coordinates [13]. Finally the relationship between the inductance in dq coordinates and the inductance in $\alpha\beta$ coordinates is shown as:

$$L_d = L_{\alpha 0} - L_{\alpha 2} \tag{4.7}$$

$$L_q = L_{\alpha 0} + L_{\alpha 2}$$

The objective of this paper is to estimate the L_d , L_q inductance values online by estimating $L_{\alpha 0}$ and the $L_{\alpha 2}$ from the PWM excitation. To obtain an inductacne at a standstill and zero torque, the conventional PWM excitation method will not be sufficient as the current through the phases will be zero when the voltage applied to the motor is zero. To measure rate of change of current under this condition, the phase voltage pulses are phase shifted with respect to each other so that the current excitation is available when the net average phase voltages are equal. *Figure 4.4* and *Figure 4.5* shows the difference between a conventional PWM and a phase shifted PWM. In the conventional PWM, when the duty cycles of all the three phases are equal, no current flows in the phase winding. Thus, inductance estimation cannot be performed. In the phase shifted PWM the current can be observed even when all the duty cycles are equal as the voltage excitation is available.

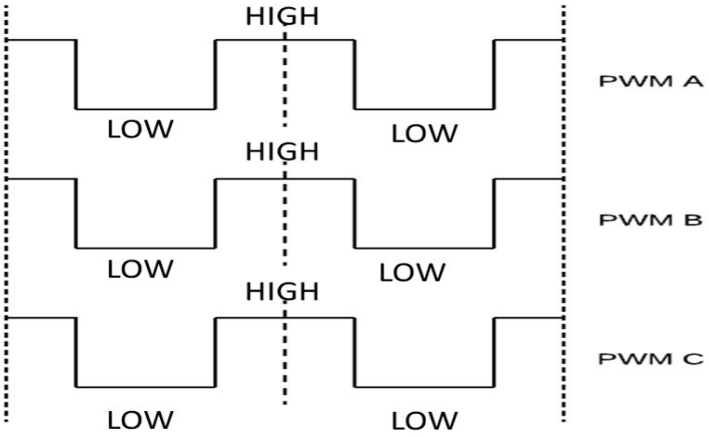

Figure 4.4: Conventional SVPWM sequence with zero applied voltage across the motor phases

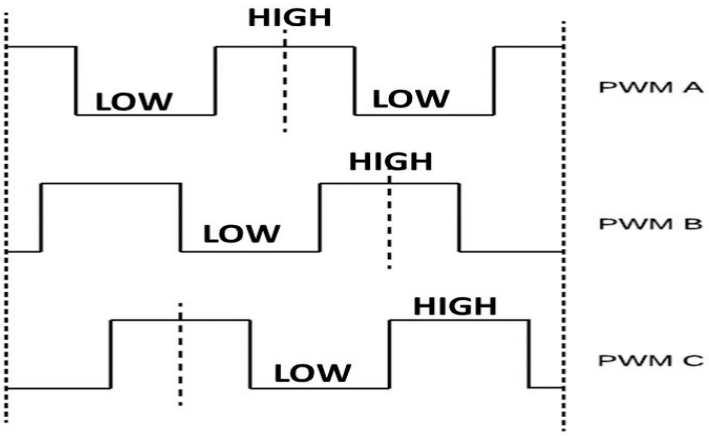

Figure 4.5: Phase shifted SVPWM sequence with zero applied voltage across the motor phases

To further understand this, Figure 4.6 shows different switching states in a conventional PWM. The switching states for phases A, B and C are defined such a way that if the motor phase is connected to the power source (Battery) positive, it is defined as “1, ” and if the motor phase is connected to the negative of the battery, it is defined as “0.” The PWM states such as U0 and U7 it can be seen that the excitation voltage is zero and therefore di/dt will be zero, assuming zero speed and torque. This scenario is shown in Figure 4.4. In this research the switching state U1- U6

will be defined as “active swticiing states” and U0 and U7 will be defined as “inactive switcihing states”

In order to overcome the issue of maintaining the current excitation during inactive switching states modification has to be done to the existing PWM. One of the possible solutions is phase shifting the PWM of one or two related phases for more than $\mathbf{t_{min}}$ with di/dt measurements proceeding at that appropriate instant. The modified PWM sequence is shown in Figure 4.5.

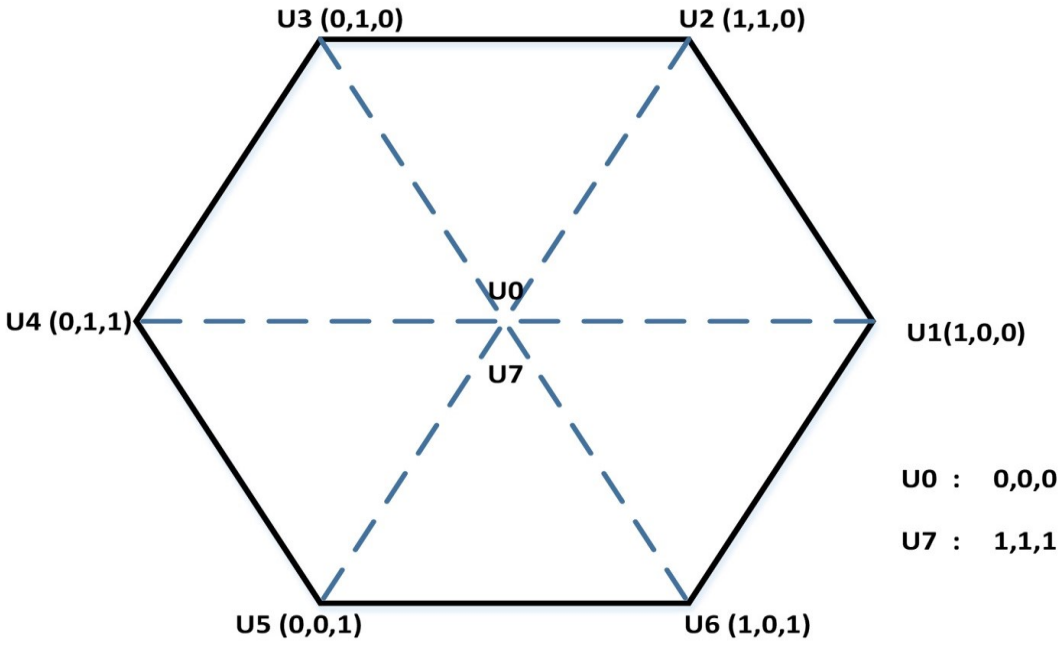

Figure 4.6: Conventional SVPWM switching states

Figure 4.7 shows the calculated phase currents for all the three phases when a continuous 50% duty ratio is applied to the three phases obtained with the motor speed set to zero. In such scenario the average voltage is zero. It can be seen that unlike the conventional PWM, the phase shifted PWM provides excitation with average current being zero. Thus, the rate of change of current can now be calculated even when the output voltage is zero.

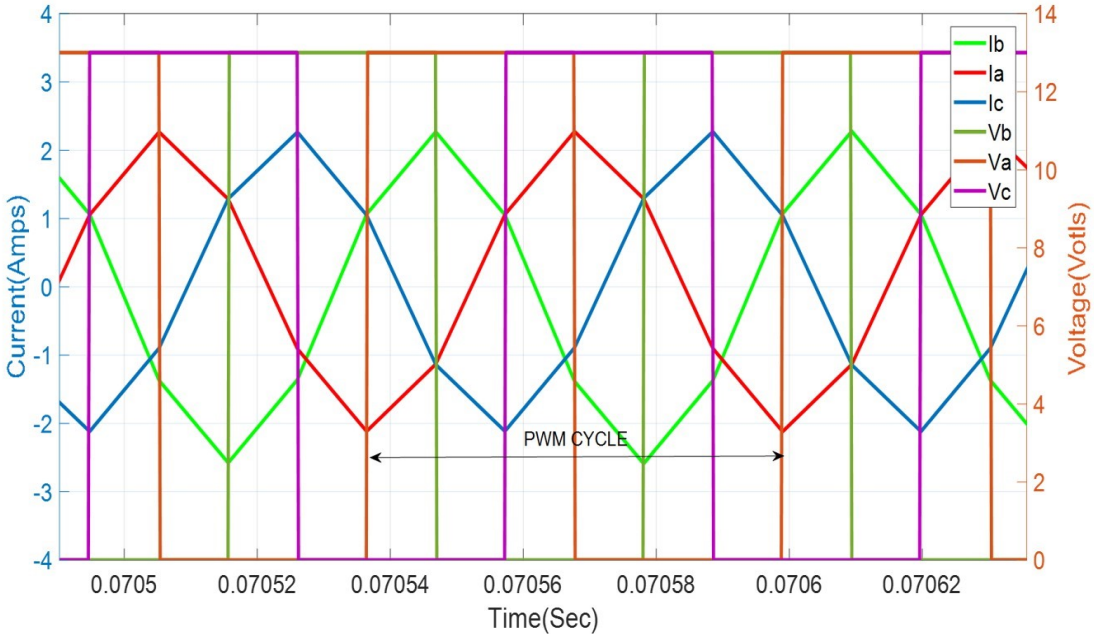

Figure 4.7: Phase current at 50% duty cycle for each of the three phases with phase shifted SVPWM at standstill

4.3 Equivalent inductance of a three phase system based on switching states

In this section, the effective inductance is modeled using the self and mutual inductance parameters defined in chapter 3. It can be seen from *Figure 4.7* that, in one PWM cycle there are 6 six different slope regions in each phase current corresponding to the six different active switching states. In general depending on the duty cycle of each of the phases, there can be another state where all the low side switches are ON or all the high side switches are ON. The equivalent inductance for each of these states can be calculated by knowing the applied voltage and the rate of change of current corresponding to each of these states. In order to estimate phase inductance online it is critical that we find a relationship between the equivalent inductance and the phase inductance parameters described in Eq.(4.5)

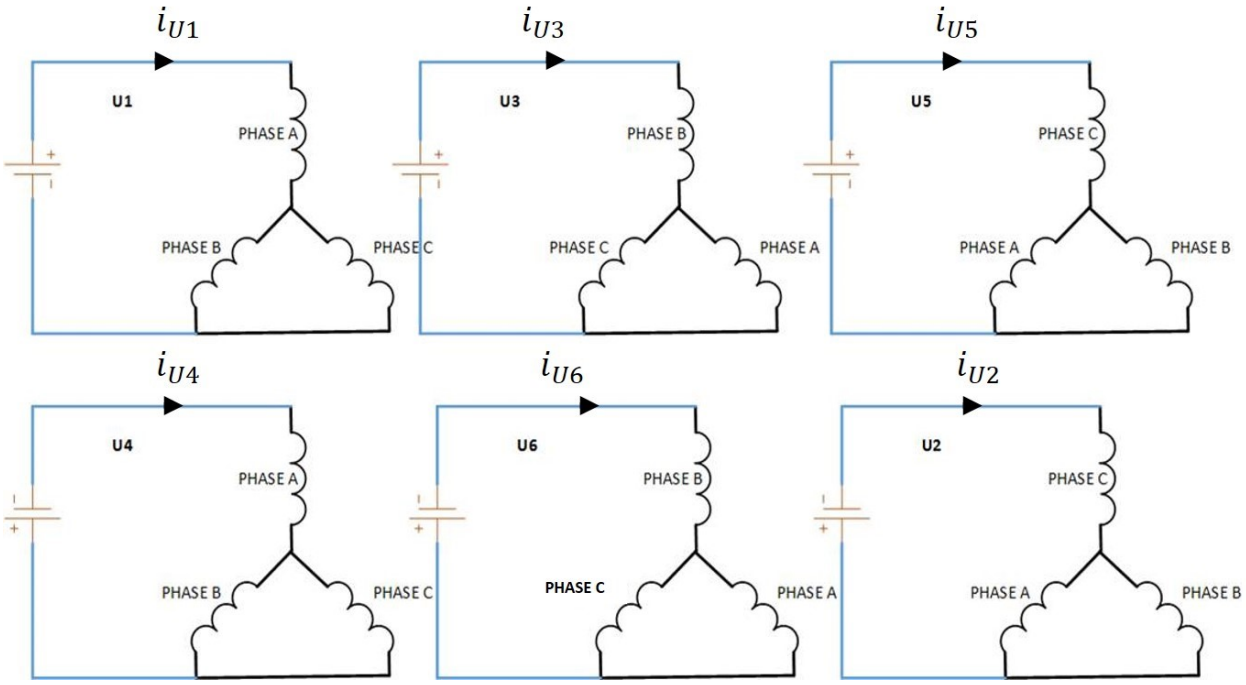

Figure 4.8: Motor winding connection during different switching states

To find a relationship between the equivalent inductance and the phase inductance consider the three switching states U1, U3, and U5. From *Figure 4.8* it can be seen that these states are such

that one of the phases are connected to positive rail while other two phases are connected to the negative rail. The phase resistance are not considered to study the equivalent inductance.

Case 1: Phase A is high, Phase B & Phase C Low (**U1 Switching state**)

Assuming static condition the phase to neutral voltage can be expressed as:

$$v_{an}=\frac{d(\left(L_a* i_a+(M_{ab}-M_{ac})* i_b-M_{ac}*i_a\right))}{dt} \tag{4.8}$$

$$v_{bn}=\frac{d((L_b-M_{bc})* i_b+(M_{ab}-M_{bc})* i_a)}{dt}$$

$$v_{cn}=\frac{d((M_{ac}-L_c)\, i_a+(M_{bc}-L_c)* i_b)}{dt}$$

Where:

v_{an}, v_{bn}, and v_{cn} : phase to neutral voltages.

Since $v_{bn} = v_{cn}$ for U1 switching state, i_b can be written as:

$$i_b=\frac{(M_{ab}-M_{bc}-M_{ac}+L_c)}{(2M_{bc}-L_c-L_b)}i_a \tag{4.9}$$

Substituting the expression for i_b from (4.6) in v_{an} and v_{cn} and finding v_{ab}

$$v_{ab}=\frac{d\,(i_a*\left[\frac{{M_{ab}}^2+{M_{bc}}^2+{M_{ac}}^2-2M_{ab}\,M_{bc}\,-2M_{bc}\,M_{ac}-2M_{ab}\,M_{ac}+2\,L_a\,M_{bc}+2L_b\,M_{ac}}{+2L_c\,M_{ab}-L_aL_b-L_b\,L_c-L_c\,L_a}{(2M_{bc}-L_c-L_b)}\right])}{dt}$$

v_{ab} for U1 switching state can be expressed in general as:

$$v_{ab}=\frac{d(i_aL_{1eq})}{dt} \tag{4.10}$$

Where:

$$L_{1eq} = \frac{M_{ab}{}^2+M_{bc}{}^2+M_{ac}{}^2-2M_{ab}\,M_{bc}-2M_{bc}\,M_{ac}-2M_{ab}\,M_{ac}+2\,L_a\,M_{bc}+2L_b\,M_{ac}+2L_c\,M_{ab}-L_aL_b-L_b\,L_c-L_c\,L_a}{(2M_{bc}-L_c-L_b)} \quad (4.11)$$

Substituting the expression for L_a, L_b, L_c and M_{ab}, M_{ac}, M_{bc} from (4.5) in the above equation and also using the expression for $L_{\alpha 0}$ and $L_{\alpha 2}$ given in (4.6) . The U1 state equivalent inductance L_{1eq} can thus be expressed as:

$$L_{1eq} = \frac{3(L_{\alpha 0}^2-L_{\alpha 2}^2)}{2(L_{\alpha 0}-L_{\alpha 2}\cos(2\theta_e)} \quad (4.12)$$

Case 2: Phase B is high, Phase A & Phase C Low (**U3 Switching state**)

Following similar analysis as done for Case 1

$$L_{3eq} = \frac{3(L_{\alpha 0}^2-L_{\alpha 2}^2)}{2(L_{\alpha 0}-L_{\alpha 2}\cos(2(\theta_e-120))} \quad (4.13)$$

Case 3: Phase C is high, Phase A & Phase B Low (**U5 Switching state**)

$$L_{5eq} = \frac{3(L_{\alpha 0}^2-L_{\alpha 2}^2)}{2(L_{\alpha 0}-L_{\alpha 2}\cos(2(\theta_e-240))} \quad (4.14)$$

It is to be noted that the equivalent inductance of other switching state can be defined using the above three equivalent inductance. The relationship of the remaining switching states can be shown as:

$$L_{4eq} = L_{1eq} \tag{4.15}$$

$$L_{2eq} = L_{5eq}$$

$$L_{6eq} = L_{3eq}$$

4.4 Online current slope measurement

From the last section the relationship between equivalent inductances of all switching states and the inductance parameters $L_{\alpha 0}$ and $L_{\alpha 2}$ is established. The next important step is to establish the

relationship between the measured current slope and the equivalent inductance. The relationship between the current slope, the applied voltage V and the equivalent inductance can be shown as:

$$\frac{di_a}{dt} = \frac{V}{L_{1eq}}$$

$$\frac{di_b}{dt} = \frac{V}{L_{3eq}} \tag{4.16}$$

$$\frac{di_c}{dt} = \frac{V}{L_{5eq}}$$

It is to be noted that the current slope is measured at the appropriate switching state in order to calculate the corresponding equivalent inductance. For example, the $\frac{di_a}{dt}$ is measured for computing L_{1eq} only in the switching state U1. From (4.16) it is clear that the measured current slope is proportional to the inverse of the equivalent inductance. Substituting the expression derived for equivalent inductance from (4.12) in (4.16), the current slope can be expressed in general by a dc and 2nd order component for each of the three switching state U1, U3 and U5 as:

$$\frac{di_{U1}}{dt} = S_{U1} = S_{off} + S_{amp2} * \cos(2 * \theta_e) \tag{4.17}$$

$$\frac{di_{U3}}{dt} = S_{U3} = S_{off} + S_{amp2} * \cos(2 * (\theta_e - 120)) \tag{4.18}$$

$$\frac{di_{U5}}{dt} = S_{U5} = S_{off} + S_{amp2} * \cos(2 * (\theta_e - 240)) \tag{4.19}$$

Where:

$$S_{off} = \frac{2VL_{\alpha 0}}{3(L_{\alpha 0}^2 - L_{\alpha 2}^2)} \tag{4.20}$$

$$S_{amp2} = \frac{2VL_{\alpha 2}}{3(L_{\alpha 0}^2 - L_{\alpha 2}^2)}$$

The relationship of current slope from switching states U2, U4, and U6 compared with switching states U1, U3, and U5 can be expressed as:

$$\frac{di_{U2}}{dt} = S_{U2} = -\frac{di_{U5}}{dt} \tag{4.21}$$

$$\frac{di_{U4}}{dt} = S_{U4} = -\frac{di_{U1}}{dt}$$

$$\frac{di_{U6}}{dt} = S_{U6} = -\frac{di_{U3}}{dt}$$

From Eq.(4.17) –(4.19) it can be deduced that, by measuring the current slope and estimating the S_{off} and S_{amp2} ,the DC component and the magnitude of 2nd order component respectively, from any one of the switching state, the inductance parameters $L_{\alpha 0}$ and $L_{\alpha 2}$ can be calculated as:

$$L_{\alpha 0} = \frac{-2 * S_{off} * V}{3({S_{amp2}}^2 - {S_{off}}^2)} \tag{4.22}$$

$$L_{\alpha 2} = \pm \sqrt{{L_{\alpha 0}}^2 - \frac{2 * VL_{\alpha 0}}{3 * S_{off}}}$$

From (4.19) it is clear that by measuring the rate of change of phase current corresponding to any one of the state, we can obtain the inductance parameters by observing the magnitude of dc and the second order magnitude of the current slope signal. Let's consider the scenario where the Phase A voltage is high and Phase B and Phase C are low, this defines the U1 switching state. The phase voltages are measured with respect to the ground. During the U1 state the Phase A current measurement is done. Similarly the Phase B and Phase C current are measured during the U3 and U5 switching state. In each PWM cycle, rate of change of phase current is calculated at least for one of the switching state. It is important to note that the amount of time the switching state is present has to be more than a minimum time t_{min} in order to avoid erroneous calculation of the slope. The amount of time for each switching state is present is determined by the applied duty cycle. In the event when the sampled phase current data for the switching state is less than the minimum time t_{min}, the rate of change of current cannot be calculated. In such cases, measurements will have to be made either in switching state U3 or in U5 where the minimum available time is not violated. *Figure 4.9* shows the data of Phase current A from U1 switching state. It is seen that the data near the switching time needs to be avoided as these are influenced by the nonlinearities in the switches and the winding capacitances. The rate of change of current shall be computed in the linear region of the current. The minimum time t_{min} shall be defined such that there is a good measurement of the rate of change of current avoiding all the nonlinearities of the switches. In this research the t_{min} is set at 8µs

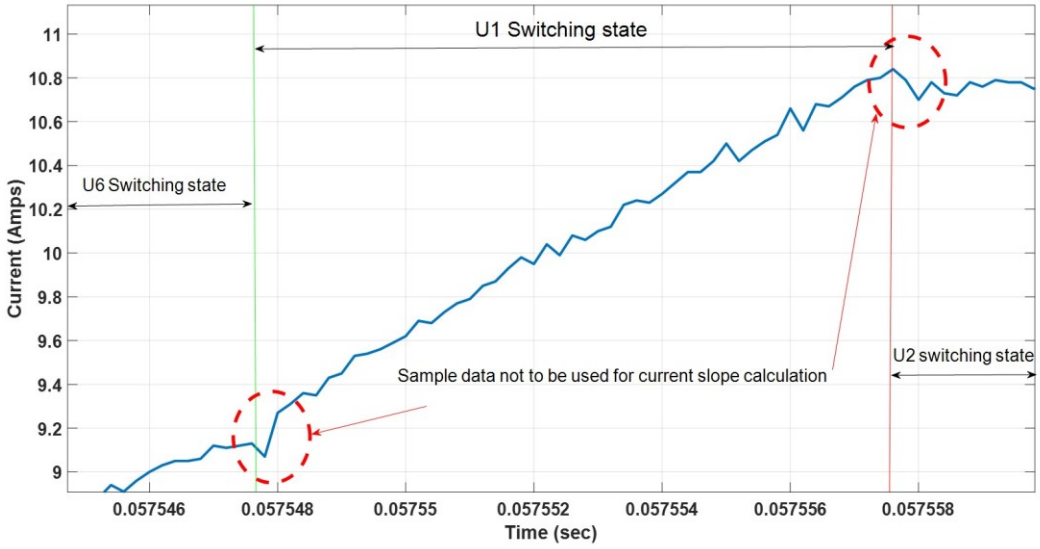

Figure 4.9: Measured phase current A using oscilloscope indicating U1 switching state

4.5 Estimation of inductance

To estimate phase inductance we need to observe the dc (S_{off}) and the 2nd order harmonic magnitude, S_{amp2} of the current slope measured. An Extended Kalman Observer is constructed to extract the DC and magnitude of the 2nd order harmonics of the signal. The detailed explanation of the Kalman Observer is given in Chapter 6. The S_{off} and S_{amp2} are estimated using the adaptive. The L_d and L_q are calculated using equations (4.22) and (4.7). *Figure 4.10* shows the block diagram of the online inductance estimation.

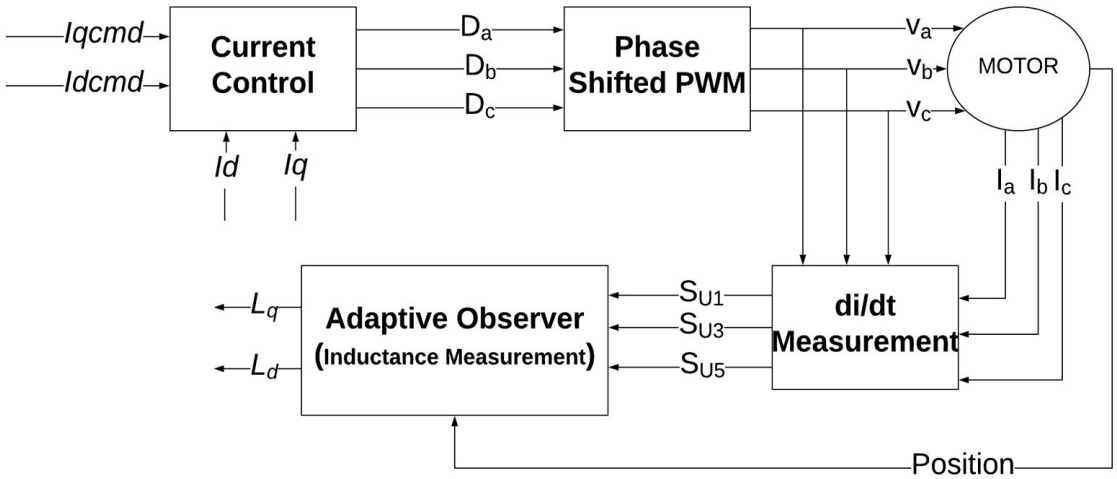

Figure 4.10: Block diagram for the inductance estimation

As stated in the previous section in order to estimate inductance the phase voltage and phase current are measured under various load condition. The Appendix B shows the parameters of the motor used for the study.

4.5.1 Inductance estimation at zero speed

From (4.17) it can be observed that, to obtain the S_{off} and S_{amp_2} we need the measurement data for one complete electrical cycle. Thus an observer based approach will not be able to converge at zero speed. For zero speed, the equivalent inductance from the three different switching states are required, for example, the U1, U3, U5 switching states. As noted in equations (4.13) to (4.15), the two unknowns $L_{\alpha 0}$ and $L_{\alpha 2}$ can be derived from the three equivalent inductance measured if rotor position is not known. In the case where rotor position is known the any two out of the three equation in (4.15) can be used. The equivalent phase inductance measured for the U1 PWM state is compared with the model result in *Figure 4.11*. The model result are obtained by using the self and mutual inductance parameters (L_{s0} , L_{s2}, M_{s0}, M_{s2}) and calculating the equivalent inductance from the expression derived in (4.13).The experimental and the analytical results match with each other, thereby validating the model obtained. *Figure 4.12* shows the equivalent phase inductances

for the U1, U3, and U5 states as the rotor is rotated by 360 electrical degrees. Figure 4.12 shows both the measured inductances and a curved fit function for all the three states.

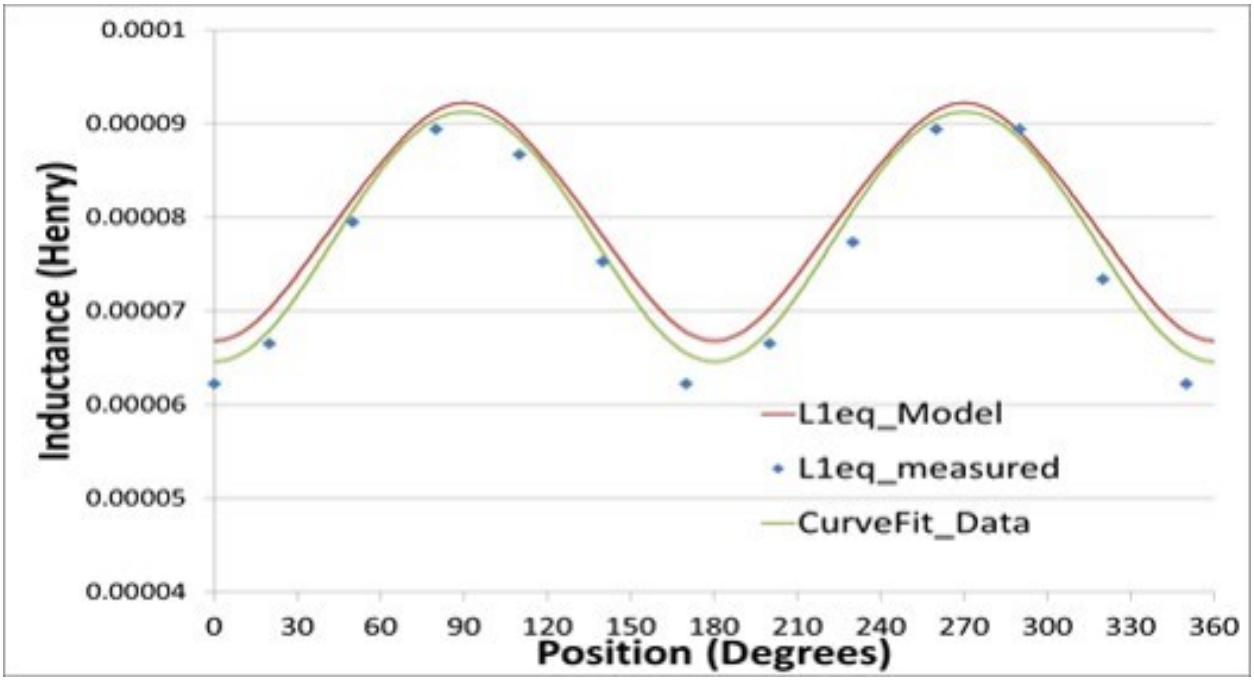

Figure 4.11: Equivalent phase inductance for U1 State (L_{1eq}) Model, Measured and best fit cosine curve

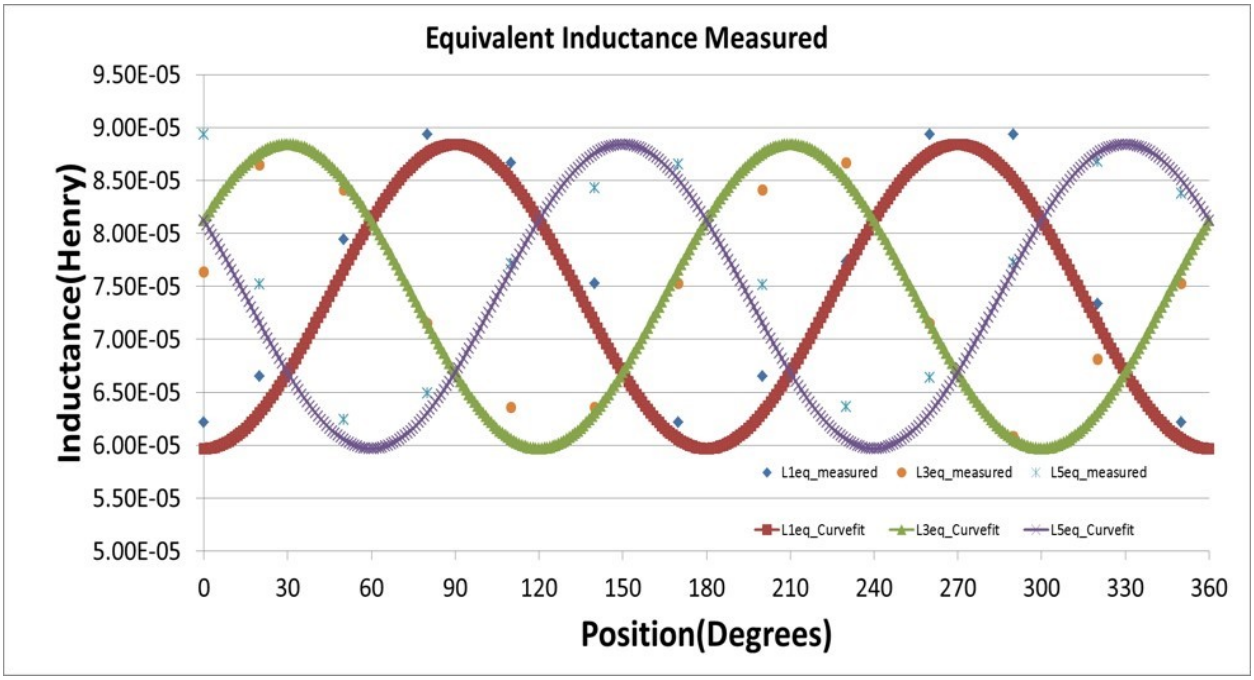

Figure 4.12: The measured equivalent inductance $L_{1eq}, L_{3eq}, L_{5eq}$ from the test machine along with the best fit cosine curves under static conditions

4.5.2 Inductance estimation at low/mid speed at various load condition

The phase voltage and phase current are measured under various load conditions. The *Figure 4.13* shows the phase currents and the rate of change of current measured for U1 switching region for q-axis current command (iq_{cmd}) of 10 Amps. The adaptive observer will be used to estimate the S_{off} and S_{amp2}. Only the rate of change of current from one phase is needed for the calculation of the inductance. The phase inductances in *dq* coordinates can thus be calculated from the observed values S_{off} and S_{amp2}, using the expressions given in (4.22) and (4.7). The *Figure 4.14* shows the comparison of the model versus measured current slope for U1 switching region in one electrical cycle.

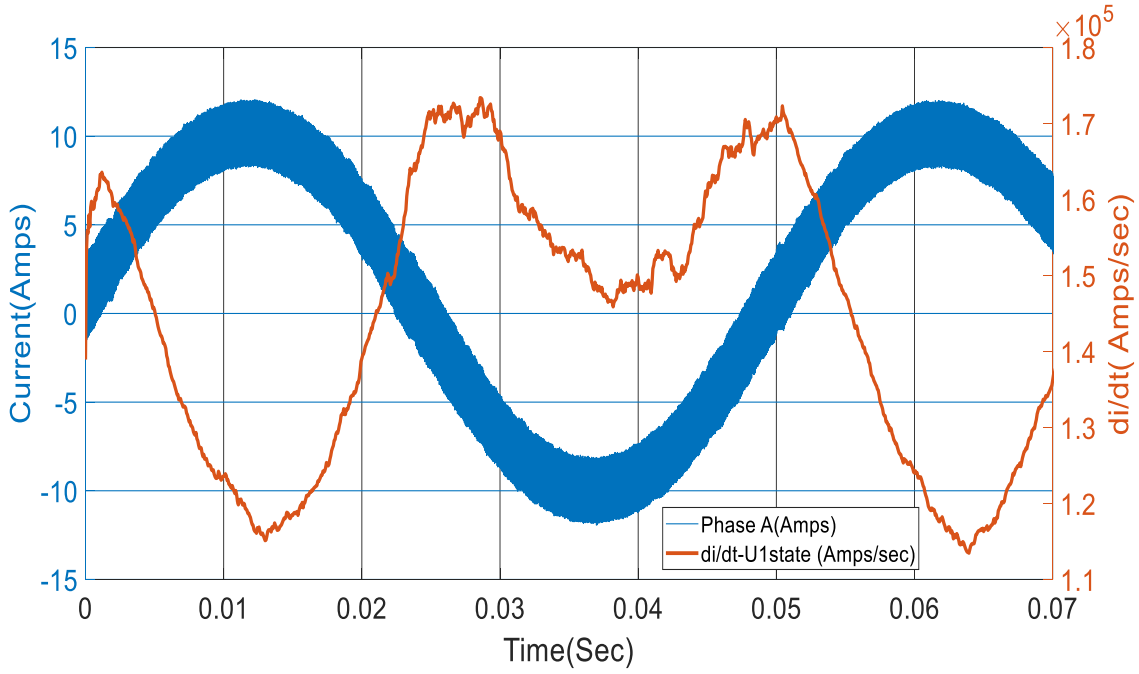

Figure 4.13: Measured phase-A current and di/dt for U1 switching region for *iqcmd* =10Amps

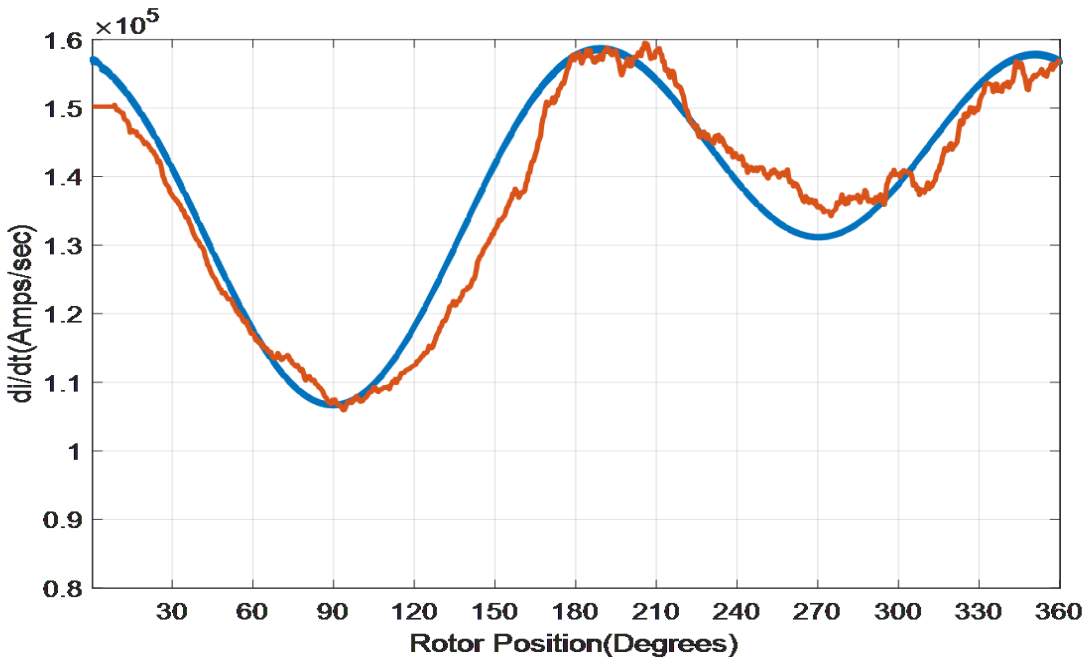

Figure 4.14: Comparison of di/dt, model vs practical for U1 switching region at 300RPM for *iqcmd* =10Amps

It can be seen from *Figure 4.14* that the main harmonics in the measured rate of change of current are first and second order harmonics. The DC bias and the magnitude of the second order harmonics are observed for estimating the inductance parameters. The reason for the first order magnitude seen in the measured current slope is due to the IR drop in the machine. This IR drop increases with the increasing current. The equivalent inductance model obtained in the last section for each active switching state did not considering the effect of resistance drop and back emf. To avoid the influence of the resistive drop and back emf voltage, derivative of current is obtained from one active switching state such as U1 and one form the inactive switching state such as U0.

The voltage equation for the U1 and U0 switching state can be given as:

For the U1 state:

$$V_{dc} = i_1 r_{eq} + L_{1eq}\frac{di_1}{dt} + e_1 \tag{4.23}$$

For the U0 state:

$$0 = i_0 r_{eq} + L_{1eq}\frac{di_0}{dt} + e_0$$

Where:

$i_1,\ i_0$: Current in phase A during U1 and U0 switching states

e_1, e_0: Back EMF during U1 and U0 switching states

L_{1eq}: Equivalent Inductance during U1 and U0 switching states

r_{eq} : Equivalent resistance in all switching states

Since the U0 and U1 state are switching states close to each other the following assumption can be made in regard to the resistive and back emf drop:

$$e_0 \approx e_1 \tag{4.24}$$

$$i_1 r_{eq} \approx i_0 r_{eq}$$

Thus, by measuring the di/dt from both switching states close to each other and subtracting them to cancel the effect of resistive drop and back emf, the saliency information can be tracked.

$$V_{dc} = L_{1eq}\left(\frac{di_1}{dt} - \frac{di_0}{dt}\right) \tag{4.25}$$

The resultant current slope is only a dc and second order component as shown in *Figure 4.15* which also includes a curve fit value for comparison. Thus it can be seen that the effect of resistive drop and the back emf voltage can be eliminated by making two current derivative measurement one from an active switching state (U1-U6) and one from inactive switching state (U0 or U7). This methodology thus helps us to calculate the inductance even at high speed. In the event when the sampled phase current data for the switching state U0 is less than the minimum time t_{min}, it is possible to subtract the sampled current data from the switching state U4. By doing so the resistive drop and back emf can be still eliminated.

Figure 4.15: Measured current slope for U1 switching state after subtraction from U0 state for *iqcmd* =10Amps at 300RPM

Figure 4.16 shows the rate of change of current for U1 state at a higher load condition with an *iqcmd* of 50 amps after the subtraction from the U0 state. Figure 4.17 shows the inductance value calculated as function of different load condition compared with Finite Element (FE) results.

One of the disadvantages of this method is that at zero torque and speed, there still will be some high frequency phase current though the fundamental component is zero. Another factor that has to be considered is the ability of the processor to measure and calculate the slope in each of the PWM cycle. Today's processors are capable of doing such measurement and calculation. This is discussed in detail in the Chapter 5

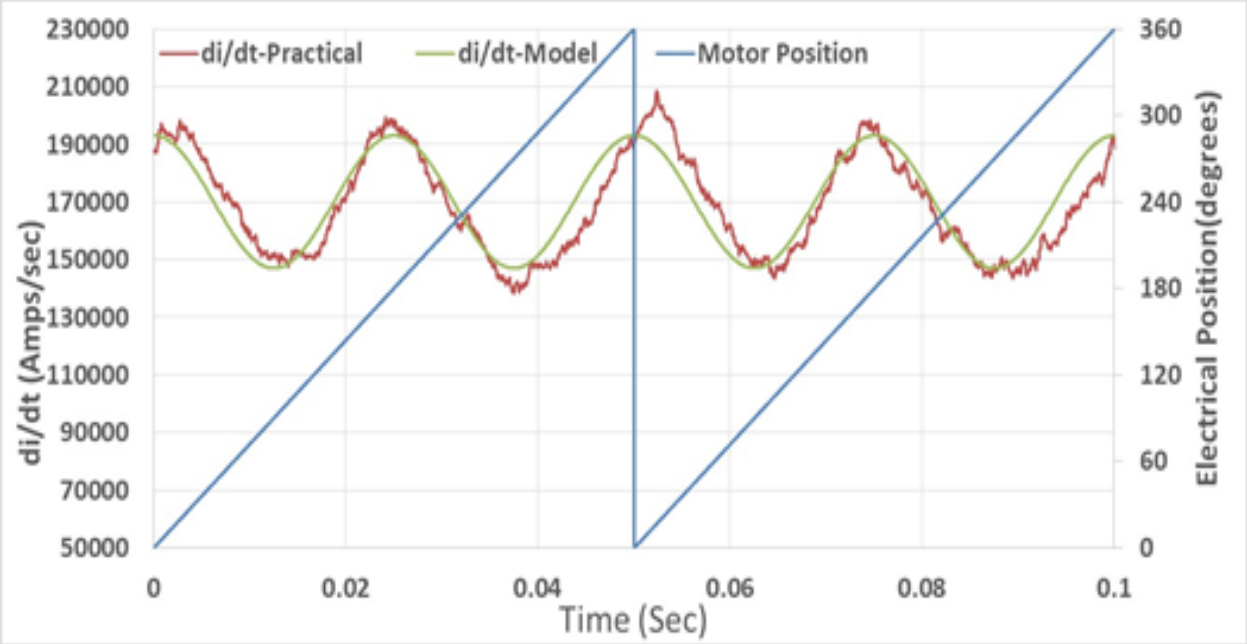

Figure 4.16: Measured current slope for U1 switching state after subtraction from U0 state for *iqcmd* =50amps

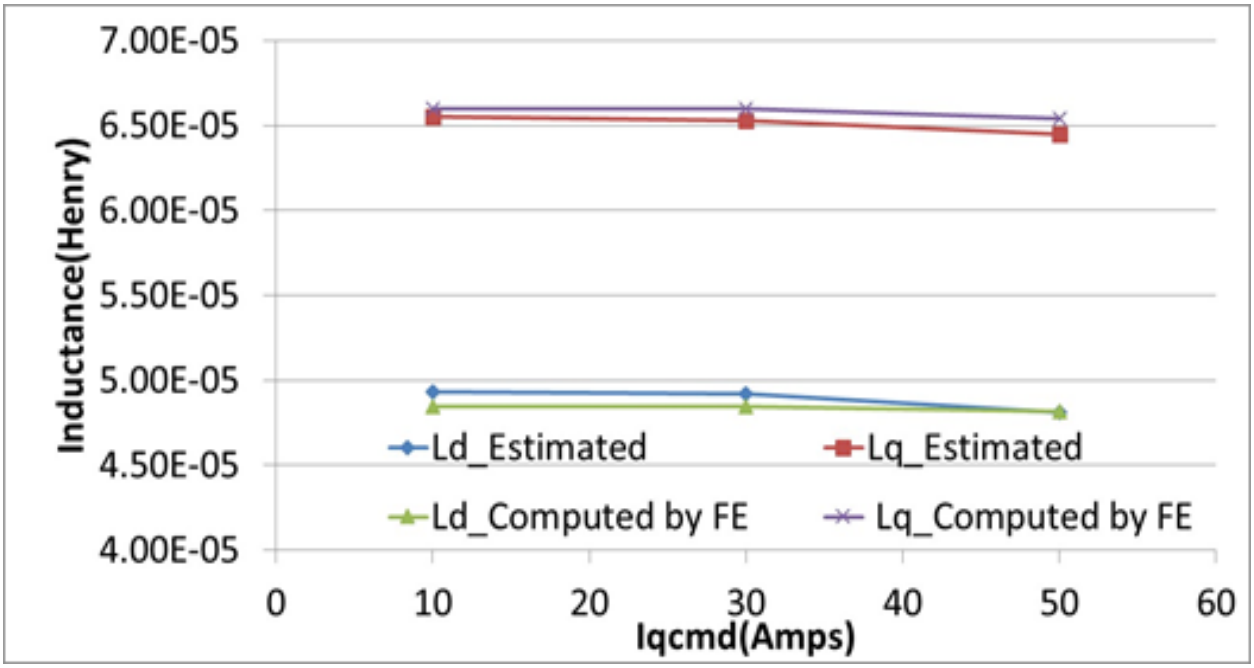

Figure 4.17: Comparison of online estimated d and q axis inductance at various load condition with FE analysis results

4.6 Conclusions

This chapter presented a novel way of estimating online phase inductance for IPMSM machine without using any external injection techniques but to use the normal PWM based excitation used for the motor drive control. The following are the main contributions of this chapter:

1. A methodology to provide current excitation at all operating ranges especially at average zero voltage condition
2. A mathematical model showing the equivalent phase inductance in terms of phase inductance parameters
3. Deriving the expression of Current derivative and the methodology to cancel the effect of back emf and resistive drop

Online inductance measurement proposed in this chapter can be used to improve the motor control performance. The proposed method also is useful for motor position estimation without using any external injection including at zero speed. This technique, therefore, provides certain advantages over the conventional injection based techniques used for position estimation such as the vibration, and acoustic noises issues can be eliminated. This will be discussed in Chapter 6

CHAPTER 5

Practical Implementation for Current Derivative Measurement for Sensorless Control of Permanent Magnet Machine

5.1 Introduction

Measuring the current derivative is an essential step in extracting the saliency information using PWM excitation. This can be achieved in two ways, one using di/dt sensors and another using fast current sensor sampling. The former increases the total system and packaging cost. In the latter, in order to obtain accurate current slope, current has to be sampled at a high sampling rate around 1MHz. Very little information is available in the literature on how to obtain an accurate di/dt measurement without additional hardware. In [56], [57] DSPACE and FPGA are used to do fast data accusation and uses only two sampled current points spaced apart by a given time t to obtain the current slope. In order to obtain a robust current slope the two points sampled are spaced apart by time $t>t_{min.}$. The two-point measurement can cause the slope measured to be erroneous due to noise in the current sampled. In order to overcome this some oversampling techniques are proposed in [58], [59]. The key concept is to sample more than one point and reconstruct the signal and then take the derivative, thereby reducing the noise in the calculated di/dt measurement. In [60], [61] fast sampling in FPGA is implemented and then DSPACE is used to calculate the derivative every PWM cycle. The FPGA and DSPACE are not used for practical mass produced applications such as steering, braking and aerospace. Implementation of such oversampling techniques is not possible as it directly impacts the total software throughput. This chapter proposes a novel method where accurate current slope can be measured without burdening the processor and obtaining robust current slope at various duty cycle.

This chapter is organized as follows: Section 5.2 discusses about possible switching states needed in order to estimate current slope without the effect of resistance drop and back EMF. Section 5.3

talks about the how to do oversampling in ADC to obtain current measurement without affecting the total software throughput. In section 5.4 various methodology of obtaining optimum current derivative is analyzed .Various experimental results are also presented in this section. Section 5.5 address the practical issues with today's hardware for shunt based current measurement.

5.2 Switching states needed for current derivative measurement

In order for estimating the saliency information, the current derivative has to be obtained at various switching state. The idea in this reasearch is to sample current at high rate such that the current derivative for the appropriate swtiching state can be calculated.The various switching states for an

SVPWM technique was described in Chapter 3. To understand the possible switching states needed for the current derivative measurement let's consider the following:

As explained in Chapter 4 Section 4.5 , in order to eliminate the resistive drop and back emf voltage from the measured current slope we need to sample current from one of the active switching states (U1-U6) and one from the inactive switching states (U0,U7) . For example for U1 switching state it can be shows that

For U1 State:

$$V_{dc} = i_1 r_{eq} + L_{1eq} \frac{di_1}{dt} + e_1 \tag{5.1}$$

For U0 State:

$$0 = i_0 r_{eq} + L_{1eq} \frac{di_0}{dt} + e_0 \tag{5.2}$$

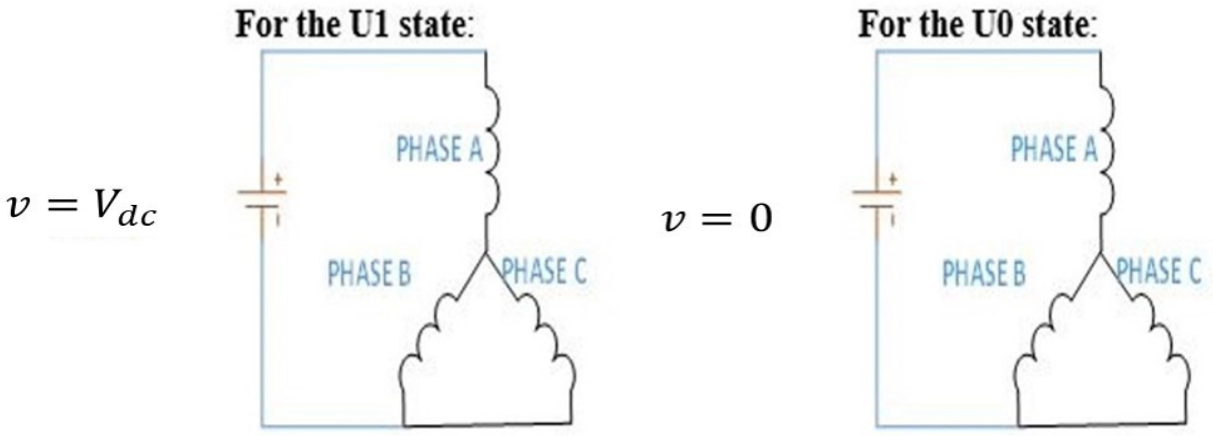

Figure 5.1: Switching states U1 and U0

Subtracting (5.3) from (5.2) it can be seen that:

$$\frac{di_1}{dt} - \frac{di_0}{dt} = \frac{V_{dc}}{L_{1eq}} - \frac{i_1 r_{eq} - i_0 r_{eq} + e_1 - e_0}{L_{1eq}} \tag{5.4}$$

As explained in chapter 4 since the U0 and U1 state are switching states close to each other the back emf and the resistive drop from both the switching state can be considered the same and therefore second term in Eq. (5.4) is zero. Thus:

$$V_{dc} = L_{1eq}\left(\frac{di_1}{dt} - \frac{di_0}{dt}\right) \tag{5.5}$$

The Figure 5.2 shows the one of the possible switching states at which current sampling is done. Thus, it can be seen that we need to sample current from one active switching state (U1-U6) and one inactive switching state (U0 or U7) for proper measuring of current slope. It is to be noted that the switching state shown in Figure 5.2 might not be present at all operating conditions. The states which are present for current measurement is a function of the Modulation index applied and the position. This will be discussed in detail in Chapter 6

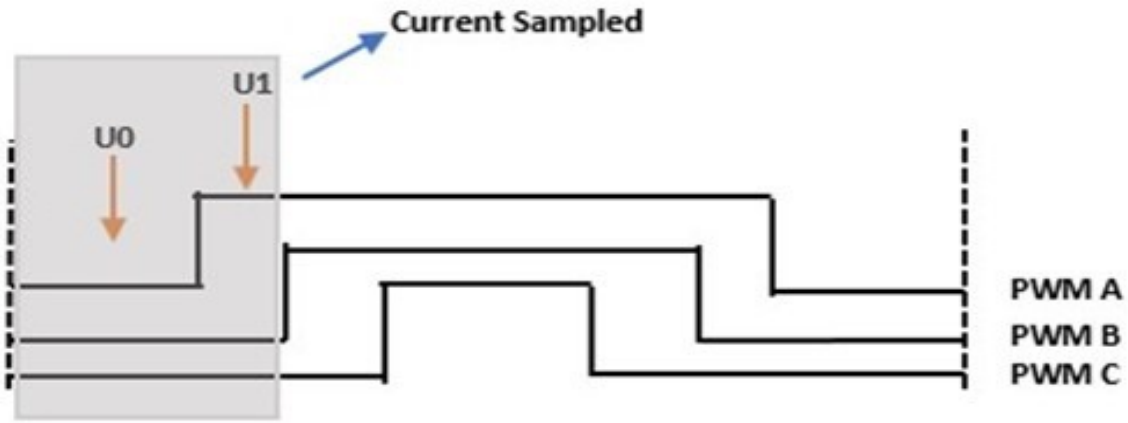

Figure 5.2: Switching states showing where current is sampled

5.3 Current measurement using oversampling technique

As explained in section 5.2, in order to obtain current slope without using any external sensor, oversampling methodology is the optimum way to implement. One of the main disadvantages in the oversampling method is that, the processor throughput is greatly affected. In this section an optimum method to measure the current slope is presented.

The main idea is to sample ADC as fast as possible without affecting the processor throughput. The slope can then be calculated averaging few points and dividing by the time. For example as shown in, if there are n phase A current samples obtained in switching state U1, the current slope can be calculated as:

$$\frac{di_1}{dt} = \frac{\sum_{k=\frac{n}{2}+1}^{n} i_{a_k} - \sum_{k=1}^{n/2} i_{a_k}}{\frac{n}{2} * t_s} \tag{5.6}$$

The t_s in (5.6) is the sampling time of the current sensor and i_a represent Phase current A. The proposed architecture of averaging the current before calculating the slope reduces the effect of the noise seen in the sampled current. Thus, this methodology is more robust when compared to the architecture provided in literatures [10]-[11] of taking 2 points in the current sampled and dividing by difference in time between samples to obtain the current slope.

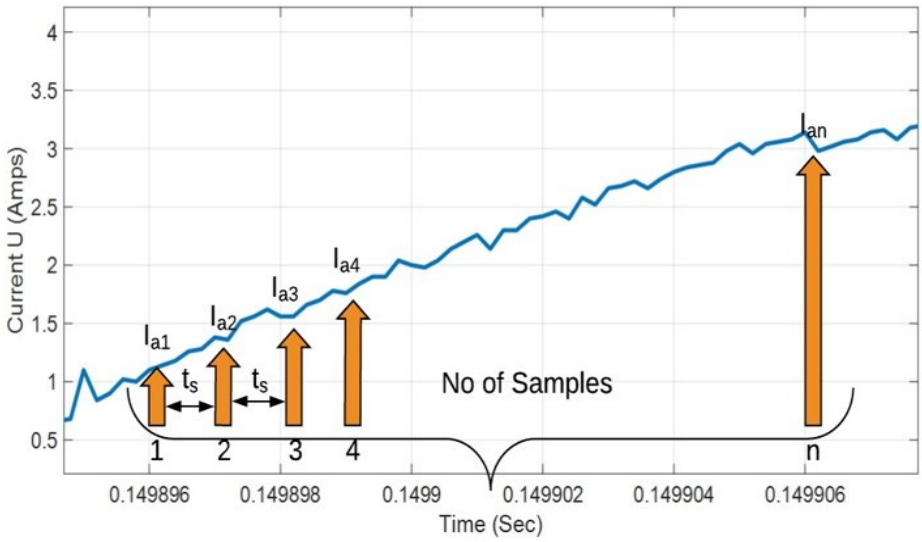

Figure 5.3: Current samples obtained by fast current sampling using DMA architecture

The key concept for doing fast sampling without affecting the throughput is to have an architecture where the ADC sampling can be triggered by a timer block and use the processor Direct Memory Access (DMA) engine to move the results from the ADC result register to a software buffer after every ADC sampling is completed. A DMA engine is now very common in most processors used in the automotive and aeronautic industry.

5.3.1 DMA background

The DMA engine in the microcomputer is used to transfer data between two locations in memory map in the background of CPU operations. Typically, the DMA is used to:

1. Transfer blocks of data between external and internal data memories.

2. Restructure the portions of internal data memory

In general, the DMA controller transfers data from a data source location to data destination locations without intervention of the CPU or other on chip devices. A DMA move is an operation that always consist of two parts as shown in Figure 5.4.

1. A read move that loads data from a data source into DMA controller.

2. A write move that puts the data from the DMA controller to a data destination.

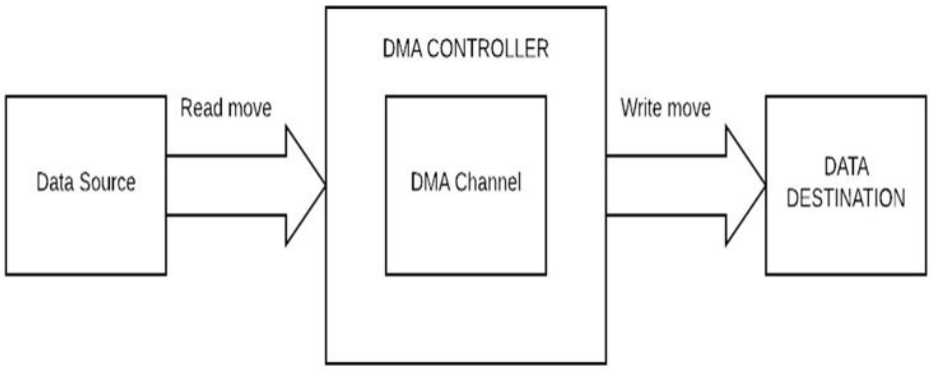

Figure 5.4: DMA move definition

One of the key feature of DMA is that a DMA move can be initiated by other subunits in the microcomputer such as ADC using the interrupt router. The DMA source and destination address can be preprogrammed and therefore no software intervention is required for the move.

5.3.2 Proposed architecture

The idea here is to use the DMA to continually serve an ADC peripheral. A timer in the processor is set up to trigger ADC sampling every 1us. The trigger then kicks of an ADC sampling periodically. Most of the ADC can generate usually two triggers based on two events:

1. Source event trigger
2. Result event trigger.

Source event trigger interrupt is kicked off whenever an ADC is requested to sample a channel. Result event is triggered once the ADC places the sampled data in the ADC results register. In the proposed architecture the ADC result event trigger is used to trigger the DMA move. The DMA can be preprogrammed with the source address location and the destination buffer location. Figure 5.5 shows different blocks involved for the fast current sampling for optimal current slope calculation. Each block in Figure 5.5 is numbered to show activation of these different blocks with respect to a PWM cycle as shown in Figure 5.6

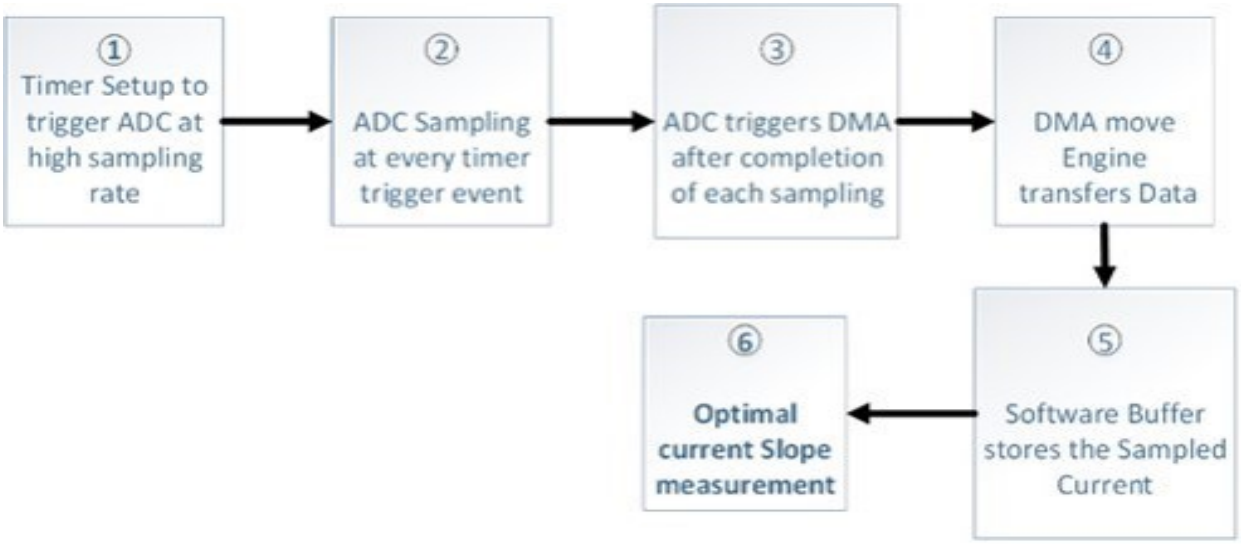

Figure 5.5: Steps involved in calculating the current slope using the oversampling technique using DMA based approach.

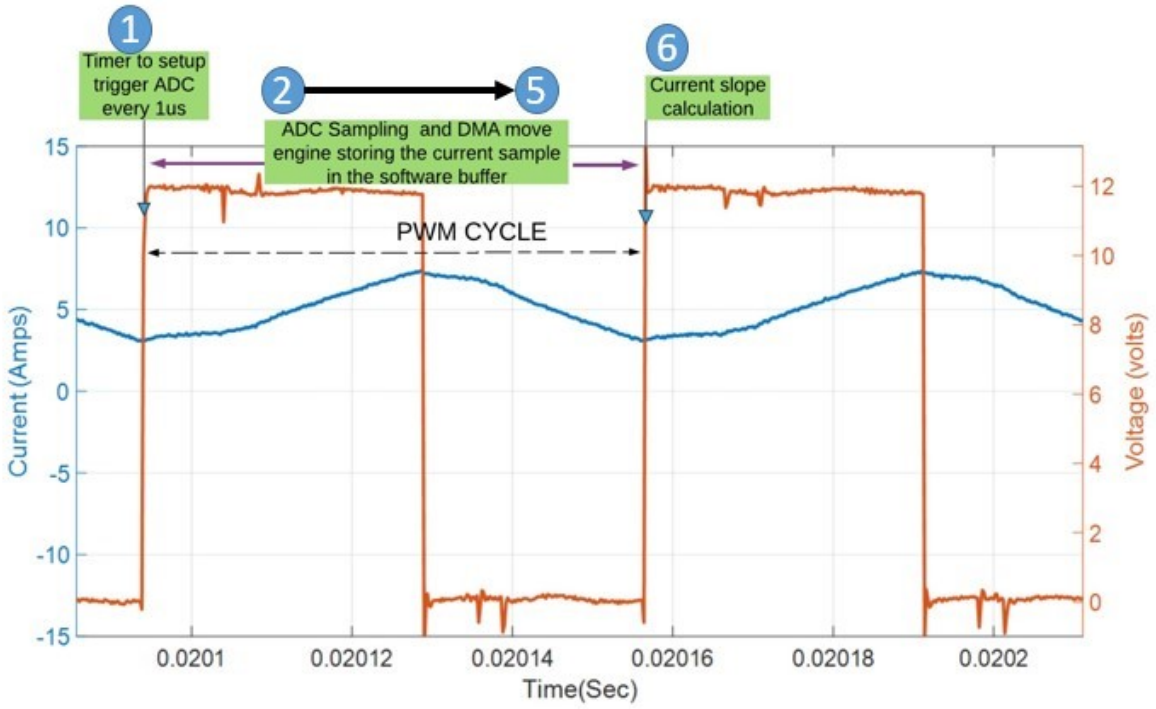

Figure 5.6: Proposed current sampling with respect to PWM cycle

It is to be noted that the current sampled by the ADC is moved to the software buffer after every sampling. After each DMA move the destination address is incremented automatically so that the next sample is stored in the next index of the buffer as shown in Figure 5.7. Therefore all the

sampled current are available at the start of the PWM for the current slope measurement. At the start of each PWM cycle the data from the buffer is used to calculate the slope, in order to avoid DMA writing into the same buffer (while the slope calculation is being completed), the destination address of the DMA is switched to another buffer at the start of each PWM cycle as shown in Figure 5.7. The Ping-Pong of buffer at each PWM cycle helps for continuous current sample.

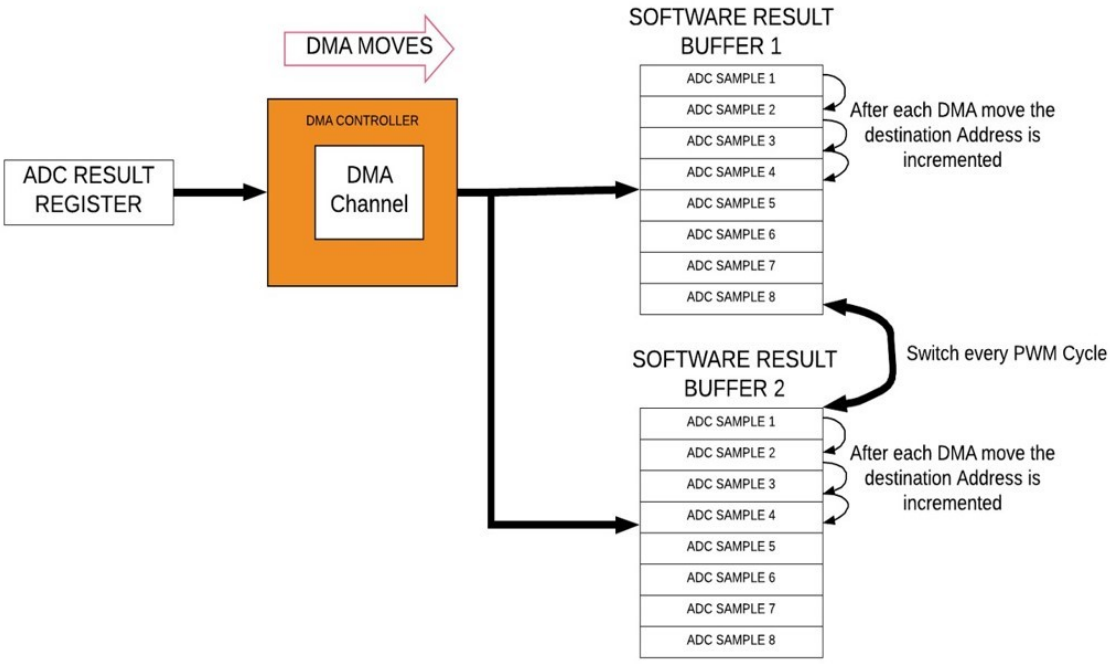

Figure 5.7: Ping-Pong of buffer in the proposed architecture

The Figure 5.7 only shows the sampling of one phase current but in reality all the three phase currents can be measured using the same architecture with each sampled data being moved to separate software buffers using three different DMA channels. It is to be noted that DMA is programmed to automatically move to the next memory location in the destination buffer after

every move. On every motor control period start the values from the buffer is used to calculate the slope of the current.

One of the key advantage of the architecture proposed is that the fast ADC sampling is done without burdening the processor overhead. Another key aspect is maximum amount of data samples are obtained for all the switching states. This is critical in the PWM excitation method since the maximum amount of data that can be sampled solely dependent on the duty cycle. In the event when the sampled phase current data in U1 switching state is less than the minimum time t_{min}, the rate of change of current cannot be calculated from the U1 state. In such cases, measurements will have to be made either in switching state U3 or in the switching state U5 where the minimum available time is not violated. This architecture thus allows to choose the optimal current sample needed in order to obtain robust current slope. The complete flow chart of the DMA setup and code for the register configuration is given in Appendix C. The proposed architecture was implemented in the Infineon -23x Tricore processor.

5.4 Current slope measurement

In this section we shall introduce a new strategies to obtain a robust current slope and compare it with available methods in the literature. There are three different methods presented in this section:

1. 2 point current slope measurement
2. Average current slope measurement.
3. Kalman Filter based current slope measurement.

5.4.1 Two point method

One of the main advantage of the two point method is that it is the easiest to implement and uses the least processor time. As noted in the last section this method is affected by the noise in the sampled current sensor. For example, consider Figure 5.8 which shows the current measured using the scope and sampled by ADC, it can be seen that based on the two points used for the slope calculation ,the amount of variation in the calculated slope can go from x amp/sec and x amps/sec. Using the current measure from the scope, the actual current slope is measured and the *Table 5.1* gives you the total percentage error in the slope calculated.

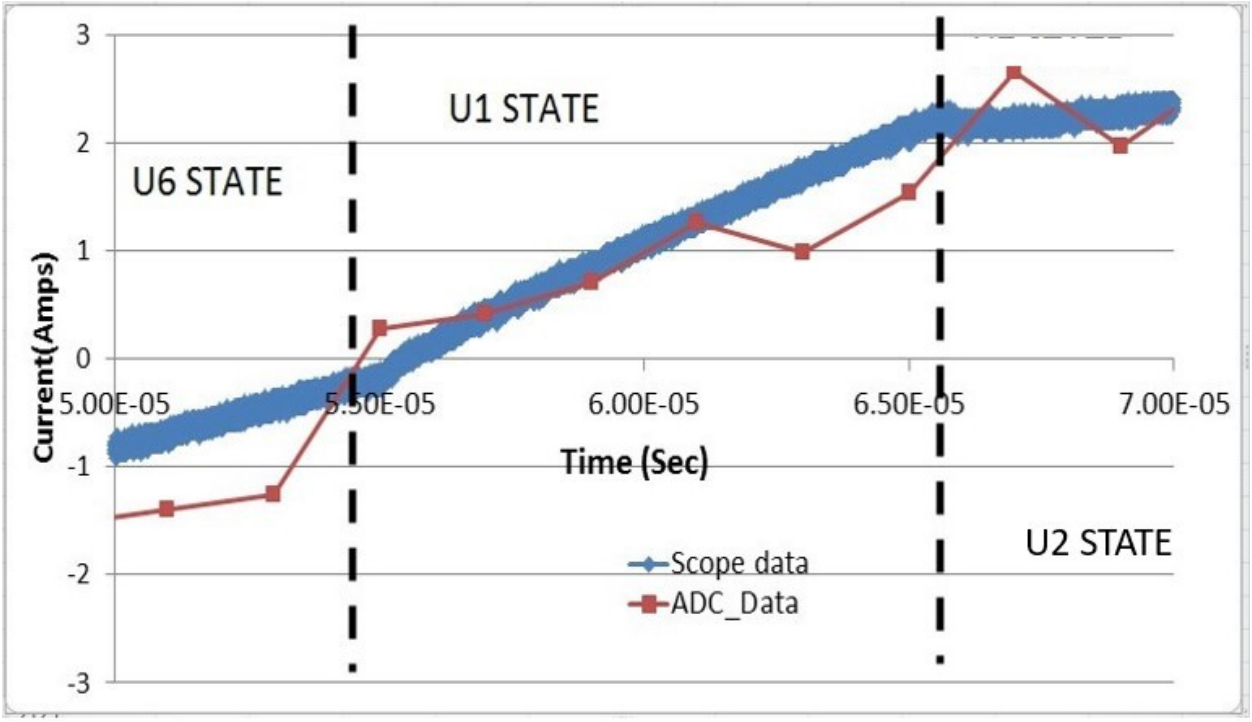

Figure 5.8: Measured phase current comparing scope Vs ADC sampled data

Method	Max Current Slope (Amps/sec)	Min Current Slope (Amps/sec)	Actual Current Slope (Amps/sec)	% Error
2 –Point	244000	134600	216656	13%- 38%

Table 5.1: Current slope variation seen in 2 point method strategy

Thus it can be seen that the two point method is greatly affected by the noise in the current sampled and therefore is not an optimal solution for current slope measurement.

5.4.2 Averaged current slope method:

This paper introduces an average current slope technique to minimize the effect of the noise in the sampled current. Eq.(5.7) shows the mathematical model on how to calculate the current slope to reduce the effect of the current noise. The main idea here is to use more than two sample to obtain the current slope. Additional samples can thus be used to average points thereby reducing the effect

of noise on the slope calculated. For the samples shown in Figure 5.8 the variation of the current slope thus obtained and the relative error from the actual slope compared with the two point method is shown in *Table 5.2*.

It can be seen that this method reduces the variation and also improves the accuracy of the current slope obtained. The effectiveness of this method totally depends on the no. of samples that can be obtained.

Method	**Max Current Slope (Amps/sec)**	**Min Current Slope (Amps/sec)**	**Actual Current Slope (Amps/sec)**	**% Error**
2 –Point	244000	134600	216656	13%- 38%
Average method	198750	168587	216656	8%-16%

Table 5.2: Current slope variation seen in 2 point method Vs average slope method

5.4.3 Observer based current slope measurement

Another methodology proposed to improve the signal to noise ratio of current slope estimated is to use a Kalman filter to reconstruct the current from the ADC sampled current data (for the given switching state) and then calculate the current slope from the reconstructed current . The idea here is to take the current sampled for the required switching state from the software buffer and pass it through an Extended Kalman Filter to reconstruct the current. The reconstructed current is devoid of any sampling noise but still maintain the slope information. The current slope is then obtained on the reconstructed current by taking two points and dividing by time. The system model for the Kalman filter can be given as

$$\hat{x}_k = Ax_{k-1} + w_k \tag{5.7}$$

where x_{k-1} represent estimated value in the previous cycle and the $\hat{x}_k$ represent the predicated value. The subscript k defines the sample time of the current sensor. As described in the previous section sampling time is set at 1us. It is to be noted that the Kalman filter is reconstructing based on the current sampled obtained every 1µs.

In Kalman filter the estimated value can be calculated from the predicted value and the actual measured current reading (z_k) as:

$$x_k = \hat{x}_k + K_k(z_k - \hat{x}_k) \tag{5.8}$$

The error between the predicted and the measured value is multiplied with a gain K_k which is added to improve the predicted estimate for each cycle. The multiplier gain K_k is calculated every cycle based on the accuracy of the estimated value. Figure 5.9 shows the current slope thus obtained. One drawback of this method is that the implementation of Kalman filter will add to the total software throughput. In this architecture since the current sampled is reconstructed, the minimum time t_{min} needed per switching state can be reduced compared to the other two methods. The Kalman filter is chosen compared to other methods such as Artificial Neural Network (ANN) proposed in [13] or recursive least square method (RLS) [14] because, it is a discrete filter and is easy to implement in the processor. The implementation of Kalman filter is given in Appendix B

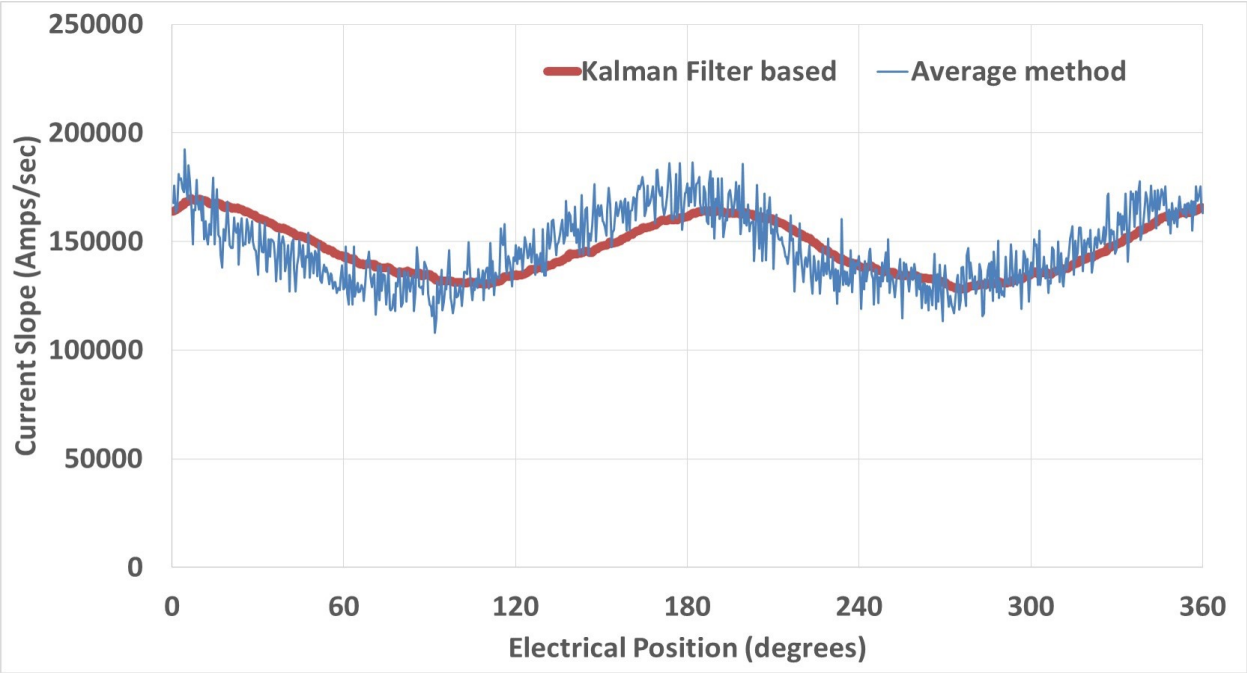

Figure 5.9: Current slope measured using proposed average slope and Kalman filter based approach

5.5 Experimental setup/ practical issues for a shunt based current measurement

Figure 5.10 shows the hardware schematic of the phase current measurement. Two shunt resistance are placed in line with the phase for measuring the phase currents. The sensor output is amplified through an amplifier. The amplifier output goes to the ADC for sampling. PWM frequency used for the motor drive control is set up to be at 16kHz.. The resolution of the current sensor after amplification is 10mV/Amp. The Infineon Tricore TC23X floating point processor has a 12 bit ADC with a resolution of 1.2mV/count. In the initial implementation, the PWM signals are phase shifted by an equal amount,i.e. each PWM signal is shifted 20.83us from each other. As explained in the Chapter 4 each PWM cycle has six different switching states. Therefore each switching state is about 10us when the duty cycle of each of the phases are 50%.

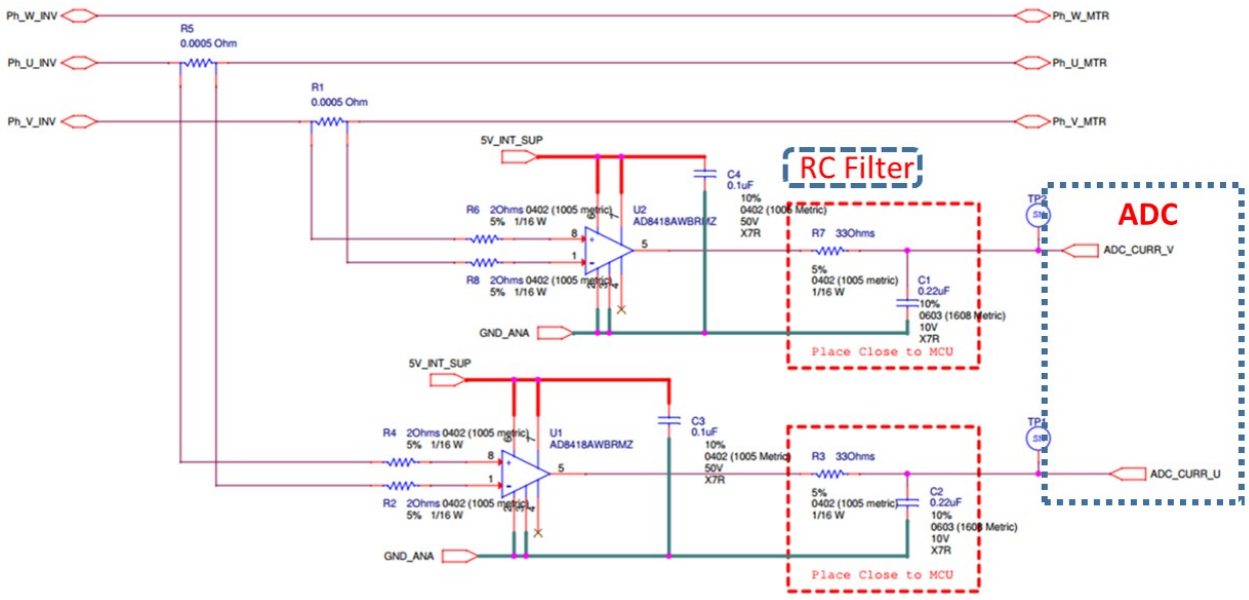

Figure 5.10: Hardware schematics for current measurement

One of the important factor that needs to be considered for current slope calculation using the shunt based measurement, is the effect of the various nonlinearities present in the current sampling. The

major nonlinearities comes from the poor Common Mode Rejection Ratio (CMRR) capability of the amplifier and the capacitive effect from the machine can influence the current slope. In a shunt based current measurement the common mode rejection characteristics of the amplifier can make the measured current deviate from the actual current.

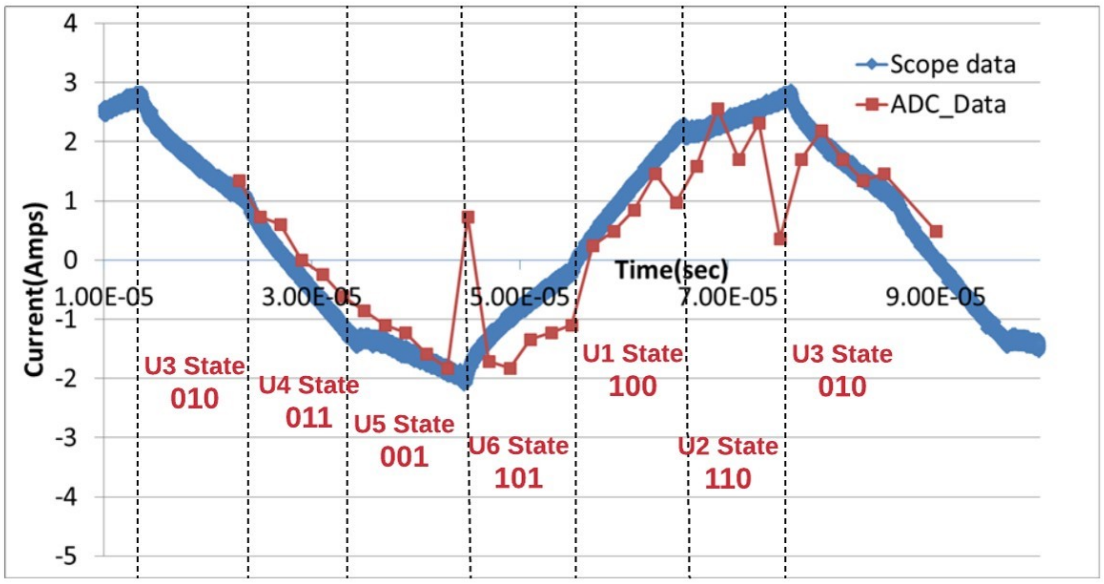

Figure 5.11: Current measured using the oscilloscope vs the ADC sampled Data

Figure 5.11 shows the current in phase A through ADC sampling, and measured from an external oscilloscope. The switching states corresponding to each slope is also shown. It can be seen that spikes seen in the ADC measured data is when the Phase A switches are turning on and off. This is due to the poor CMRR rejections ability of the amplifier. The ADC sampling noise for the 12 bit ADC used is also high. Due to these nonlinearities the ADC sampled data loses the information of the current slope needed for position estimation. With the cost of the high precision ADC and amplifier with high CMRR coming down, in future these issues will be resolved. This research

therefore moves ahead to prove the concept with the current measurement done using the external oscilloscope.

5.6 Conclusions

This chapter presented a practical approach to measure the current slope (di/dt) without using any additional hardware. The accurate measurement of di/dt measurement enables the use of fundamental PWM based sensorless technique to be used in wider application. This paper proposes an optimal current sampling architecture which can be easily implemented in processor keeping the software throughput to minimum. The architecture thus provides different techniques to obtain an accurate current slope measurement. The chapter proposes two new methodology to improve the accuracy of the current slope measured. Experimental results shows the difference of the proposed methodology versus the one available in literature. The di/dt calculated using the proposed scheme verifies the benefits of the proposed mechanism.

CHAPTER 6

Position Estimation using PWM Excitation Method with Minimized Ripple Current

6.1 Introduction

Chapter 5 discussed a novel architecture to obtain robust current slope (without involving processor overhead), which is key to estimating position accurately using PWM excitation. One of the challenges in obtaining the current slope is that the sufficient time for phase current measurement under all operating conditions is not guaranteed. For example, in a center based PWM strategy as shown in *Figure 6.1*a, if we depend on measuring the Phase A current slope when A is high, while Phases B and C are low, the time to take a sufficient number of current samples may be insufficient. It is assumed that in order to calculate the slope, current is sampled and measured using an analog to digital converter at regular intervals of time. As explained in the previous chapter, in order to calculate the slope without the effect of noise, 5 to 10 samples of current are required. . Other than the center based PWM, other strategies include shifting the Phase B and C waveforms with respect to A. In *Figure 6.1*.b phase B and C are shifted by $1/3^{rd}$ and $2/3^{rd}$ of the PWM period. Another option is to keep B and C on the same center based control but they are shifted from Phase A as shown in *Figure 6.1*.c. It is to be noted that these control strategies can increase the total ripple current produced which is undesirable.

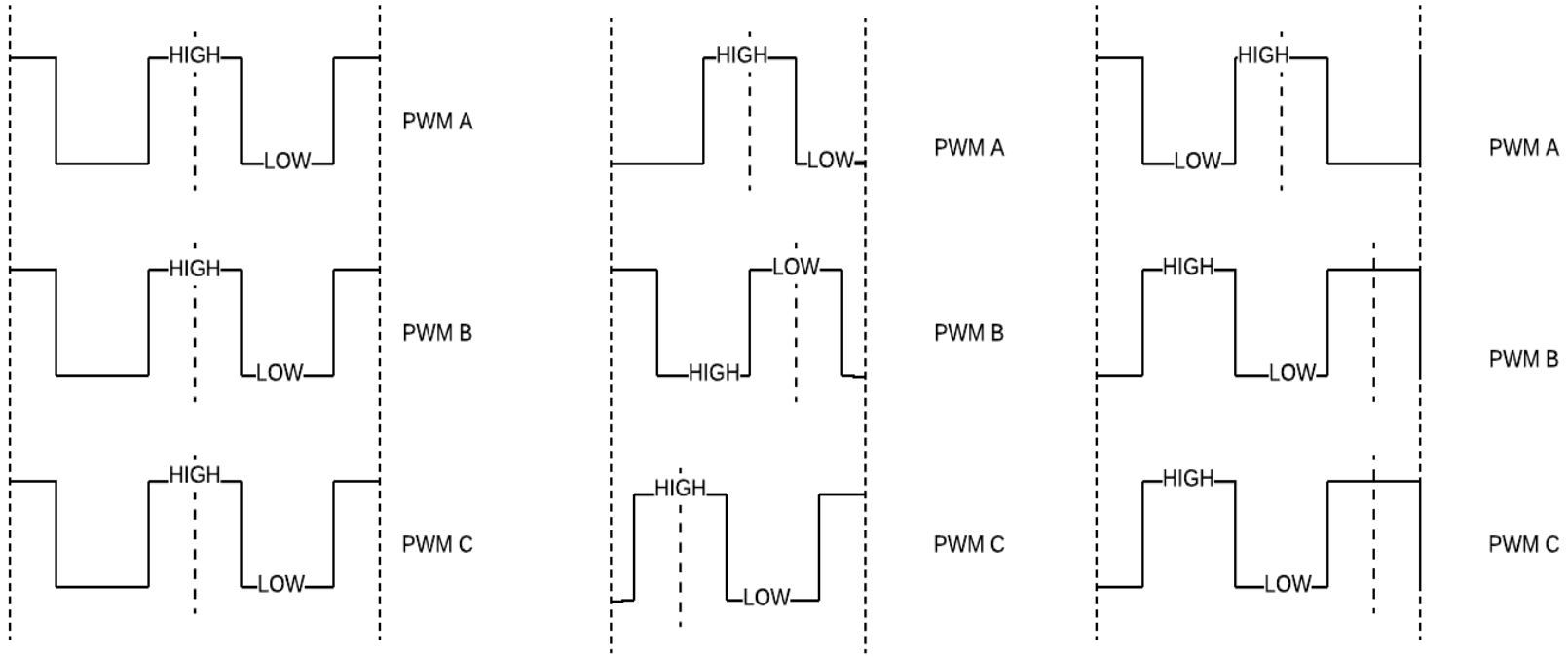

Figure 6.1:a) Center based PWM Scheme .b) Phase B and C shifted $1/3^{rd}$ and $2/3^{rd}$ c) Phase B and C shifted compared to Phase A

The peak to peak ripple current in d-q coordinates for the three different switching strategies is shown in *Figure 6.2*. It can be seen that the conventional SVPWM technique provides the least current ripple, and as the phase shift increases the peak to peak current ripple also increases. In available literatures, there have not been enough studies performed to understand the optimum phase shift strategy for various operating conditions that will allow a robust current to be measured while keeping the ripple current to a minimum.

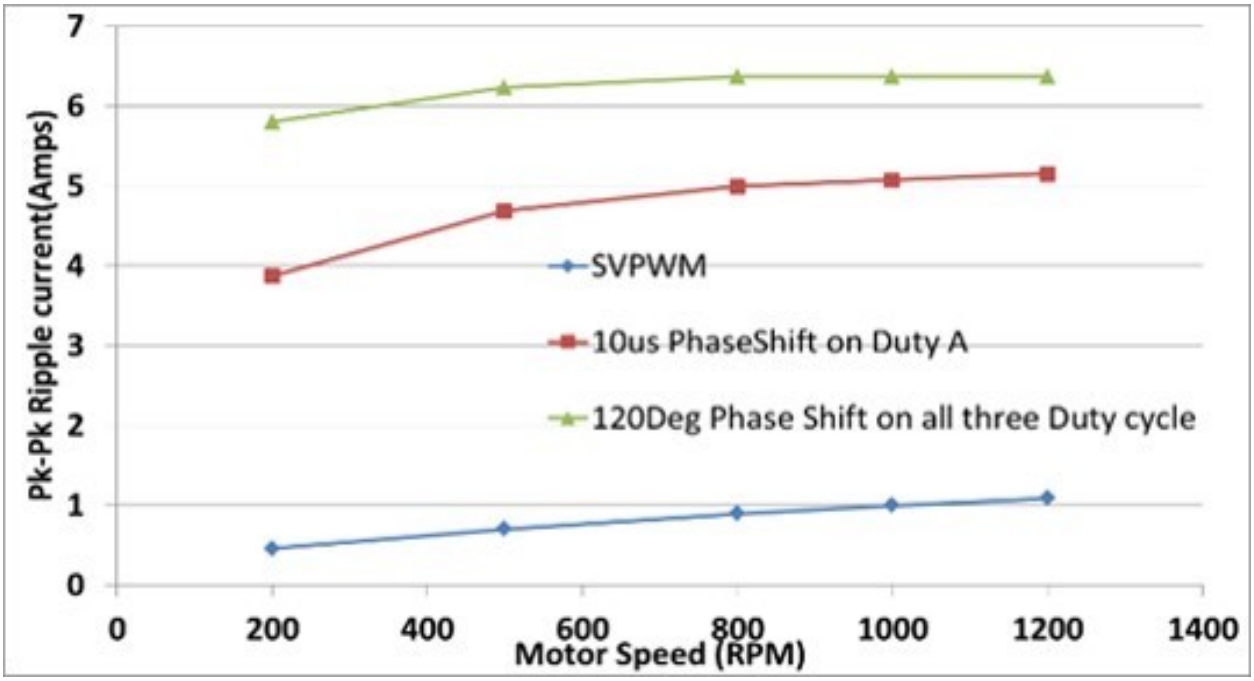

Figure 6.2: Comparison of total Pk-Pk ripple current (Amps) for various PWM strategies used for PWM excitation

The main objectives of this chapter are:

1. To identify appropriate switching strategy to ensure sufficient time for reading current to ensure proper position estimation while minimizing the ripple current.

2. This chapter explains the adaptive observer technique used for both position as we all as inductance estimation.

3. To present position estimation strategies for accurate estimating position at various operating conditions.

This chapter is organized as follows, section 6.2 defines the optimum switching state needed for robust current slope measurement while keeping ripple current at a minimum. Section 6.3 introduces the Extended Kalman Observer (EKO) model based inductance and position estimation for the low and medium speed range. Section 6.4 talks about position estimation during special conditions such as zero speed and high speed scenarios. Section 6.5 presents supporting experimental results.

6.2 Optimum strategy for position estimation with reduced ripple current

From Chapter 4 and 5 it is clear that the basic principle behind estimating rotor position using the PWM excitation is to determine the saliency in the rotor which is position dependent. Determining rotor saliency is achieved through measuring the rate of change of current. In the conventional SVPWM technique there are 6 active switching states, U1 to U6, and two inactive switching states, U0 and U7, as shown in *Figure 6.3*

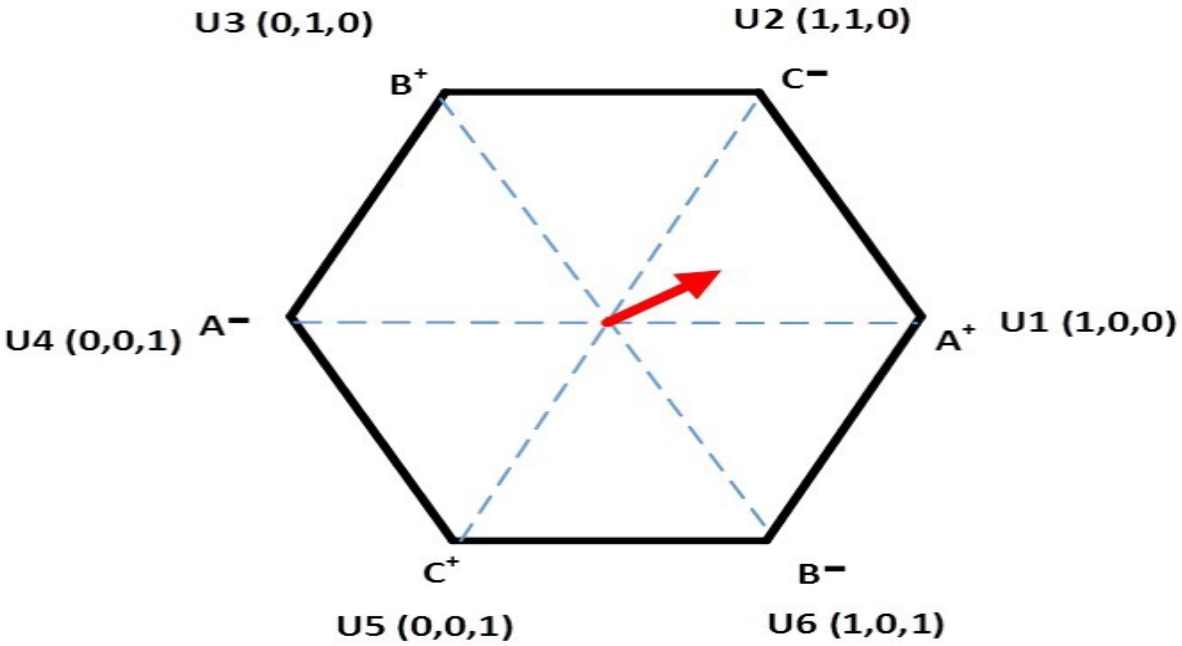

Figure 6.3: Switching state definition

From Chapter 5 section 5.2 it is clear that in order to negate the effect of both resistance drop and BEMF in the current slope, we need to measure current from an active switching state and an inactive switching state. It is noted that the effect of resistive drop and BEMF can also be negated by measuring the current slope from two opposite active vectors. The three pairs of opposite active

switching vectors are defined as (U1, U4), (U3, U6) and (U5, U2) based on *Figure 6.3*. The expression for current slope for switching state U1 and U4 is given as:

$$\frac{di_{a\_u1}}{dt} = \frac{1}{L_{1eq}}[V_{dc} - i_1 r_{eq} - e_1] \tag{6.1}$$

$$\frac{di_{a\_u4}}{dt} = -\frac{1}{L_{1eq}}[V_{dc} - i_4 r_{eq} - e_4]$$

Assuming the BEMF term $e_1 \approx e_4$ and $i_1 r_{eq} \approx i_4 r_{eq}$ by subtracting the $\frac{di_{a\_u1}}{dt}$ and $\frac{di_{a\_u4}}{dt}$ terms, the effect of resistive drop and BEMF can be cancelled. Thus the current slope can now be expressed as:

$$S_{U1} = \frac{di_{a\_U1}}{dt} - \frac{di_{aU4}}{dt} = \frac{2V_{dc}}{L_{1eq}} \tag{6.2}$$

The current slope S_{U1} as shown in (6.2) is proportional to 1/ L_{1eq} . The term 1/ L_{1eq} as shown in section 4.3, can be expressed as dc and 2nd order components. Similarly, the current slope (after eliminating resistive drop and BEMF) for all the switching states can be expressed as:

$$\begin{aligned} S_{U1} &= S_{off} + S_{amp2} * \cos(2 * \theta_e) \\ S_{U3} &= S_{off} + S_{amp2} * \cos(2 * (\theta_e - 120)) \\ S_{U5} &= S_{off} + S_{amp2} * \cos(2 * (\theta_e - 240)) \\ S_{U4=} &-S_{U1},\ S_{U6=} -S_{U3}\ ,\ S_{U5=} -S_{U2} \end{aligned} \tag{6.3}$$

In order to estimate the current slope we need one active switching state and one inactive switching state, or two opposite switching state vectors. The availability of these switching states are dependent on the duty cycle applied. As explained in Fig 6.2, in order to maintain minimum current ripple the conventional SVPWM approach is the optimum method. Unfortunately, the conventional PWM strategy does not guarantee that there is one active switching state and one inactive state, or two opposite switching states available through the entire operating range. A switching state is considered "**available"** for current slope measurement if the switching state time

$t > t_{min}$. In order to determine t_{min}, the total time for switching transition current ripple to die down as well as the ADC sampling rate must be considered. In this research the t_{min}, is set at 8µs.Figure 6.4 shows the available switching states, when modulation index is zero for a conventional SVPWM. The y- axis corresponds to switching states U0 through U7. A solid line on the graph means that the corresponding state is "**available**". Since there are no active states are available when modulation index is zero, as shown in Figure 6.4, we can conclude that estimating inductance is not possible when using a conventional PWM strategy.

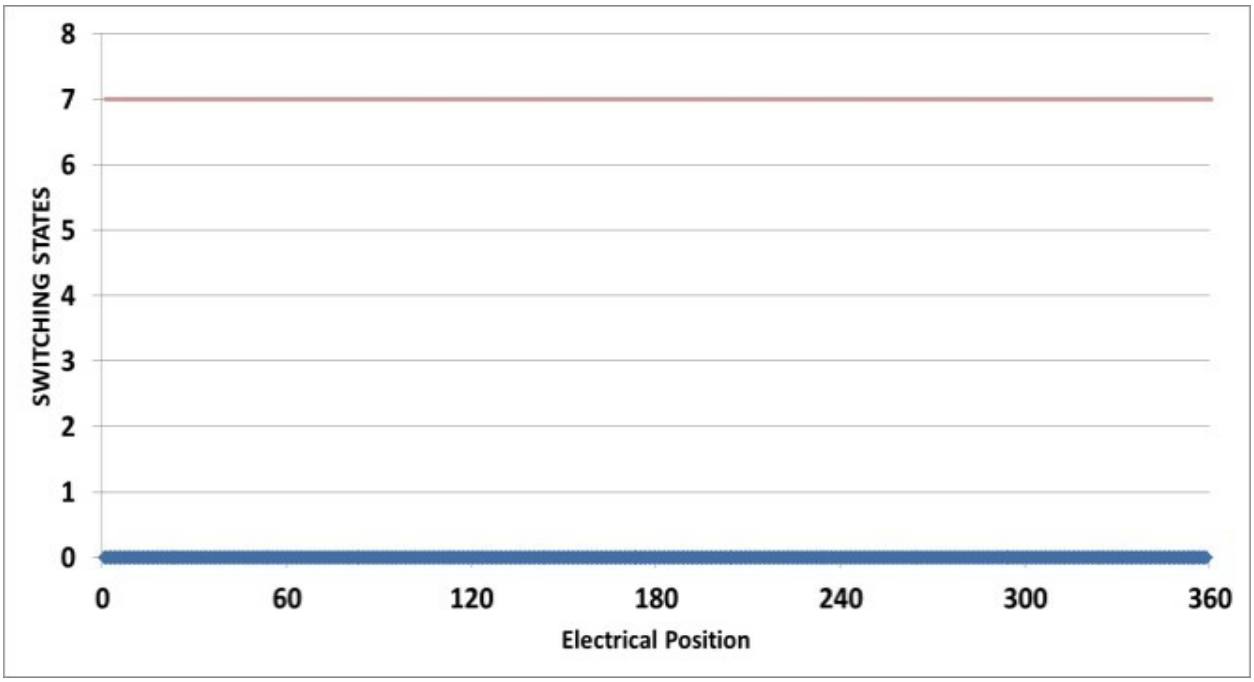

Figure 6.4: Available switching states for conventional SVPWM at Modulation Index=0

Phase shifting one of the phase pulses with respect to other two phases provide the next best strategy for low current ripple. The current ripple is a function of amount of phase shift applied and therefore phase shift is kept as small as possible. *Figure 6.5* shows the minimum amount of phase shift needed for the phase A pulse with respect to Phases B and C as function of Modulation index (MI), in order to ensure one active switching state and one inactive switching state is available to measure current slope.

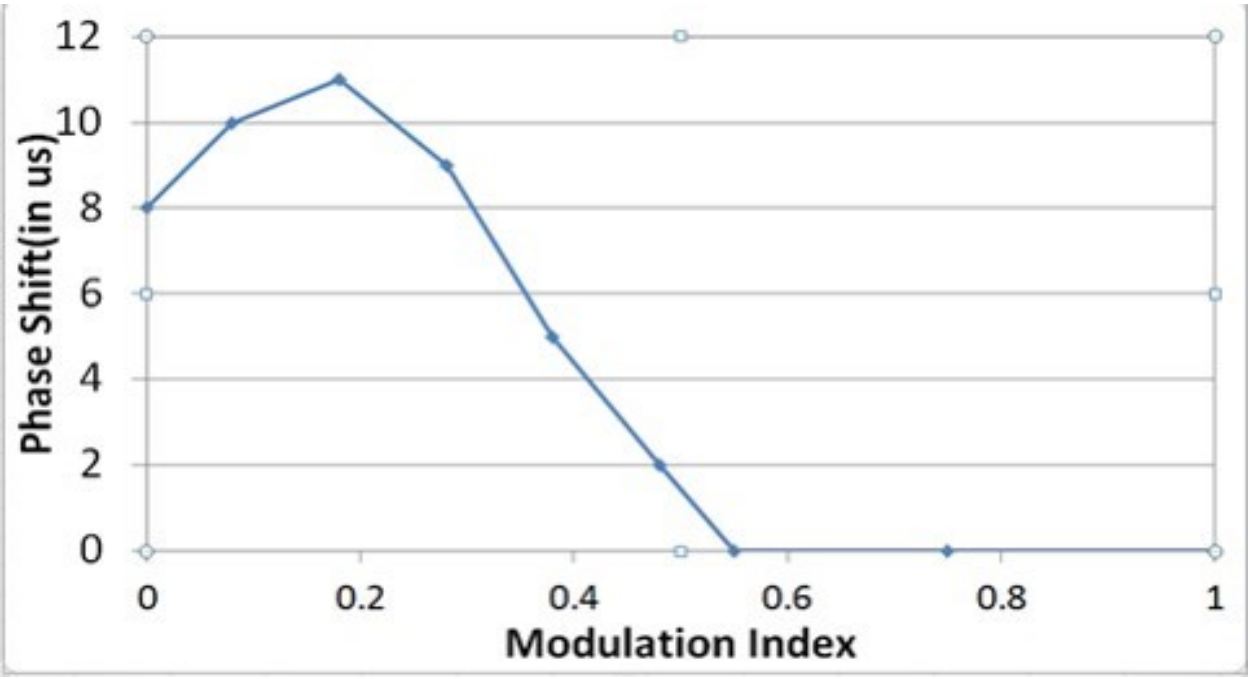

Figure 6.5: Amount of phase shift needed in the applied PWM as function of MI to have one active switching state and one inactive switching state available

It can be seen that by phase shifting A pulse 8μs with respect to B and C phases the switching state U1 and U4 becomes available at 0 modulation index as shown in *Figure 6.6*.

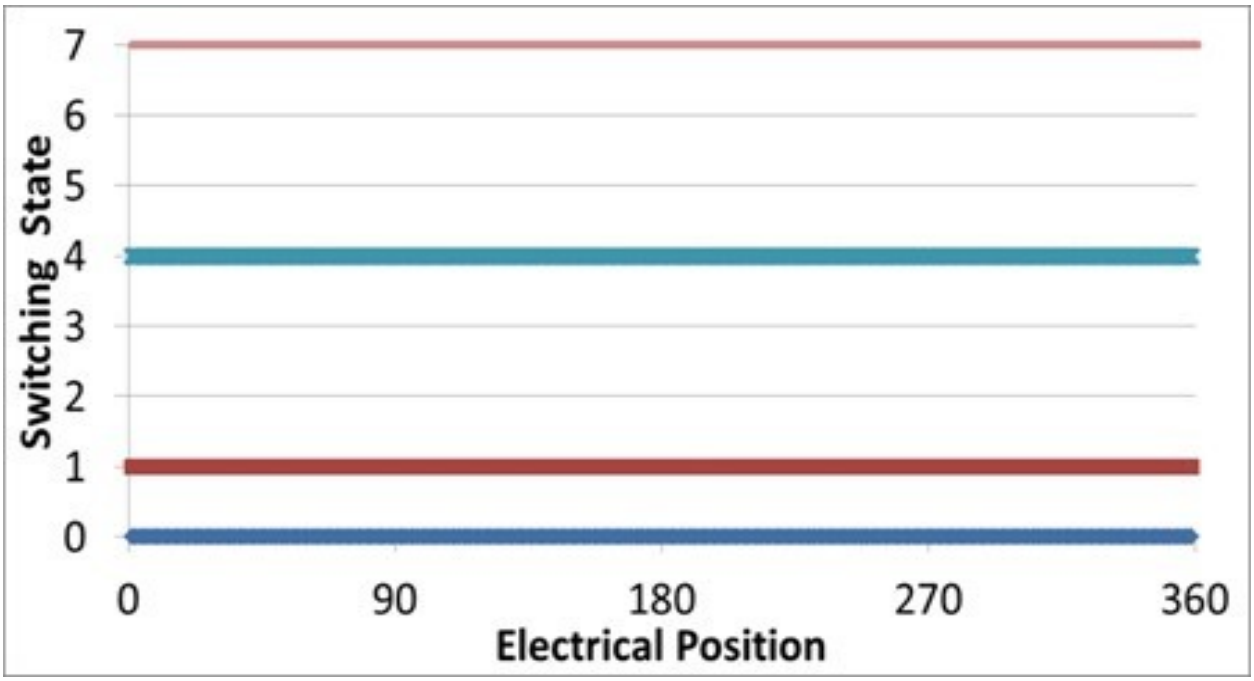

Figure 6.6 : Available switching states at MI=0 with 8us phase shift

The switching states which are available changes based on modulation index. *Figure 6.7* and *Figure 6.8* shows various switching states available for different modulation indexes. It can be seen that for a very low modulation index (between 0-0.1), by phase shifting the A pulse for 8-9us compared to phases B and C, the active switching states U1 or U4 become available during the entire electrical cycle. As the modulation index increases, the amount of time U1 and U4 are available change as a function of electrical position. In order to cover the entire electrical cycle, the phase shift must be increased to 10us for MI=0.1. *Figure 6.7* shows that, using U1 and U4 switching states we can robustly obtain current slope for the entire electrical cycle. For a modulation index of 0.3 and greater, other switching states become available which are able to cover the entire electrical cycle, this is shown in *Figure 6.8*. Therefore, for MI equal or greater than 0.3, we can decrease phase shift while maintaining availability of an active and an inactive switching state for the entire operating range.

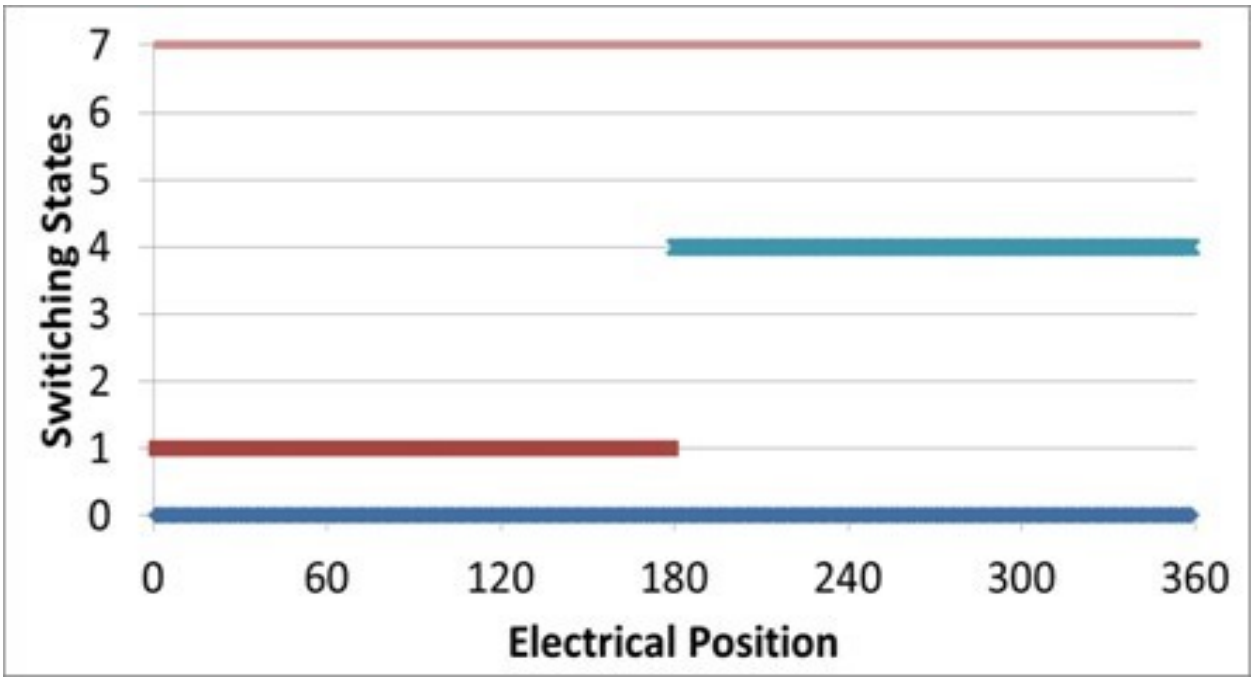

Figure 6.7: Switching states available for 10us Phase A pulse shifted: MI = 0.1

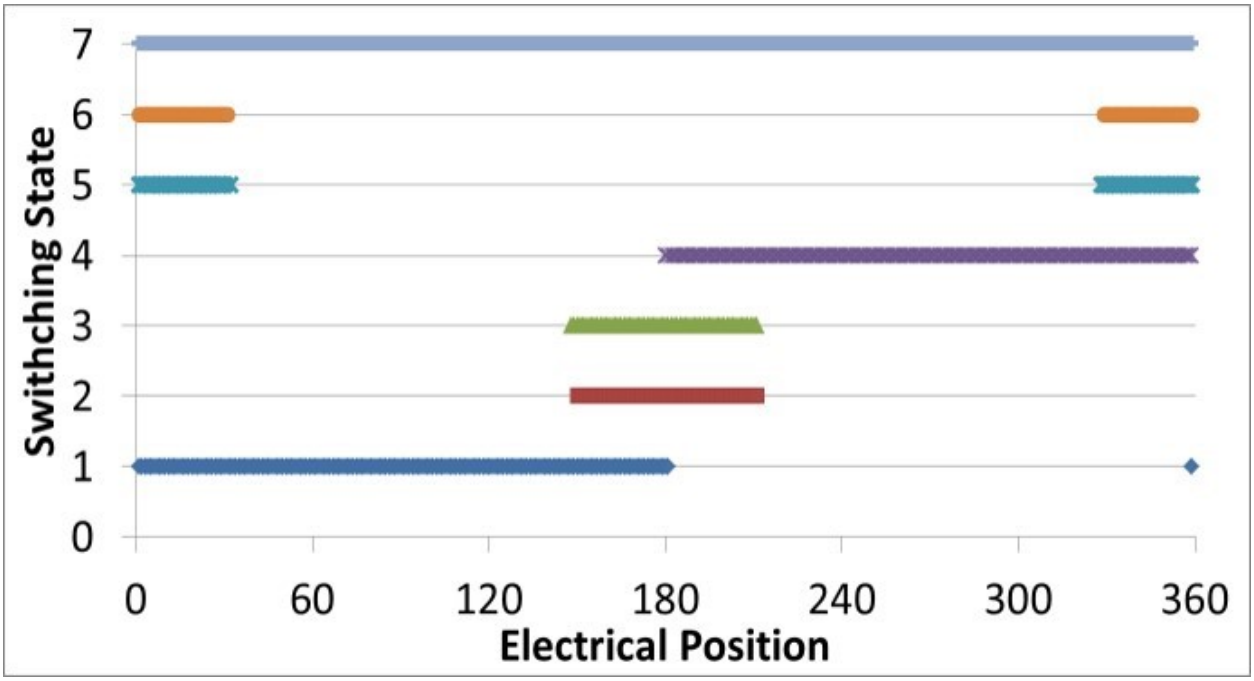

Figure 6.8: Switching states available for 9us of phase shifted phase A pulse: MI=0.3 to 0.48

For modulation index in the range 0.48-0.75 the conventional SVPWM strategy can be used without any phase shift. As shown in *Figure 6.9*, one active switching state and one inactive switching state is present over the entire electrical cycle, thus, inductance/position estimation is possible without any phase shift, which is optimal to maintain the lowest possible ripple current.

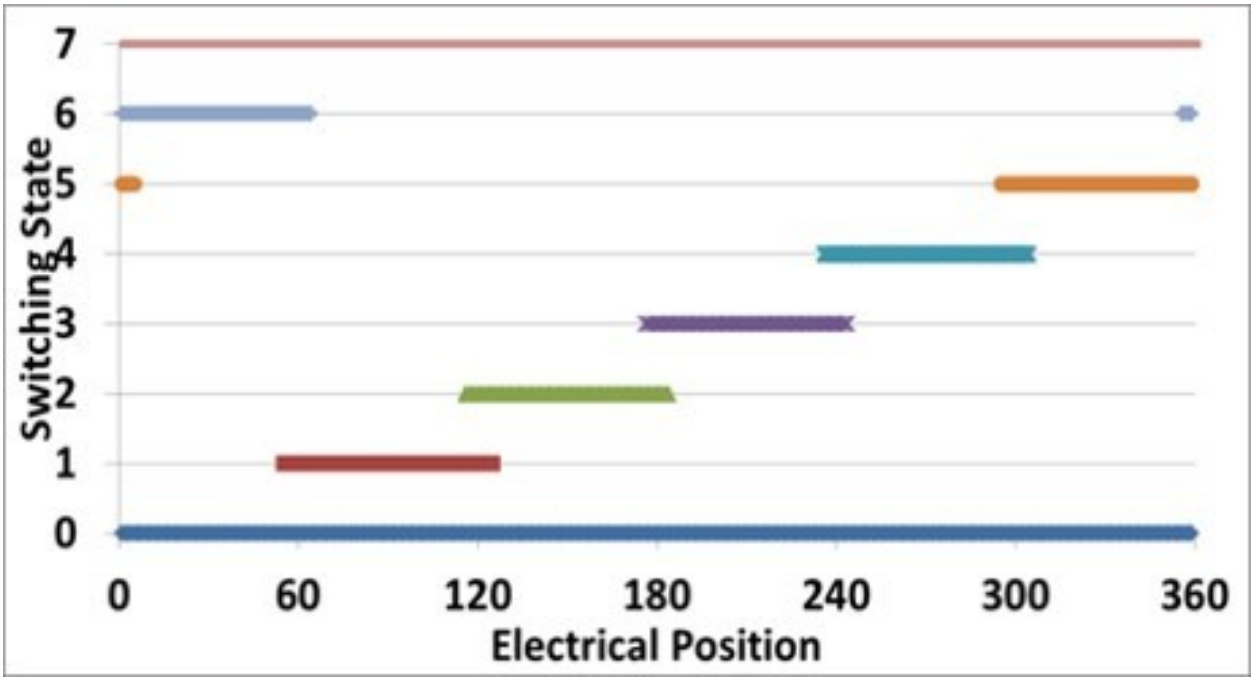

Figure 6.9: Switching states available for conventional SVPWM at MI =0.48 to 0.75

For modulation index greater than 0.75, the inactive switching states (U0 and U7) are no longer available over the entire range, thereby making the estimation of inductance not possible. *Figure 6.10* shows the available switching states for modulation index above 0.75 for conventional PWM.

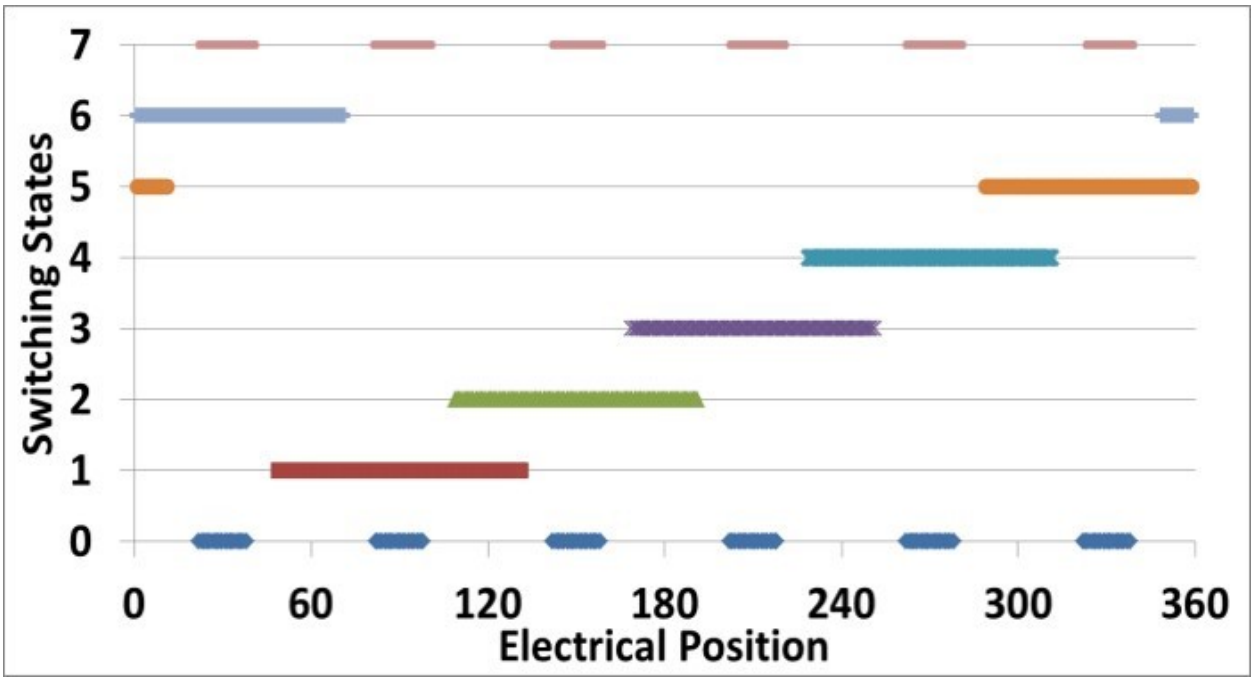

Figure 6.10: Switching states available for conventional SVPWM at MI>0.75

It is to be noted that during this operating range phase shifting phase pulses doesn't help to make the inactive switching state available and therefore position estimation above modulation index of 0.75 needs to employ different strategy. This will be discussed in section 6.4. Thus, it can be concluded that amount of phase shift needed changes with Modulation index and position and this section clearly shows that after certain modulation index the conventional PWM switching can be employed to estimate position. Thereby keeping the ripple current at minimum.

6.3 Adaptive observer based inductance/position estimation

From Eq.(6.2) and Eq.(6.3), in order to calculate the S_{off} and S_{amp2} from the measured current slope and online observer is proposed. The general block diagram of the observer based position/inductance showing the inputs and outputs is given in *Figure 6.11*. The "current slope calculation" block calculates the current slope for all switching states. As discussed in section 6.2, using the knowledge of the applied duty cycle, the optimum current slope (S_{opt}) needs to be identified. The "Optimum Current Slope Detection" block calculates the optimum slope and identifies the switching states used for the calculation. An adaptive observer is constructed in order to estimate different state variables. The state variables estimated differs for inductance and position estimation, this will be discussed in further detail in this section.

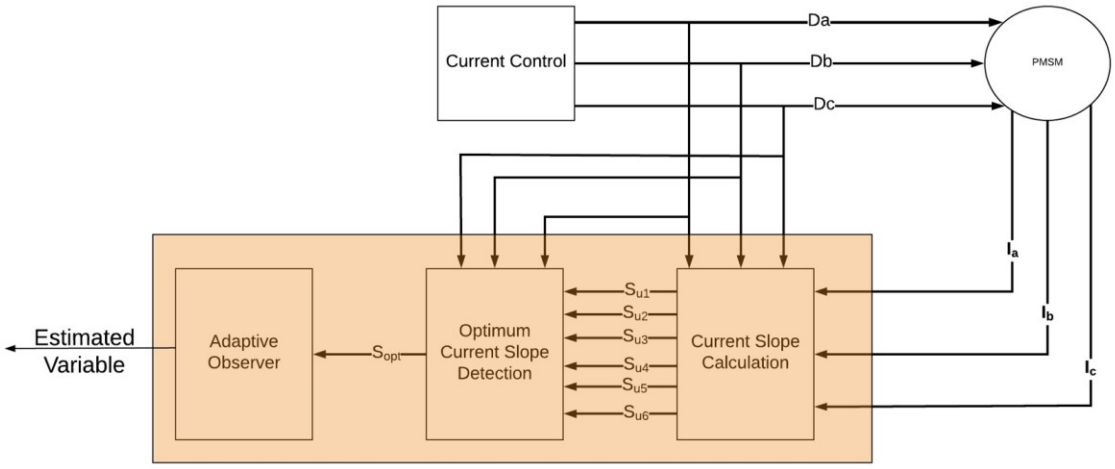

Figure 6.11: General block diagram for observer based position / inductance estimation using PWM excitation

In a linear time invariant system the state space equation in discrete form can be defined as:

$$\dot{\hat{x}}(t) = Ax(t) + Bu(t) + w(t) \tag{6.4}$$

$$y(t) \quad = C\hat{x}(t) + v(t)$$

Where x is the state variable; u is the system input; y is the system output; A, B, C are the system matrices. The w(t) and v(t) represent the process noise and measurement noise. If the system matrices, A, B, C and the input u are known, and by ignoring the noise in the measurement, we can build the identical system that runs in parallel to estimate the state variables defined as $\hat{x}(t)$ provided that the initial condition of the estimated $\hat{x}(0)$ is known. This method is called the open loop estimator. The open loop estimator is not feasible in practice as $\hat{x}(0)$ is not known, and because the noise in the measured input will cause further error in the estimation. An obvious way to fix this problem is to add a feedback loop to the system, using the difference between estimated output $\hat{y}(t)$ and the actual system output y to correct for the estimated system variable x. *Figure 6.12* shows a general closed – loop estimator.

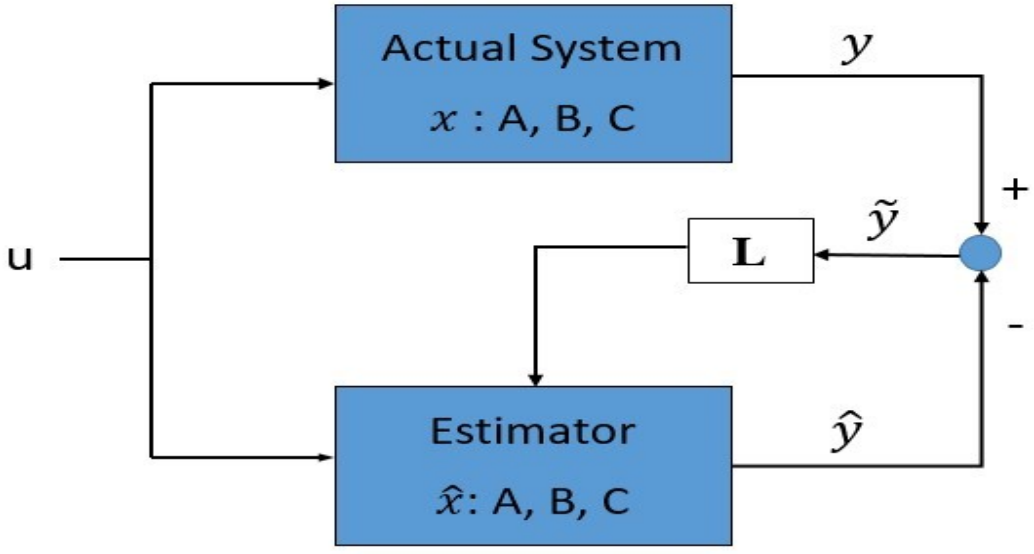

Figure 6.12: General block diagram of closed loop estimator

The observer system can be rewritten as:

$$\dot{\hat{x}}(t) = A\hat{x}(t) + Bu(t) + w(t) + L(y(t) - \hat{y}(t)) \tag{6.5}$$

$$y(t) = C\hat{x}(t) + v(t)$$

Where Lis the observer matrix. The L obtained can be calculated by either the Luenberger observer, the sliding mode observer or the Kalman Observer [62]. The goal of such an observer system is to ensure the estimated output $\hat{y}$ converges to the measured output y and eventually forces the estimated state variable $\hat{x}$ converge to the true value.

6.3.1 Inductance estimation

In the case for inductance estimation, as discussed in chapter 4, the idea is to estimate the DC offset S_{off} and the magnitude of the 2nd order harmonic S_{amp2} of the measured current slope from which the inductance can be calculated. For the selection of observer, the Kalman observer has unique advantages of a fast convergence speed, and is also robust against noise in the measurement. Moreover, the Kalman observer is a discrete algorithm, which lends itself easily for practical implementation in a processor. The Kalman observer is also a recursive algorithm which only uses the present and previous estimate, it requires minimal memory usage, also an advantage for practical implementation. From (6.3) it is clear that the current slope model is a non-linear model. The nonlinear version of the Kalman Observer, called Extended Kalman Observer (EKO), should be used in nonlinear systems as is the case here. The calculation process of an Extended Kalman Observer in general is explained in the *Table 6.1*

Table 6.1: Calculation process of EKO algorithm

Nonlinear system model

State Transition : $X_{t+1} = f(x_t) + w_t$

Measurement Model: $Y_{t+1} = h(x_t) + v_t$

Step I: Initialization

For t=0 Set $\hat{X}_0$ and C_0

Step II: Predict State Estimate and error Covariance

$\hat{x_t}^- = f(\hat{x}_{t-1})$

$P_t^- = \boldsymbol{A}_t C_{t-1} \boldsymbol{A}_t^T + Q$

Step III: Compute Kalman Gain

$K_t = C_t^- H_t^T (H_t C_t^- H_t^T + R)^{-1}$

Step IV: Compute the Estimate

$\hat{x}_t = \hat{x_t}^- + K_t(Y_t - h(\hat{x_t}^-))$

Step V: Compute the error Covariance

$C_t = C_t^- - K_t H_t C_t^-$

where , $\boldsymbol{A}_t = \left(\frac{\partial f(X_t)}{\partial X} \middle| X = \hat{x_t}^-\right)$, $\boldsymbol{H}_t = \left(\frac{\partial h(X_t)}{\partial X} \middle| X = \hat{x_t}^-\right)$

Q = Covariance matrix of w_t

R = Covariance matrix of v_t

Here, the subscript 't' indicates that it is the value at the present time t and subscript 't-1' indicates that the value from the previous sample at time t-1. In order to distinguish between predicted and estimated values at the same time, there are two superscripts. The superscript '-' indicates that the value is a predicted value, while the superscript '^' indicates that the value is estimated. The definition for the estimate and the error covariance are shown in *Table 6.2: Definition of the notation used in the Extended Kalman ObserverTable 6.2*

Table 6.2: Definition of the notation used in the Extended Kalman Observer

$\hat{x}_t$	Present Estimate of the state variables
$\hat{x_t}^-$	Prediction of the state variables
C_t	Estimate of the error covariance
C_t^-	Prediction of the error covariance

The state transition model for the inductance estimation is linear and can be modelled as:

$$\begin{bmatrix} S_{off}{}_{t+1} \\ S_{amp_2}{}_{t+1} \end{bmatrix} = \begin{bmatrix} 1 & 0 \\ 0 & 1 \end{bmatrix} \begin{bmatrix} S_{off}{}_{t} \\ S_{amp_2}{}_{t} \end{bmatrix} + \begin{bmatrix} w_{1_t} & 0 \\ 0 & w_{2_t} \end{bmatrix} \tag{6.6}$$

The measurement input used for correcting the predicted value, is the optimum current slope measured. It is noted that the model of the current slope measured is a nonlinear function as given in (6.3). Thus the measurement model is given as:

$$Y_{t+1} = h(S_{off}{}_{t}, S_{amp_2}{}_{t}, \theta_{e_t}) + v_t \tag{6.7}$$

It is also noted that the above measurement model changes based on the switching state at which the current slope is measured. For example, if the current slope is measured from U1 switching state, the measurement is modelled as:

$$Y_{U1_t} = S_{off_t} + S_{amp_{2\,t}} * \cos(2 * \theta_{e_t}) + v_t \tag{6.8}$$

For inductance measurement, it is noted that the position θ_e is measured from a position sensor. Therefore the estimation of position is not needed. The Kalman observer is implemented in a $62.5\mu s$ loop. The complete flow chart of the Extended Kalman Observer based inductance estimation method which is based on current slope measurement in the U1 state, is given in *Figure 6.13*. It is noted that the initial values for the estimated values S_{off} and S_{amp_2} are computed from the nominal values of *d* and *q* inductance and nominal bus voltage using equation (4.20). The terms S_{off} and S_{amp_2} estimated by the observer is used to calculate the *d* and *q* phase inductance using eq.(4.22) and eq.(4.7). The general block diagram of observer based inductance estimation is given in *Figure 6.14*.

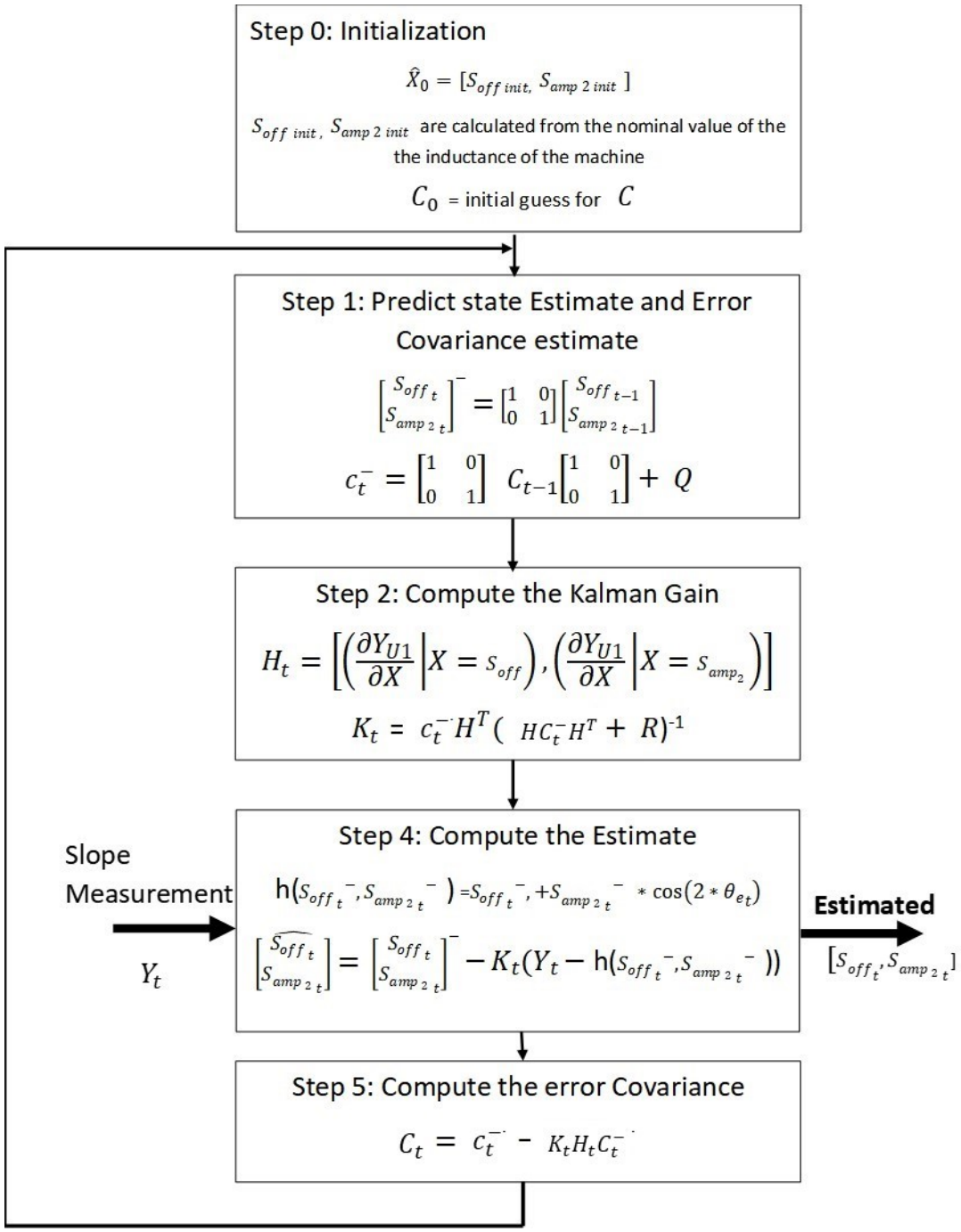

Figure 6.13: Implementation flowchart of Extended Kalman Observer for inductance estimation

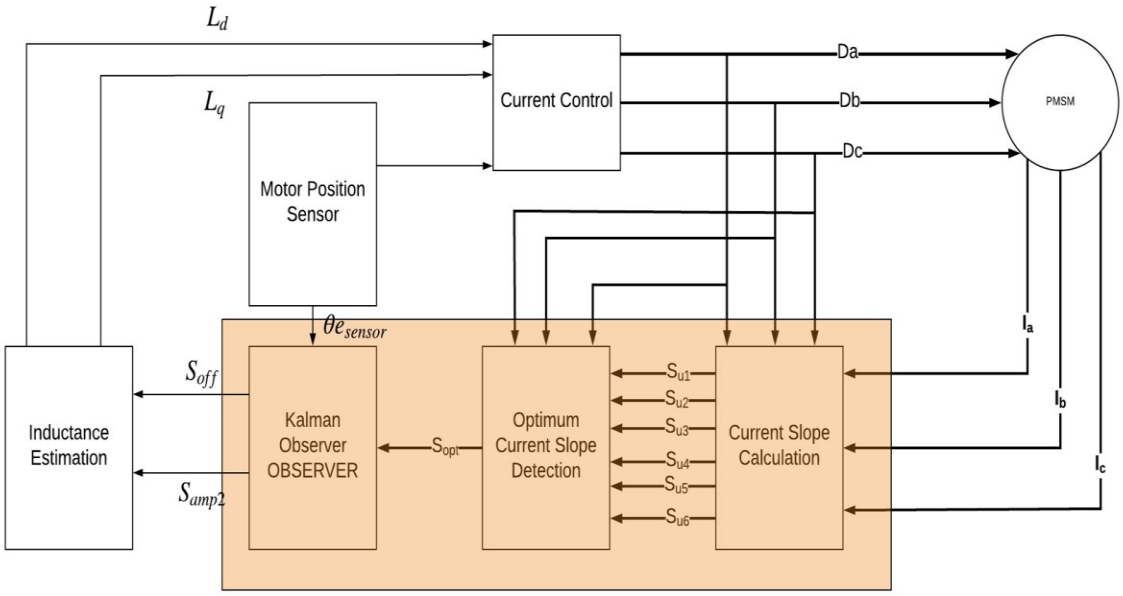

Figure 6.14: Block diagram for inductance estimation using EKO

Figure 6.15 and Figure 6.16 shows the observed DC bias S_{off} and the amplitude of the second order harmonic S_{amp2} calculated from the practical current slope measured using U1 switching state. The observed S_{off} and S_{amp2} is used for the inductance estimation as explained in Chapter 4. It is clear from the result that the observer converges within a few tenths of a seconds.

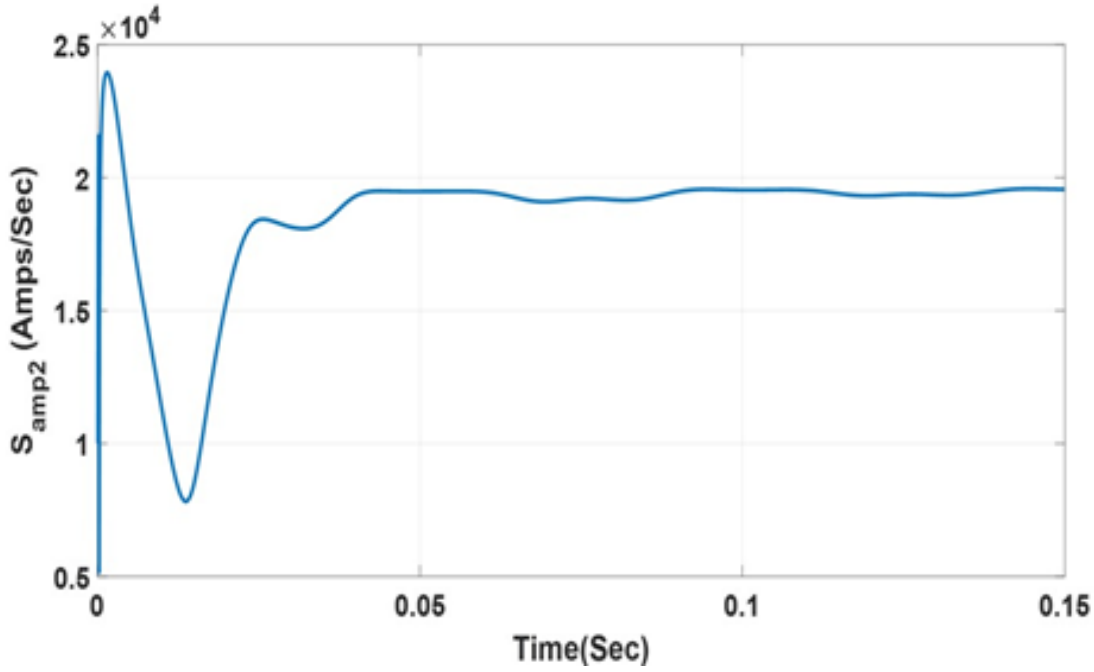

Figure 6.15: Estimated amplitude of the second order harmonics with initial condition Samp2 =0.1*10^4amps

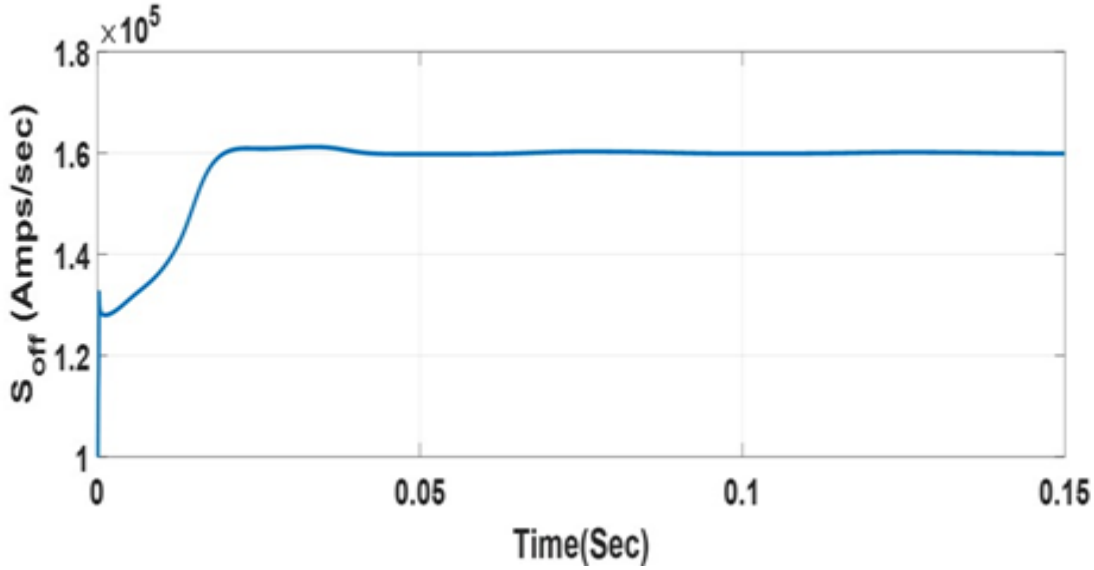

Figure 6.16: Estimated DC offset of the rate of change of Phase A current with the initial condition of Soff=0.1*10^5 amps/sec

6.3.2 Position estimation

In the case of Position estimation the Extended Kalman Observer (EKO) is constructed to track the rotor position θ_e, motor speed ω_e, the dc component of the current slope S_{off} and the magnitude of the 2nd order harmonic S_{amp2}. The discrete observer is implemented with a sampling time of $62.5\mu s$. The state transition model for the position estimation is linear and is given as:

$$\begin{bmatrix} \omega_{e\,t+1} \\ \theta_{t+1} \\ S_{off\,t+1} \\ S_{amp_2\,t+1} \end{bmatrix} = \begin{bmatrix} 1 & 0 & 0 & 0 \\ dt & 1 & 0 & 0 \\ 0 & 0 & 1 & 0 \\ 0 & 0 & 0 & 1 \end{bmatrix} \begin{bmatrix} \omega_{e\,t} \\ \theta_t \\ S_{off\,t} \\ S_{amp_2\,t} \end{bmatrix} + \begin{bmatrix} w_{1_t} & 0 & 0 & 0 \\ 0 & w_{2_t} & 0 & 0 \\ 0 & 0 & w_{3_t} & 0 \\ 0 & 0 & 0 & w_{4_t} \end{bmatrix} \tag{6.9}$$

The subscript t represents the value at the present sample time and the subscript t+1 represents the estimated value for the next sample time. The w_k matrix in the state model refers to Gaussian noise input, representing the maximum change in speed in the sample interval. The measurement model is the same as that which is explained in section 6.3.1. As discussed in section 6.2, the current slope measurement used for the position observer changes within an electrical cycle. Therefore, based on the input current slope passed to the observer, the measurement model used for calculating the estimated position must be updated per the model given in (6.3). The switching state that is used for the optimum current slope measurement is calculated based on the duty cycle applied. A software flag can be used to indicate the appropriate optimum switching state used for current slope measurement. The Kalman observer will make use of this software indicator to select appropriate state model. The block diagram for the observer based position estimation is given in *Figure 6.17* .

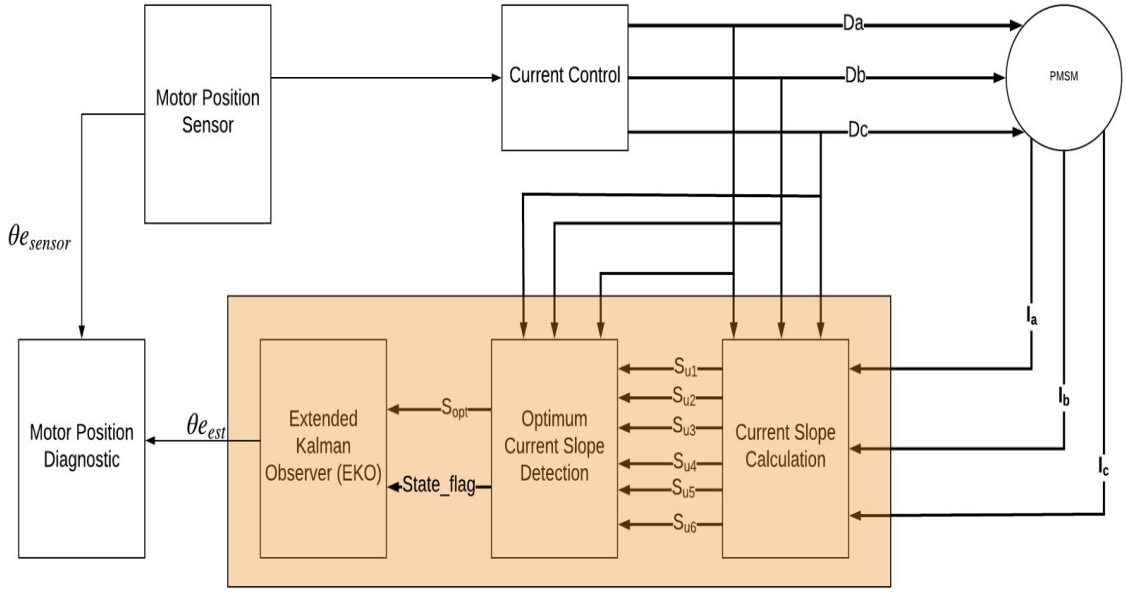

Figure 6.17: Block diagram for position estimation using EKO

In this research, the estimated position is used for diagnostic purposes rather than for controlling the drive. Therefore the initial position value is initialized from the primary position sensor reading. In this way, there is no need for an initial position detection algorithm. The complete flow chart based on current slope measured from the U1 state for the position detection is given in *Figure 6.18*. The measurement model shown in red (step 4), need to be modified based on the software indicator which will indicate the switching state used for the current slope measurement. The initial values for the S_{off} and S_{amp_2} are computed from the nominal values of d and q inductance and nominal bus voltage using eq. (4.20) and (4.7).

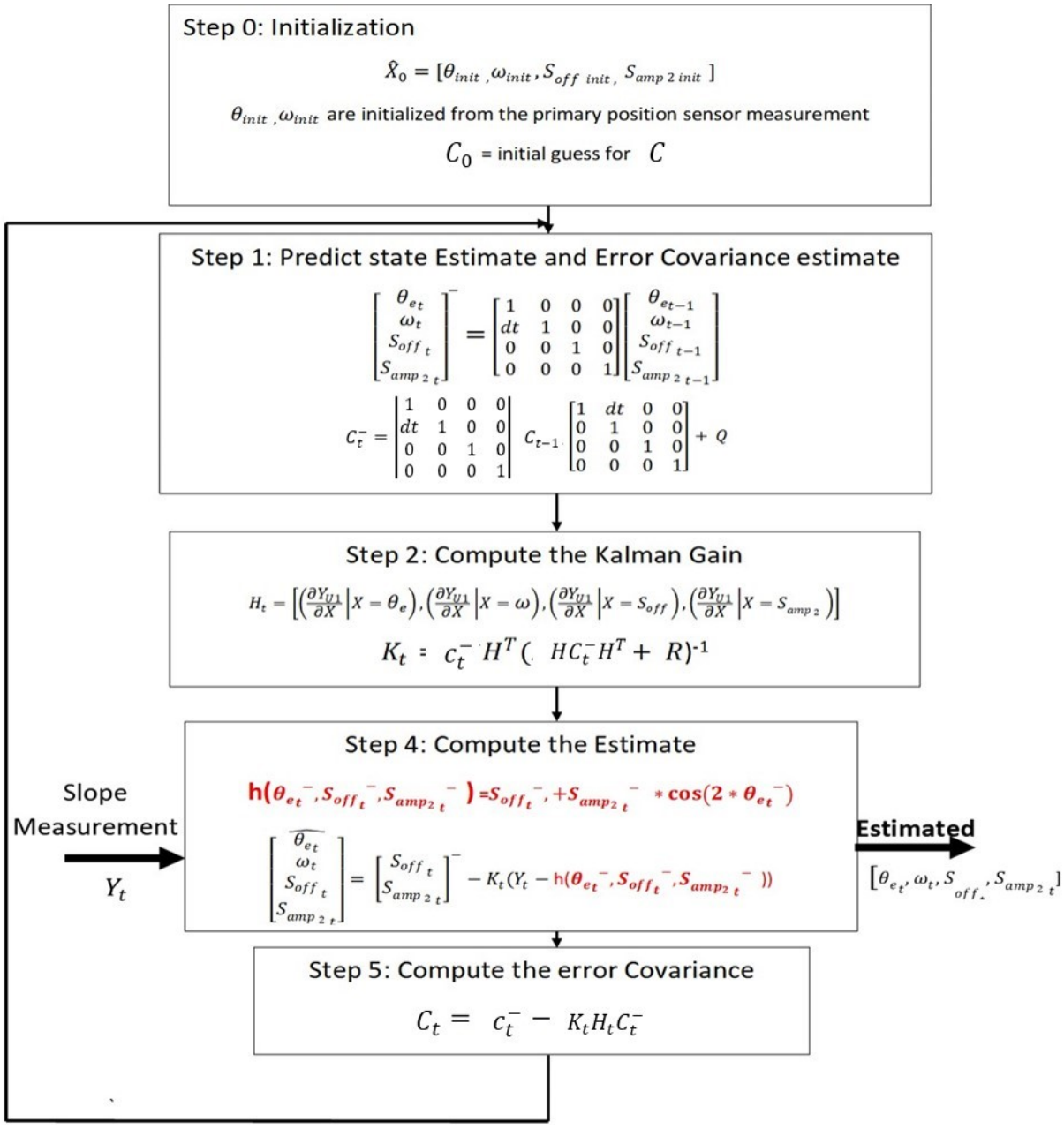

Figure 6.18: Implementation flowchart of Extended Kalman Observer for position estimation

6.4 Position estimation at high speed and zero speed

6.4.1 High speed

The observer based method discussed in the previous section does work at low and mid speed. From Section 6.2 it is clear that during high modulation index an optimum current slope measurement cannot be achieved as the inactive switching states (U0, U7) are not available over the entire electrical cycle, shown in *Figure 6.10*. In these scenarios the proposed position estimation would fail. During these operating conditions the motor is running at high speed where the BEMF based method suggested in literatures [5], [8], [63]can be deployed. The back emf based method is optimal to maintain lowest possible current ripple. It is to be noted that phase shifting the phase pulses doesn't resolve the issue. Another methodology that can be deployed is to increase the U7 switching state for the PWM cycle where the current is sampled and compensate for it in the adjacent PWM cycle to keep the average voltage the same. This method however will come at cost of increased voltage and current ripple. This technique is described in literatures [21], [59]

6.4.2 Zero speed

From section 6.2, the measured current slope is modeled as given in Eq.(6.3). From Eq.(6.3) it is observed that, to obtain the S_{off} and S_{amp_2} we need the measurement data for one complete electrical cycle is needed. Thus an observer based approach will not be able to converge at zero speed. Therefore another technique must be determined for the case where the speed is zero. The basic idea here is to obtain 3 balanced current slope shifted by 120^0 degrees using three active switching states and one inactive sector. From Eq.(6.2) it can be seen that current slope S_{U1}, S_{U3}, and S_{u5} are balanced scalars which are 120^0 degrees apart.

Once the balanced scalars are obtained they can be converted to orthogonal components P_α and P_β as:

$$P_\alpha = S_{u1} - \frac{1}{2}(S_{u3} + S_{u5}) \quad (6.10)$$

$$P_\beta = \frac{\sqrt{3}}{2}(S_{u3} - S_{u5})$$

The position can thus be obtained by taking the arctangent function as:

$$\theta_e = 0.5 * \text{atan}(\frac{P_\alpha}{P_\beta}) \quad (6.11)$$

From Eq.(6.3) we find that the current slope is a function of $2*\theta_e$. Therefore atan of orthogonal components P_α and P_β would result in $(2*\theta_e)$ and the resultant angle has to be multiplied with the 0.5 to obtain θ_e as shown in (6.11). One of the main disadvantage of this methodology is that it requires three active switching state and one inactive switching state to be available to calculate the position. Various studies [21], [22], [59], [64] published discuss the architecture proposed for zero speed in this literature to estimate position. In these literatures three active switching state and one inactive switching state are used to estimate position. In order to make three active switching state and one inactive switching state available the amount of phase shift needed is around 35us which results in approximately 8 amps of peak-peak current ripple. In order to reduce current ripple, phases B and C are shifted by 1/3rd and 2/3rd respectively of the PWM period inorder to reduce current ripple. The amount of peak to peak current ripple using the proposed phase shifting strategy is shown in *Figure 6.2*. It can be seen that the total peak to peak current ripple in this scenario is around 6 amps.

Figure 6.19 shows the switching states available for optimum current slope measurement as function of position for the proposed strategy. Note that the availability of switching states shown in *Figure 6.19* is only true for low modulation index. Since this method is only used at zero speed, the modulation index range will be within 0-0.1.

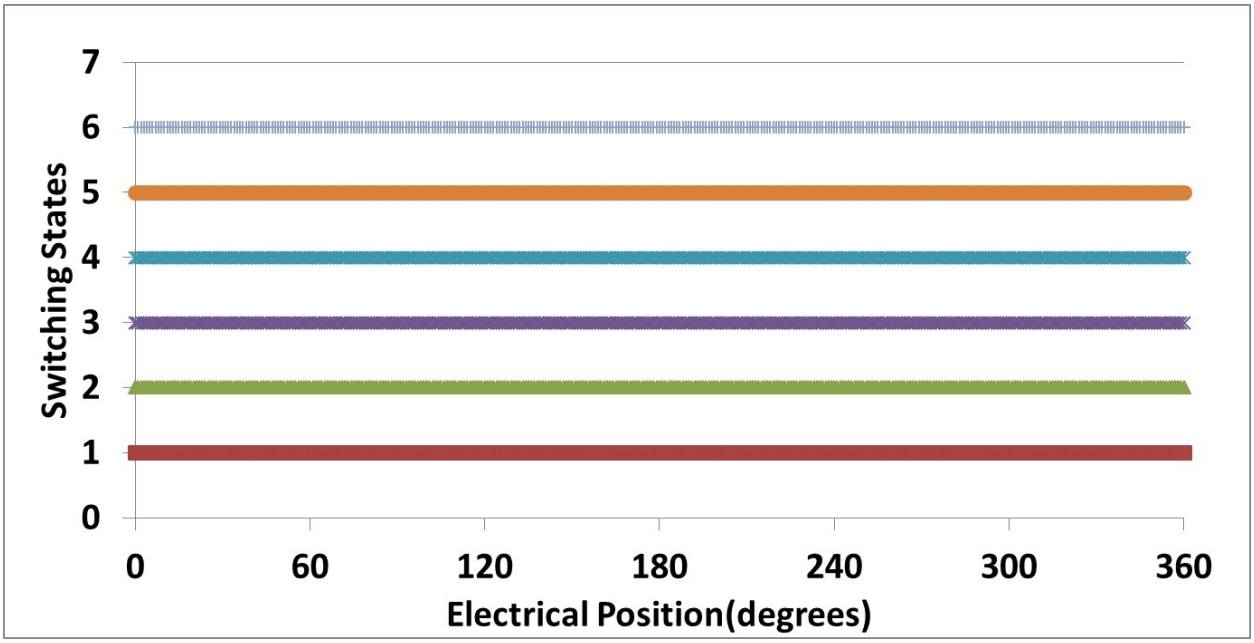

Figure 6.19: Switching state available for Phase B and C shifted by 1/3rd and 2/3rd of PWM period at MI=0.1

It can be seen from *Figure 6.19* that the inactive switching states U0 and U7 are not available, therefore to cancel the resistive drop and the BEMF effect U4, U2, and U6 switching states must be used. The position estimated is without the use of any observer therefore it would work well at zero speed.

6.5 Practical Results

Figure 6.20 shows the test set up. An IPMSM machine is connected to a dynamometer which can run the motor at any given constant speed. A Hall Effect motor position sensor is used for the primary control of the machine. The phase current and the applied duty cycle are measured to calculate the optimum current slope. The data is collected at different operating ranges to show the feasibility of the observer output. The estimated position is plotted against the actual position from the position sensor.

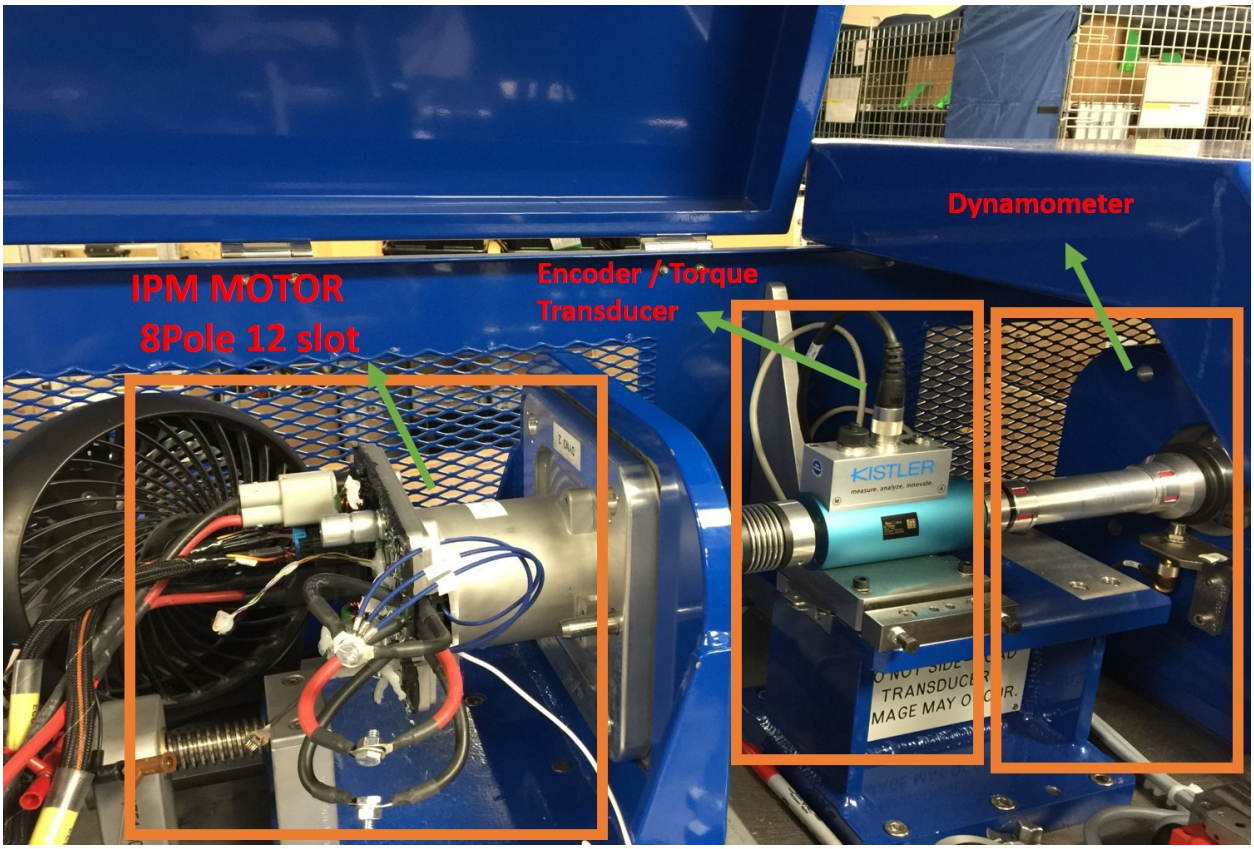

Figure 6.20: Experimental setup for position estimation

As seen in section 6.2 the number of switching states used per electrical cycle for position estimation is a function of duty cycle. *Figure 6.21* shows the result of position estimation at low

modulation index where only one active switching state and one inactive switching state is used. Note that the estimated position in the first cycle has larger error compared to other cycle because the observer needs one full cycle to calculate the S_{off} and S_{amp2}. Also note that the current slope plotted, is after we subtract the current slope obtained in the U0 switching state. This is to remove the effect of the resistive drop and the BEMF. *Figure 6.22* shows the plot of estimated position compared with the actual position.

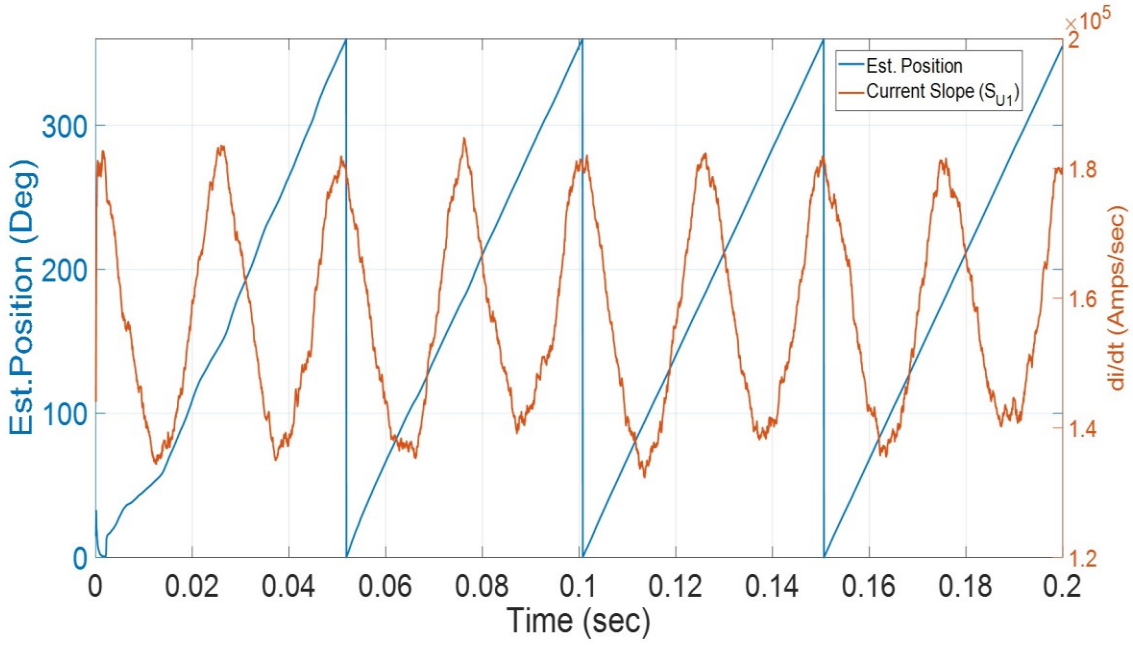

Figure 6.21: Estimated position using one active switching state U1 and U0 inactive switching state for MI=0.05

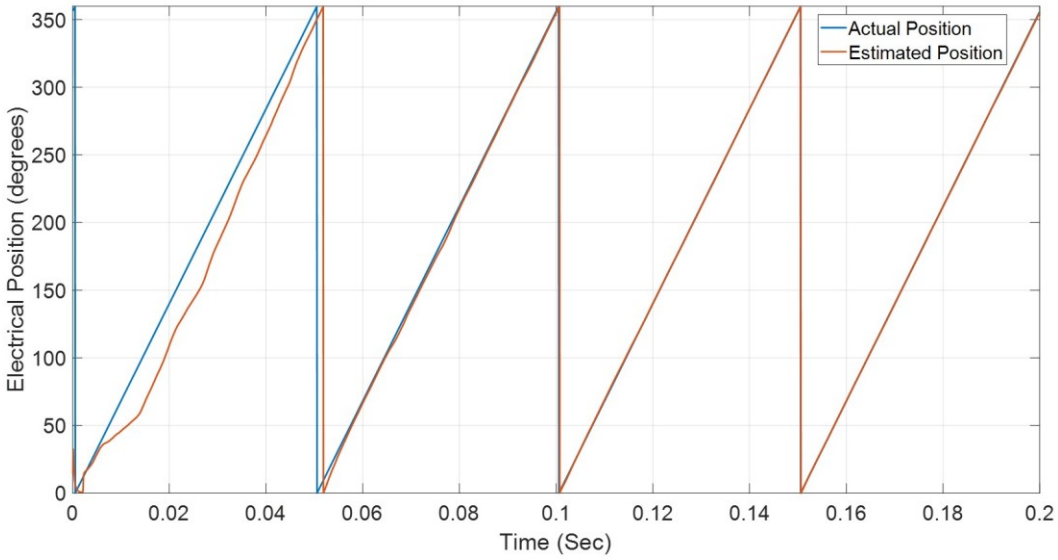

Figure 6.22: Actual vs estimated position at MI=0.05 using U1 and U0 switching states

Moving on to mid-range modulation index where two active switching states and one inactive switching state are required is shown in *Figure 6.23*. The two switching states used for computation of the current slope are U1 and U4. The transition from using U1 to measure current slope to using the current from U4 occurs at approximately 180 degrees rotor position. Based on the transition from U1 to U4, the measurement model in the Kalman observer is updated according to eq. (6.3). The transition from one switching state to another switching state is found not to affect the position estimated when the measurement model is correctly updated. The error between the estimated and actual position is presented in *Figure 6.24*. We can see that after the first cycle the error in position converges to zero. *Figure 6.25* shows the actual versus the estimated position with respect to time. It is to be noted that in both low modulation index range and mid modulation index range the PWM phase shift between phase A with respect to Phases B and C is 8 μs and 10 μs respectively as explained in section 6.1.

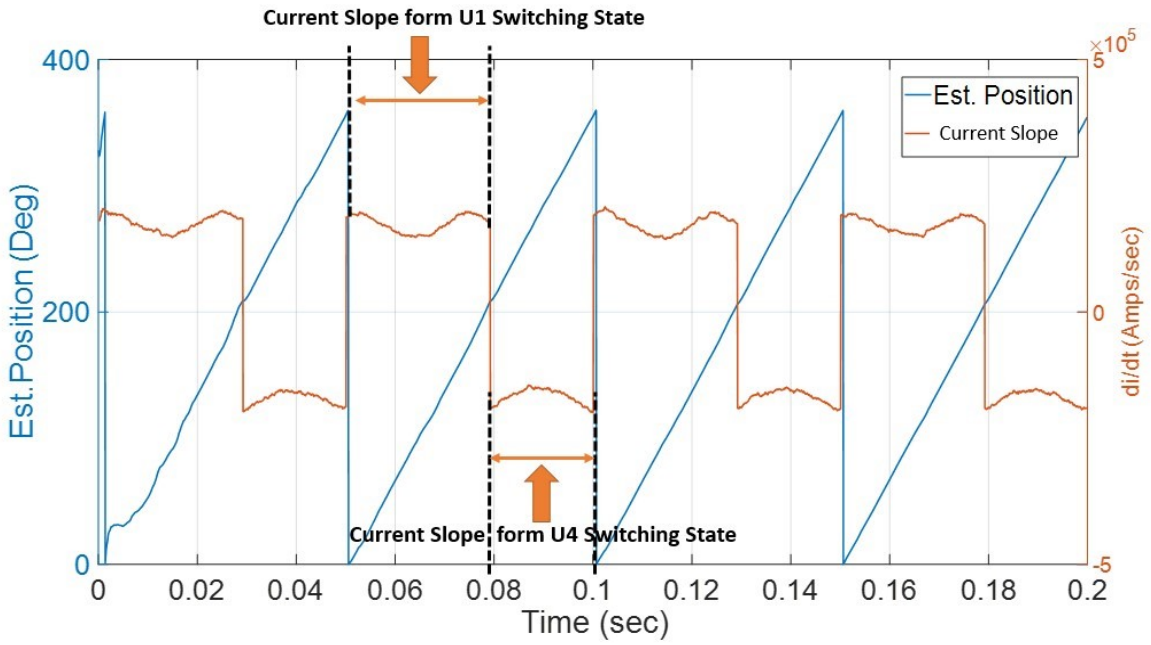

Figure 6.23: Estimated position using two active switching state U1 and U4 and one inactive U0 switching state for MI=0.32

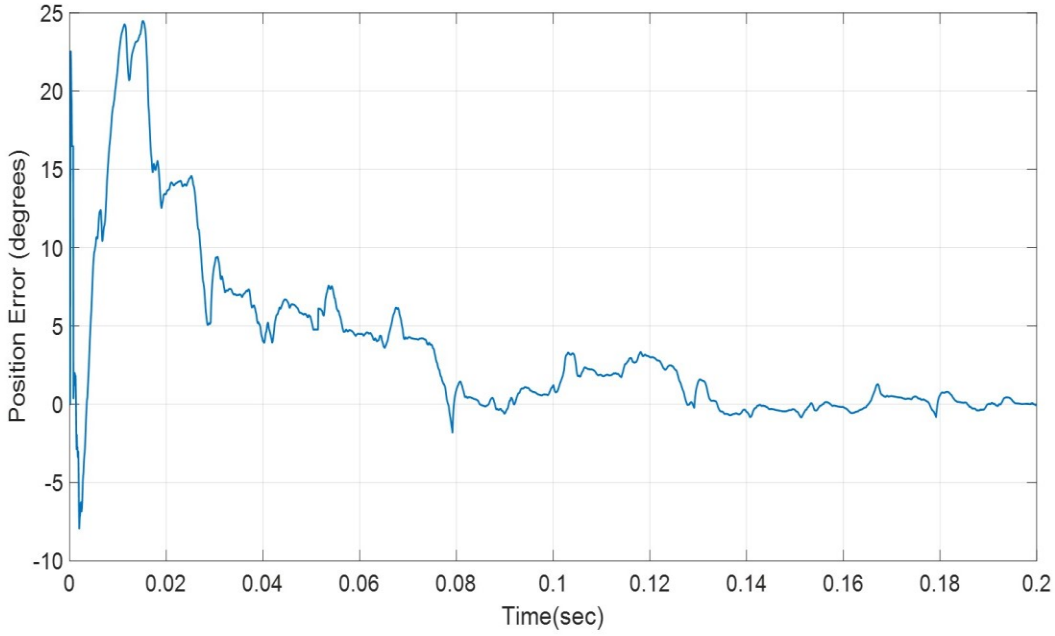

Figure 6.24: Error in position estimated at MI=0.32

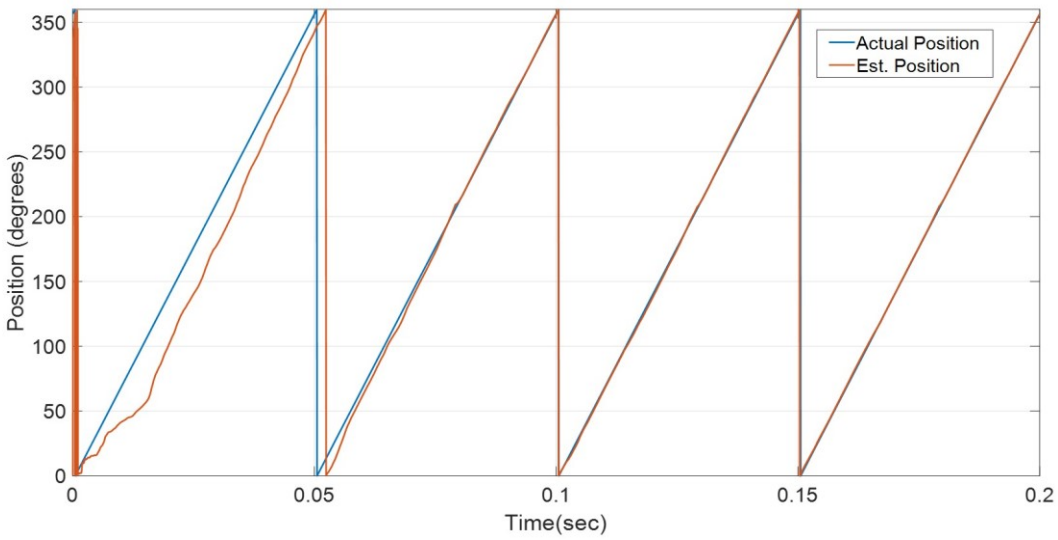

Figure 6.25 : Actual vs estimated position at MI=0.32

For the case where speed is zero, the current slope measured from U1, U3 and U5 switching states is shown in *Figure 6.26*. Note that the current slope plotted is after cancelling the effect of resistive drop and BEMF.

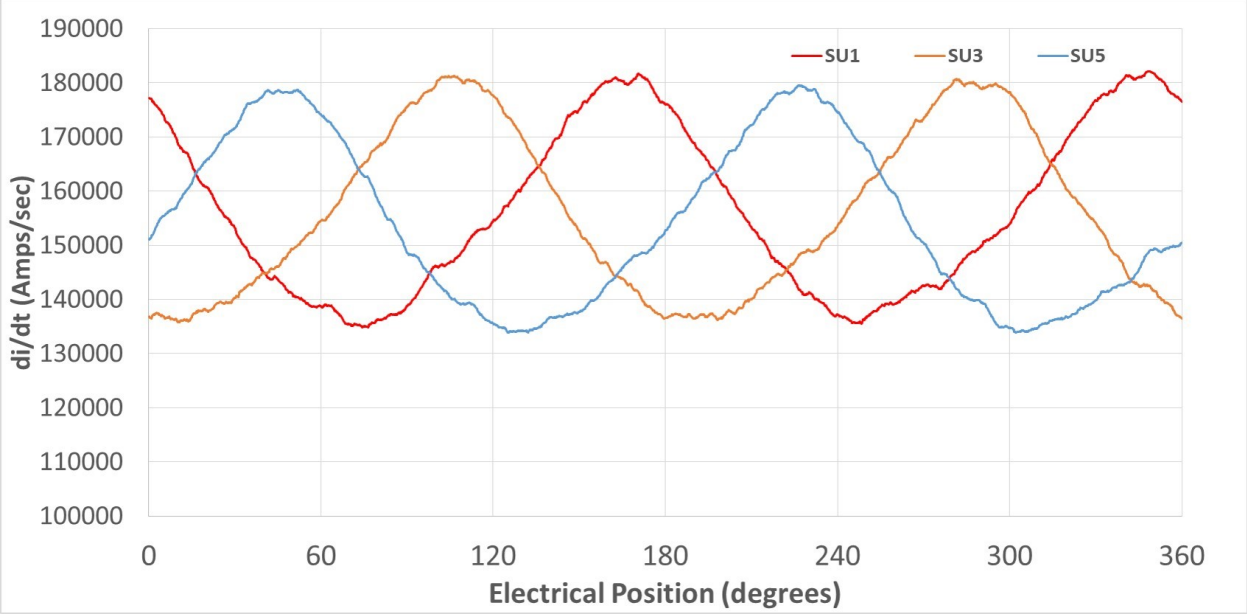

Figure 6.26: Current slope from switching state U1 , U3 and U5 for zero speed phase shifting strategy at Modulation Index=0.1

The position estimated for one electrical cycle is shown in *Figure 6.27*. Noted that the position estimated below uses the strategy described in section 6.4, not the observer. Thus this methodology would work when speed is zero. We observe from the experimental results that the position to tracks well with the actual position measured with the position sensor. The error in the estimated angle for a complete electrical cycle is shown in *Figure 6.28*.

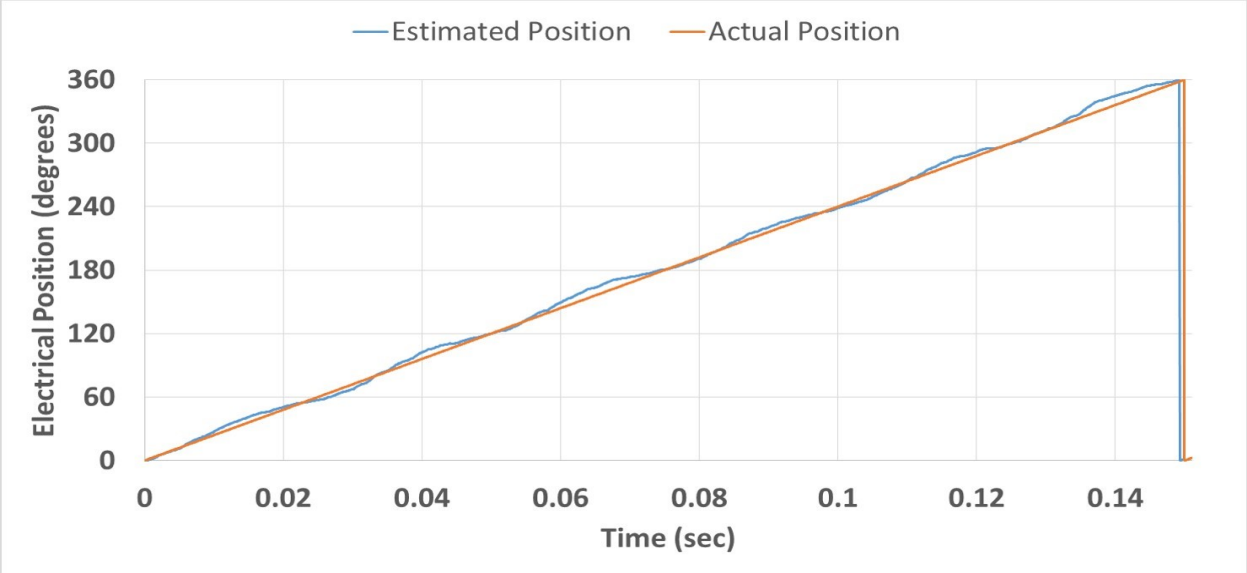

Figure 6.27: Position estimated compared with actual position for one electrical cycle at MI=0.1

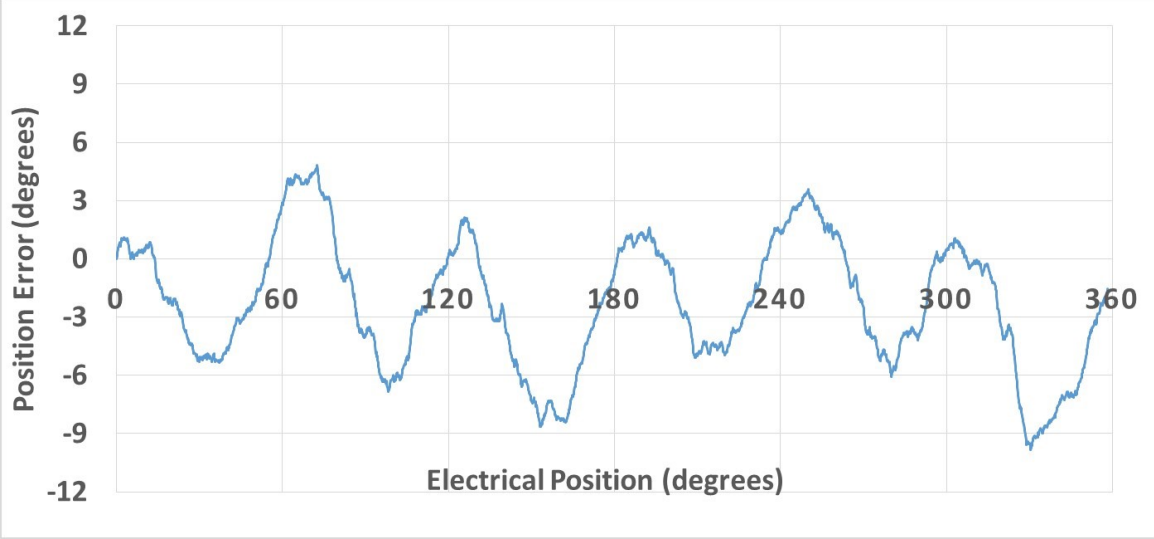

Figure 6.28: Error in estimated position for zero speed strategy

6.6 Conclusions

The work presented in this chapter analyzes the various operating regions of the motor to establish the strategies which can be used to obtain position using PWM excitation. This chapter initially analyzes the strategy needed to estimate position with the goal of maintaining minimum current ripple. This chapter then introduces a new Extended Kalman Observer (EKO) based position estimation technique. The EKO based position estimation reduces the number of switching states required for the position estimation, thereby reducing the modification needed to the traditional SVPWM. This reduces the amount of current ripple and makes it easier to implement. We noted that the observer based strategy does not work at zero speed and high speed. This chapter proposes phase shifting strategies at zero speed which are distinct from the strategies proposed in the current literature with the advantage of minimizing the total peak to peak current ripple. When considering high speed operation, this chapter uses well established BEMF methods to estimate position. Thus, strategies for position estimation with minimal undesirable effects (such as current ripple) have been provided for the complete operating range of the drive. Various experimental results for low, medium and zero speed operating conditions are provided which show the effectiveness of the proposed methods.

CHAPTER 7

Conclusions and Future Works

Rotor position and online inductance estimation of an IPMSM, using PWM excitation used for motor control have been presented in this thesis. Position information is required for proper control of the motor. The position estimation proposed in this research provides an alternative solution to adding redundant position sensor hardware in order to satisfy the requirements of safety critical systems. Proper control of the IPMSM requires accurate knowledge of the inductance parameters. Thus online estimation of the inductance improves the motor drive performance.

Chapter 2 analyzes the effect of position sensor error on the PMSM drive system. First, this chapter analyzes the effect of position sensor error on the measured current. This chapter provides a mathematical model for the effect of position error as a function of *id* and *iq* currents. Next, the effect of position error on the torque generated is analyzed. A mathematical model for the torque ripple generated as a function of position error is developed. The developed model clearly shows the various torque ripple harmonics created due to position sensor error as a function of *id* and *iq* currents. Various practical results showing the effect of position error on current and torque are compared with modelled results. The experimental results obtained validate the developed model.

Chapter 3 is focused on building the foundation for the inductance and position estimation, by understanding phase inductance variation with respect to position. The analysis done in this chapter is with respect to the motor under study. In order to build the model for the phase inductance, the chapter begins with single phase inductance testing. The testing is done to identify

the single winding inductance parameters. The result thus obtained is verified with FE analysis. The mutual inductance from coils one slot and two slot apart, are studied and various result based conclusions are drawn. Finally the model for the phase self-inductance, and mutual inductance between phases is developed. The relationship of the phase inductance parameter with the single winding inductance parameters is also shown. The model thus developed for phase self-inductance and mutual inductance form the basis of analysis moving forward in the thesis.

In chapter 4, the online phase inductance estimation using PWM excitation method is developed. This chapter introduces the concept of using current excitation provided by the PWM signals to estimate the phase inductance. Current excitation at all operating points, including zero rotor speed and zero voltage is developed. The equivalent inductance model for each switching state with respect to the phase inductance parameters is developed. This forms the key relationship between measureable equivalent inductance to the phase inductance parameters. The chapter then shows how to estimate the equivalent inductance from the measured rate of change of current. An Extended Kalman Observer (EKO) is used to estimate various equivalent inductance parameters. The equivalent inductance parameter are thus used to derive the L_d and L_q inductance. Finally, various results of the inductance estimated at different operating conditions are presented. The results thus obtained are verified with the FE analysis.

Chapter 5 address one of the main challenges in obtaining current derivative measurement without using any external hardware. First, this chapter identifies various switching states used for current derivative measurement. Next, the architecture needed to oversample the current without affecting the software throughput is introduced. The proposed architecture can be easily implemented in

processors widely used in automotive without any additional cost. Finally, two new methodologies to improve the accuracy of the current slope are presented. This section compares the proposed methodologies with an existing technique and identifies the improvement obtained with the proposed methods.

The position estimation using a PWM excitation signal with reduced ripple current is presented in Chapter 6. The various PWM phase shifting strategies to maintain current excitation is discussed. The ripple current generated due to the each phase shifting strategy are shown. The optimum PWM phase shift needed between phases at all operating range to obtain robust current slope is identified. The various switching states needed for current slope estimation are identified. The proposed strategy keeps the phase current ripple generated at minimum thereby enhancing the position estimation accuracy using PWM excitation. The thesis then moves on to present the Extended Kalman Observer implementation for both inductance estimation and position estimation. Position estimation strategy for zero and high speed are discussed and various position estimation results are shown for zero, low and mid speed operation.

This dissertation provides five distinct contributions towards sensorless position estimation and optimum control of PMSM drive, these are as follows:

1. The effect of the position sensor error on the performance of the PMSM drive system was studied, and subsequently a mathematical model was developed to understand the effect of position sensor error on the developed torque at various operating conditions.

2. An online stator inductance estimation technique using PWM excitation signals was developed. The estimation of inductance is accomplished without using any additional hardware or offline test. The proposed technique can be used to estimate inductance with a Modulation Index of zero to 0.7.

3. A software architecture which supports fast current sampling without affecting the software throughput was developed. The oversampling of current allows the introduction of two new strategies to measure the current derivative with improved accuracy and better signal to noise ratio.

4. A strategy to provide current excitation at all operating conditions, including zero speed and zero voltage, was developed. This thesis goes further to study the amount of current ripple generated due to various PWM phase shifting strategies. An optimum phase shift strategy is thus developed so that robust current derivative measurement can be obtained in order to maintain minimum phase current ripple.

5. Sensorless position estimation, without the use of additional hardware or signal injection for zero, low and mid speed was developed.

The few drawbacks of the proposed method are:

1. The present technology of the current sensor, amplifier and ADC does not capture the current slope information accurately. The inherent frequency response of the sensor and in the case of shunt based current sensing, the CMRR, are major reason for this.

2. The proposed PWM based position estimation technique does not allow estimation in the whole range of the motor operation.
3. Distinguishing between 0-180 degrees and 180-360 degree rotor position requires other known methods [23] .
4. As the observer needs to be implemented in the motor control loop it impacts the software throughput.

Scope for future work

1. Online inductance method proposed here works only upto MI=0.7. Since the inductance is only a function of motor current, a learning algorithm may be developed to estimate inductance above 0.7 based on motor current.

2. Implementation of the proposed position estimation using the current measurement sampled inside the processor.

3. Including the effect of fourth order content in the phase inductance for inductance and position estimation.

4. Effect of the various slope measurement error on position accuracy and inductance accuracy can be studied.

5. Algorithm to blend between the position estimation methods for zero, low, mid and high speed needs to be studied.

APPENDICES

`

APPENDIX A

Equation for torque generated as function of position error discussed in Chapter 2

$$T_d' = T_{R1}\cos(x) + T_{R2}\cos(2x) + T_{R3}\cos(3x) + T_{R4}\cos(4x) + T_{DC}$$

Where:

$$T_{R1} = (\left(0.75Pk1\left(L_d - L_q\right) - 0.281Pk1^3\left(L_d - L_q\right)\right) id_i^2 - 1.5K_e k1 id_i + \left(0.75Pk1\left(L_q - L_d\right) - 0.281Pk1^3\left(L_d - L_q\right)\right) iq_i^2$$

$$T_{R2} = (id_i iq_i \left(0.75Pk1^2\left(L_d - L_q\right) - 0.094Pk1^4\left(L_d - L_q\right)\right) - 0.375 * iq_i * K_e * k1^2$$

$$T_{R3} = (iq_i^2 \left(0.094Pk1^3\left(Ld - L_q\right)\right) - id_i^2 \left(0.094Pk1^3\left(L_d - L_q\right)\right)\right)$$

$$T_{R4} = \left(-id_i iq_i(0.023 * P * k1^4\left(L_d - L_q\right)\right)$$

$$T_{DC} = iq_i\ (1.5Ke - 0.375K_e * k1^2) - id_i iq_i\left(0.75P\left(L_d - L_q\right) - 0.75k1^2\left(L_d - L_q\right) + 0.07Pk1^4(L_d - L_q)\right)$$

$$x = n * \theta\ ;\ k1 = P * \hat{\theta}_{er}$$

`

Parameters of the IPM motor under study

Parameters	Value
K_e (V-s/rad)	0.02482
R(ohm)	0.008
L_q (Henry)	0.000065
L_d (Henry)	0.000049
Max Current (Rating(Amps)	100

`

APPENDIX B

Flow Chart of the DMA based Oversampling Technique Implementation on Infineon Tricore processor discussed in Chapter 4:

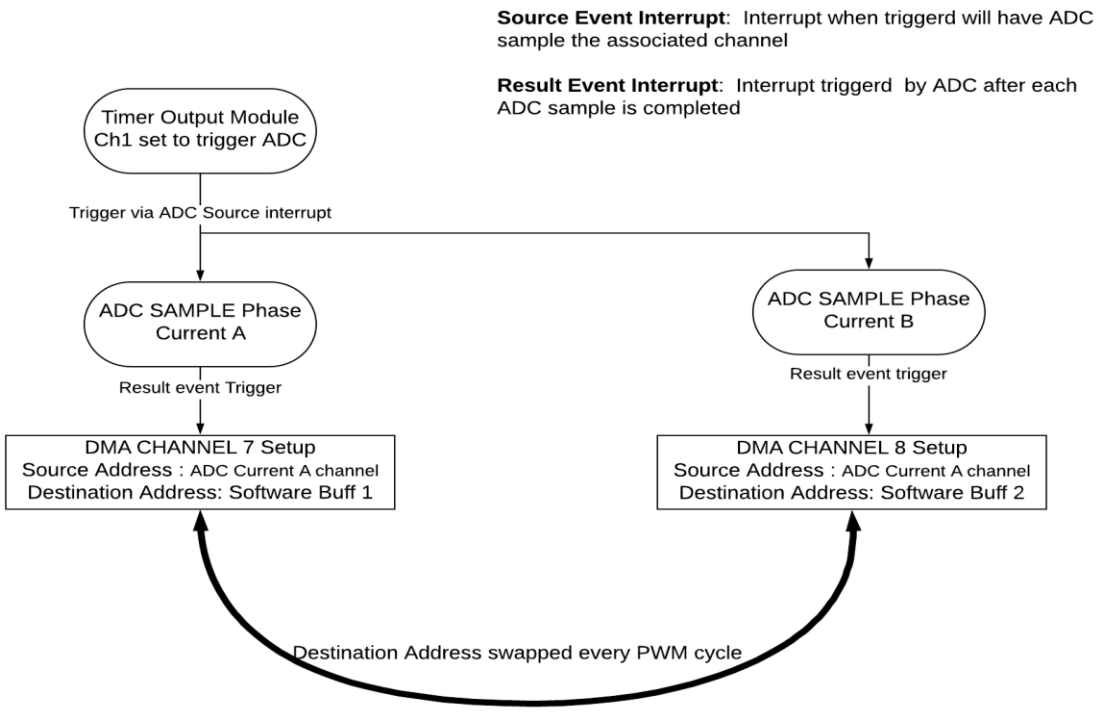

`

C code for the DMA based oversampling technique discussed in Chapter 4

Setting up the ADC to be triggered by Hardware timer and result even triggering the DMA.

DMA is setup to transfer data from the ADC result register to Software buffer “DMABf1_0” and “DMABf1_1”

```
void CurrSens_init(void)
{
    uint32 SrcAddress,SrcAddress1;


        /* ADC ENABLE TRIGGER*/
           GrpReqSrc = Adc_ConfigRoot[0].CfgPtr[0]->GrpCfgPtr->GrpRequestSrc;
           IntChMask = Adc_ConfigRoot[0].CfgPtr[0]->GrpCfgPtr->IntChMask;

        /* Destination Buffer Index */
           DestAddressNew[0]=(uint32)((uint32)&(DMABf_0[0]));
           DestAddressNew[1]=(uint32)((uint32)&(DMABf_1[0]));

        /* Destination Buffer 2 Index */
           DestAddressNew1[0]=(uint32)((uint32)&(DMABf1_0[0]));
           DestAddressNew1[1]=(uint32)((uint32)&(DMABf1_1[0]));


        /* Setting up Initial Buffer & DMA Setting */
           Result1Address0=(uint32) DestAddressNew[0];
           Result1Address1=(uint32) DestAddressNew1[0];

           SrcAddress = (uint32)&(VADC_G0RES4);
           SrcAddress1 = (uint32)&(VADC_G1RES4);

           SetupCurr_DMAChannel(Result1Address0, DMA_CHANNEL8, SrcAddress, MovespTransfer,DMASAMPLES);
           SetupCurr1_DMAChannel(Result1Address1, DMA_CHANNEL7, SrcAddress1, MovespTransfer,DMASAMPLES);

        /* This  has to go just  before the GPT start TIMERS*/
           Adc_EnableHardwareTrigger(AdcConf_AdcGroup_AdcGroup_0);


           /* Masking the Result Event to trigger the DMA compared to  */
            ADC_MODULE[Kernel].REVNP0.B.REV4NP = 0;
           ADC_MODULE[Kernel].SEVNP.B.SEV1NP  = 3;

            ADC_MODULE[Kernel1].REVNP0.B.REV4NP = 3;
            ADC_MODULE[Kernel1].SEVNP.B.SEV1NP  = 0;

        /* DMA TRANSFER DOESN'T CLEAR the READ FLAG THEREFORE NEED TO TURN OFF THE SETTING
         * FOR WAIT FOR READ FLAG IN ADC
         */

           ADC_MODULE[Kernel].RCR[4].B.WFR =0;
           ADC_MODULE[Kernel].RCR[5].B.WFR =0;
}
```

`

On every PWM cycle the DMA and the ADC hardware trigger is stopped and the destination address of the DMA channels are swapped. The function “priCurrSens” shown below is called once every PWM cycle. The error flags are cleared before swapping the Destination address. After swapping the DMA and the ADC channel triggers are enabled and the process continues for the next PWM cycle.

```
void priCurrSens(void)
{
    uint32 RemapAddress;

            /* Disabling the Timer */
            Gtm_DisableTomChannel(1,13);

            /*  Hardware Transaction Request : Disable Hardware Transfer Request for DMA Channel 8*/
            MODULE_DMA.TSR[DMA_CHANNEL8].U  |=((uint32)1U << 17);
            MODULE_DMA.TSR[DMA_CHANNEL8].B.RST = 1U;


            /*  Hardware Transaction Request : Disable Hardware Transfer Request for DMA Channel 7*/
            MODULE_DMA.TSR[DMA_CHANNEL7].U  |=((uint32)1U << 17);
            MODULE_DMA.TSR[DMA_CHANNEL7].B.RST = 1U;


            /* DMA Clear Error Flag */
            MODULE_DMA.TSR[DMA_CHANNEL8].B.CTL = 1U;
            MODULE_DMA.TSR[DMA_CHANNEL7].B.CTL = 1U;
            /* Set the Transfer Count Value */

            MODULE_DMA.CH[DMA_CHANNEL8].CHCFGR.B.TREL=DMASAMPLES;
            MODULE_DMA.CH[DMA_CHANNEL7].CHCFGR.B.TREL=DMASAMPLES;


            /* SWAP the  Destination Address for DMA */
            RemapAddress=((DestAddressNew[BufferIndex]& 0x0000FFFFU) | 0x70000000U);
            MODULE_DMA.CH[DMA_CHANNEL8].DADR.U  = (uint32)RemapAddress;


            RemapAddress=((DestAddressNew1[BufferIndex]& 0x0000FFFFU) | 0x70000000U);
            MODULE_DMA.CH[DMA_CHANNEL7].DADR.U  = (uint32)RemapAddress;


             /* Clear the Result register event flag */
             VADC_G0_REFCLR.U = IntChMask;
             VADC_G1_REFCLR.B.REV4=1;

             /* Clear the Channel register event flag */
             VADC_G0_CEFCLR.U = IntChMask;

            /* EnableHw transfer */
             MODULE_DMA.TSR[DMA_CHANNEL8].U  |= (uint32)((uint32)1U << DMA_TSR_ECH_BIT_POS);
             MODULE_DMA.TSR[DMA_CHANNEL7].U  |= (uint32)((uint32)1U << DMA_TSR_ECH_BIT_POS);

        /*Adc_EnableHardwareTrigger*/
             VADC_G0_SEFCLR.U = (1 << GrpReqSrc);

             /* Enabling the TIMER */
             Gtm_EnableTomChannel(1,13);
}
```

`

BIBLIOGRAPHY

[1] R. Grave, "Autonomous Driving – From Fail-Safe to Fail-Operational Systems," 2015.

[2] S. A. E. International, "Fail-Operational Safety Architecture for ADAS Systems Considering Domain ECUs," pp. 1–7, 2018.

[3] J. Holtz, "Speed estimation and sensorless control of AC drives," *Proc. IECON '93 - 19th Annu. Conf. IEEE Ind. Electron.*, vol. 2, pp. 649–654, 1993.

[4] D. Yousfi, M. Azizi, and a. Saad, "Robust position and speed estimation algorithm for permanent magnet synchronous drives," *Conf. Rec. 2000 IEEE Ind. Appl. Conf. Thirty-Fifth IAS Annu. Meet. World Conf. Ind. Appl. Electr. Energy)*, pp. 1541–1546, 2000.

[5] H. Kim, M. C. Harke, and R. D. Lorenz, "Sensorless control of interior permanent-magnet machine drives with zero-phase lag position estimation," *IEEE Trans. Ind. Appl.*, vol. 39, no. 6, pp. 1726–1733, 2003.

[6] R. Wu and G. R. Slemon, "A permanent magnet motor drive without a shaft sensor," *IEEE Trans. Ind. Appl.*, vol. 27, no. 5, pp. 1005–1011, 1991.

[7] S. O. Zhiqian Chen, Mutuwo Tomita, Shinji Ichikawa, Shinji Doki, "Sensorless Control of Interior Permanent Magnet Synchronous Motor by Estimation of an Extended Electromotive Force," no. September, pp. 1814–1819, 1992.

[8] S. Morimoto, K. Kawamoto, M. Sanada, and Y. Takeda, "Sensorless control strategy for salient-pole PMSM based on extended EMF in rotating reference frame," *IEEE Trans. Ind. Appl.*, vol. 38, no. 4, pp. 1054–1061, 2002.

[9] M. Tsuji, H. Mizusaki, and S. Hamasaki, "Stability Comparison of IPMSM Sensorless Vector Control Systems Using Extended EMF," no. 5, pp. 3093–3098, 2014.

[10] S. Chi, Z. Zhang, and L. Xu, "Sliding-mode sensorless control of direct-drive PM synchronous motors for washing machine applications," *IEEE Trans. Ind. Appl.*, vol. 45, no. 2, pp. 582–590, 2009.

[11] K. Kang and J. Kim, "Sensorless control of PMSM in high speed range with iterative sliding mode observer," *Appl. Power Electronics*, vol. 00, no. 1, pp. 1111–1116, 2004.

[12] Z. Peixo, F. M. Freitas Sa, P. Seixas, B. R. Menezes, P. C. Cortizo, and W. S. Lacerda, "Application of sliding mode observer for induced e.m.f., position and speed estimation of permanent magnet motors," *Proc. 1995 Int. Conf. Power Electron. Drive Syst. PEDS 95*, pp. 599–604, 1995.

[13] J. Jiang and J. Holtz, "High dynamic speed sensorless ac drive with on-line model parameter tuning for steady-state accuracy," *IEEE Trans. Ind. Electron.*, vol. 44, no. 2, pp. 240–246, 1997.

[14] D. Yousfi and Mustapha EI Adnani, "Indirect Position and Speed Sensing for PMSM Sensorless Control," *7th international confernce on power electonics,*pp. 817–822, 2007.

[15] L. A. S. Ribeiro, M. W. Degner, F. Briz, and R. D. Lorenz, "Comparison of carrier signal voltage and current injection for the estimation of flux angle or rotor position," *Ind. Appl. Conf. 1998. Thirty-Third IAS Annu. Meet. 1998 IEEE*, vol. 1, no. 1, pp. 452–459 vol.1, 1998.

[16] P. L. Jansen and R. D. Lorenz, "Transducerless Position and Velocity Estimation in Induction and Salient AC Machines," *IEEE Trans. Ind. Appl.*, vol. 31, no. 2, pp. 240–247, 1995.

[17] P. García, F. Briz, M. W. Degner, and D. Díaz-Reigosa, "Accuracy, bandwidth, and stability

limits of carrier-signal-injection-based sensorless control methods," *IEEE Trans. Ind. Appl.*, vol. 43, no. 4, pp. 990–1000, 2007.
[18] M. W. Degner and R. D. Lorenz, "Using multiple saliencies for the estimation of flux, position, and velocity in AC machines," *IEEE Trans. Ind. Appl.*, vol. 34, no. 5, pp. 1097–1104, 1998.
[19] A. Consoli, G. Scarcella, and A. Testa, "Industry application of zero-speed sensorless control techniques for PM synchronous motors," *IEEE Trans. Ind. Appl.*, vol. 37, no. 2, pp. 513–521, 2001.
[20] J. I. Ha and S. K. Sul, "Sensorless field-orientation control of an induction machine by high-frequency signal injection," *IEEE Trans. Ind. Appl.*, vol. 35, no. 1, pp. 45–51, 1999.
[21] T. M. Wolbank and J. Machl, "A modified PWM scheme in order to obtain spatial information of AC machines without mechanical sensor," *APEC. Seventeenth Annu. IEEE Appl. Power Electron. Conf. Expo. (Cat. No.02CH37335)*, vol. 00, no. c, pp. 310–315, 2002.
[22] M. Schroedl, "Sensorless Control of AC Machines at Low Speed and Standstill Based on the 'INFORM''' Method,'" *IAS '96. Conf. Rec. 1996 IEEE Ind. Appl. Conf. Thirty-First IAS Annu. Meet.*, vol. 1, pp. 270–277, 1996.
[23] E. Robeischl and M. Schroedl, "Optimized INFORM measurement sequence for sensorless PM synchronous motor drives with respect to minimum current distortion," *IEEE Trans. Ind. Appl.*, vol. 40, no. 2, pp. 591–598, 2004.
[24] F. Briz *et al.*, "Rotor Position Estimation," *IEEE Ind. Electron. Mag.*, vol. 5, no. 2, pp. 24–36, 2011.
[25] G. Qiang, G. M. Asher, and M. Sumner, "Position Estimation of AC Machines at all Frequencies using only Space Vector PWM based Excitation," *3rd IET Int. Conf. Power Electron. Mach. Drives(PEMD)*, pp. 61–70, 2006.
[26] Q. Gao, G. M. Asher, M. Sumner, and P. Makyš, "Sensorless control of induction machines, including zero frequency using only fundamental PWM excitation," *IECON Proc. (Industrial Electron. Conf.*, pp. 793–798, 2006.
[27] J. Lara and A. Chandra, "Position error compensation in quadrature analog magnetic encoders through an iterative optimization algorithm," *IECON Proc. (Industrial Electron. Conf.*, pp. 3043–3048, 2014.
[28] C. A. Borghi, D. Casadei, A. Cristofolini, M. Fabbri, and G. Serra, "Minimizing torque ripple in permanent magnet synchronous motors with polymer-bonded magnets," , *IEEE Trans. on Magnetics.*,vol. 38, no. 2, pp. 1371–1377, 2002.
[29] R. Ramakrishnan, A. Gebregergis, M. Islam, and T. Sebastian, "Effect of position sensor error on the performance of PMSM drives for low torque ripple applications," *Proc. 2013 IEEE Int. Electr. Mach. Drives Conf. IEMDC 2013*, pp. 1166–1173, 2013.
[30] M. S. Islam, S. Mir, and T. Sebastian, "Issues in reducing the cogging torque of mass-produced permanent-magnet brushless DC motor," *IEEE Trans. Ind. Appl.*, vol. 40, no. 3, pp. 813–820, 2004.
[31] G. Liu, A. Kurnia, R. De Larminat, and S. J. Rotter, "Position sensor error analysis for EPS motor drive," *IEMDC 2003 - IEEE Int. Electr. Mach. Drives Conf.*, vol. 1, pp. 249–254, 2003.
[32] S. Gopalakrishnan, L. Hao, C. Namuduri, K. Rahman, A. Omekanda, and C. Freitas, "Impact of position sensor accuracy on the performance of propulsion IPM drives," *Proc. - 2015 IEEE Int. Electr. Mach. Drives Conf. IEMDC 2015*, pp. 946–952, 2016.
[33] J. Liu, L. Dong, and G. Wang, "Research on brushless DC motor based on new type

electromagnetic position sensor," *ICEMS 2012 - Proc. 15th Int. Conf. Electr. Mach. Syst.*, 2012.

[34] M. Ehsani and A. B. Kulkarni, "A Novel Position Sensor Elimination Technique for the Interior Permanent-Magnet Synchronous Motor Drive," *IEEE Trans. Ind. Applications.*,vol. 28, no. 1, 1992.

[35] J. Lara, J. Xu, and A. Chandra, "Effects of Rotor Position Error in the Performance of Field Oriented Controlled PMSM Drives for Electric Vehicle Traction Applications," *IEEE Trans. Ind. Electron.*, vol. 0046, no. c, pp. 1–1, 2016.

[36] S. Y. Jung and K. Nam, "PMSM control based on edge-field hall sensor signals through ANF-PLL processing," *IEEE Trans. Ind. Electron.*, vol. 58, no. 11, pp. 5121–5129, 2011.

[37] Y. H. C. H.S.Mok, S.H.Kim, "Reduction of PMSM torque ripple caused by resolver error," *Trans. Korean Inst. Electr. Eng.*, vol. 57, no. 6, pp. 982–984, 2008.

[38] J. Kim, S. Choi, K. Cho, and K. Nam, "Position Estimation Using Linear Hall Sensors for Permanent Magnet Linear Motor Systems," *IEEE Trans. Ind. Electron.*, vol. 63, no. 12, pp. 7644–7652, 2016.

[39] G. Wang, T. Li, G. Zhang, X. Gui, D. Xu, and S. Member, "Position Estimation Error Reduction Using Recursive-Least-Square Adaptive Filter for Model-Based Sensorless Interior Permanent-Magnet Synchronous Motor Drives," *IEEE Trans. Ind. Electron.*, vol. 61, no. 9, pp. 5115–5125, 2014.

[40] A. Iosub, J. Kirscher, A. Buzo, G. Pelz, and L. Goras, "On the influence of angle sensor nonidealities on the torque ripple in PMSM systems - An analytical approach," *2016 13th Int. Conf. Synth. Model. Anal. Simul. Methods Appl. to Circuit Des. SMACD 2016*, pp. 1–4, 2016.

[41] S. H. Hwang, H. J. Kim, J. M. Kim, L. Liu, and H. Li, "Compensation of amplitude imbalance and imperfect quadrature in resolver signals for PMSM drives," *IEEE Trans. Ind. Appl.*, vol. 47, no. 1, pp. 134–143, 2011.

[42] A. Khattab, M. Benammar, and F. Bensaali, "A Novel Method for Online Correction of Amplitude and Phase Imbalances in Sinusoidal Encoders Signals," pp. 1–6.

[43] S. M. Methods, C. W. Secrest, J. S. Pointer, M. R. Buehner, and R. D. Lorenz, "Improving Position Sensor Accuracy Through Spatial Harmonic Decoupling, and Sensor Scaling, Offset, and Orthogonality Correction Using Self-Commissioning MRAS Methods," vol. 51, no. 6, pp. 4492–4504, 2015.

[44] A. Shea, S. Member, and T. M. Jahns, "Control Challenges and Mitigation Techniques for Sensor Errors in Modular Motor Drives with Weakly-Coupled Distributed Control Architectures," pp. 890–896, 2015.

[45] Charles V Jones, *Unified Theory of Electrical Machines: Charles V. Jones:* Butterworths & Co. Publishers Ltd, 1967.

[46] R. Dutta and M. F. Rahman, "A Comparative Analysis of Two Test Methods of Measuring d - and q -Axes Inductances of Interior Permanent-Magnet Machine," *Magn. IEEE Trans.*, vol. 42, no. 11, pp. 3712–3718, 2006.

[47] Y. S. Jeong and J. Y. Lee, "Adaptive flux observer with on-line inductance estimation of an interior PM synchronous machine considering magnetic saturation," *36th Power Electron. Spec. Conf.*, vol. 9, no. 2, pp. 188–197, 2005.

[48] S. Ichikawa, M. Tomita, S. Doki, and S. Okuma, "Sensorless control of permanent-magnet synchronous motors using online parameter identification based on system identification theory," *IEEE Trans. Ind. Electron.*, vol. 53, no. 2, pp. 363–372, 2006.

`

[49] P. Caldori, A. Guagnano, V. G. Monopoli, and F. Cupertino, “Inductance measurement methods for position estimation in permanent magnet synchronous motors,” *2016 XXII Int. Conf. Electr. Mach.*, pp. 1078–1084, 2016.

[50] Kyeong-Hwa Kim, Se-Kyo Chung, Gun-Woo Moon, In-Cheol Baik, and Myung-Joong Youn, “Parameter estimation and control for permanent magnet synchronous motor drive using model reference adaptive technique,” *Proc. IECON ’95 - 21st Annu. Conf. IEEE Ind. Electron.*, vol. 1, pp. 387–392, 1995.

[51] S. A. Odhano, P. Giangrande, R. I. Bojoi, and C. Gerada, “Self-commissioning of interior permanent- magnet synchronous motor drives with high-frequency current injection,” *IEEE Trans. Ind. Appl.*, vol. 50, no. 5, pp. 3295–3303, 2014.

[52] S. Moreau, R. Kahoul, and J. P. Louis, “Parameters Estimation of Permanent Magnet Synchronous Machine without adding extra-signals as input excitation,” *2004 IEEE Int. Symp. Ind. Electron.*, vol. 1, pp. 371–376 vol. 1, 2004.

[53] K. M. Rahman and S. Hiti, “Identification of machine parameters of a synchronous motor,” *IEEE Trans. Ind. Appl.*, vol. 41, no. 2, pp. 557–565, 2005.

[54] G. Pellegrino, B. Boazzo, and T. M. Jahns, “Magnetic Model Self-Identification for PM Synchronous Machine Drives,” *IEEE Trans. Ind. Appl.*, vol. 51, no. 3, pp. 2246–2254, 2015.

[55] S. Morimoto, M. Sanada, and Y. Takeda, “Mechanical sensorless drives of IPMSM with online parameter identification,” *IEEE Trans. Ind. Appl.*, vol. 42, no. 5, pp. 1241–1248, 2006.

[56] Q. Gao, G. M. Asher, M. Sumner, and P. Makys, “Position Estimation of AC Machines Over a Wide Frequency Range Based on Space Vector PWM Excitation,” *IEEE Trans. Ind. Appl.*, vol. 43, no. 4, pp. 1001–1011, 2007.

[57] P. Nussbaumer and T. M. Wolbank, “Saliency tracking based sensorless control of AC machines exploiting inverter switching transients,” *2010 1st Symp. Sensorless Control Electr. Drives, SLED 2010*, pp. 114–119, 2010.

[58] P. Nussbaumer and T. M. Wolbank, “Using oversampling techniques to extract AC machine saliency information,” *IECON Proc. (Industrial Electron. Conf.*, pp. 1035–1040, 2010.

[59] D. Q. Guan, M. X. Bui, D. Xiao, and M. F. Rahman, “Evaluation of an FPGA current derivative measurement system for the fundamental PWM excitation sensorless method for IPMSM,” *2016 IEEE 2nd Annu. South. Power Electron. Conf. SPEC 2016*.

[60] D. Hind, M. Sumner, and C. Gerada, “Estimating current derivatives for sensorless motor drive applications,” *2015 17th Eur. Conf. Power Electron. Appl. EPE-ECCE Eur. 2015*, no. 1, 2015.

[61] Y. Duan and M. Sumner, “A novel current derivative measurement using recursive least square algorithms for sensorless control of permanent magnet synchronous ma- chine,” *IEEE Conf. IPEMC*, pp. 1193–1200, 2012.

[62] P. Kim, L. Huh, and A-JIN Publishing, *Kalman Filter for Beginners : with MATLAB Examples*. .

[63] R. Raute, C. Caruana, C. S. Staines, J. Cilia, M. Sumner, and G. Asher, “Operation of a Sensorless PMSM Drive Without Additional Test Signal Injection,” *Power Electron. Mach. Drives, 2008. PEMD 2008. 4th IET Conf.*, pp. 616–620, 2008.

[64] Y. Hua, M. Sumner, G. Asher, and Q. Gao, “Sensorless Control for a PM Machine with Reduced Current Distortion using Space Vector PWM Excitation Keywords 2 . Position Estimation only Using Fundamental SVPWM,” pp. 1–10, 2009.